

Microscopic characterization of functionalized paper as a platform for 3D cell cultures

**Mikroskopische Charakterisierung funktionalisierter Papiere als Plattform für 3D
Zellkultur**

Zur Erlangung eines Doktors der Naturwissenschaften (Dr. rer. nat.)

dem Fachbereich Biologie vorgelegte Dissertation von **Steven Bump** aus Rüsselsheim

Juni 2015 – Darmstadt – D 17



TECHNISCHE
UNIVERSITÄT
DARMSTADT

Microscopic characterization of functionalized paper as a platform for 3D cell cultures

Dem Fachbereich Biologie
Der Technischen Universität Darmstadt

Zur Erlangung des akademischen Grades eines

Doktor der Naturwissenschaften (Dr. rer. nat.)

genehmigte

Dissertation

eingereicht von

Dipl. Biol. Steven Bump

aus Rüsselsheim

Referent: PD Dr. Tobias Meckel

Korreferent: Prof. Markus Biesalski, PhD

Tag der Einreichung: 04.06.2015

Tag der mündlichen Prüfung: 17.07.2015

Darmstadt 2015

Ehrenwörtliche Erklärung

Ich erkläre hiermit ehrenwörtlich, dass ich die vorliegende Arbeit entsprechend den Regeln guter wissenschaftlicher Praxis selbstständig und ohne unzulässige Hilfe Dritter angefertigt habe.

Sämtliche aus fremden Quellen direkt oder indirekt übernommenen Gedanken sowie sämtliche von Anderen direkt oder indirekt übernommenen Daten, Techniken und Materialien sind als solche kenntlich gemacht. Die Arbeit wurde bisher bei keiner anderen Hochschule zu Prüfungszwecken eingereicht.

Darmstadt, den 04.08.2015

Steven Bump

Statement of own work

I have undertaken all experiments, data analysis and writing of the present thesis with exception of the following:

- Images shown in Fig. 13 were provided and corresponding experiments were conducted by Laura Babel (Technische Universität Darmstadt, Darmstadt, Germany).
- Figure 5 was provided by Alexander Böhm (Technische Universität Darmstadt, Germany).
- Figure 17 was generated and provided by Dr. Tobias Meckel (Technische Universität Darmstadt, Germany).
- Chapters 1.6. to 1.6.6., 2.3.4. to 2.3.5., 2.4.. 3.3. and 4.3. are slightly modified from a previously published (without stated exceptions) peer-reviewed publication:
 - o Bump, Steven; Böhm, Alexander; Babel, Laura; Wendenburg, Sonja; Carstens, Franz; Schabel, Samuel; Biesalski, Markus and Meckel, Tobias. (2014) „Spatial, spectral, radiometric, and temporal analysis of polymer-modified paper substrates using fluorescence microscopy” *Cellulose*. Volume 22, Issue 1, pp 73-88, doi: 10.1007/s10570-014-0499-5, 2014.

Summary

To achieve an understanding and complete description of the functional properties of three dimensional (3D) cell culture systems, a large set of parameters is required, which clearly contrasts this cell cultivation approach from traditional two dimensional (2D), planar cultivation techniques. As an alternative to describe the characteristics of a 3D cell culture system by its physicochemical properties (e.g. stiffness, porosity, level of crosslinking), the behavior of the cultivated cells can be used as a read-out parameter to characterize the 3D cultivation system. In this work, the cellular parameters *membrane dynamics*, *actin fiber morphology* and *migration* were used to investigate the differences between classic, planar and a collagen based three dimensional cell culture system

Membrane dynamics – assessed by FRAP measurements of CAAX-mCherry – as well as actin formation – visualized by *in vitro* staining with LifeAct-tagRFP – showed distinct differences when investigated in planar or three dimensional systems. FRAP experiments with CAAX-mCherry showed, that even though the overall membrane composition does not appear to be different, mobility of the membrane is significantly higher in three dimensional cell culture systems than in two dimensional. A view at the actin cytoskeleton revealed the already established difference: stress fibers and cortical actin are more pronounced in planar cell culture systems compared to cells cultivated in three dimensional systems. Interestingly, cells originally seeded in collagen hydrogels which migrated towards the glass surface show features in actin cytoskeleton formation resembling both culture conditions: both, actin stress fibers within the cell body as well as cortical actin are visible in those parts of the cells directly contacting the glass surface.

The observed migration towards the glass surface gave rise to the investigation of this behavior. Migration in response to mechanical signals is termed durotaxis. Cells cultivated in collagen hydrogels or collagen hydrogels supported by cellulose sheets over a period of time were microscopically investigated to determine the distribution of cells. Cell distribution in

unsupported collagen hydrogels was clearly in favor of hydrogel regions in close proximity to the glass surface. By applying supporting material in form of cellulose sheets, the cell culture was freely floating in the culture medium, resulting in an even distribution throughout the entire thickness of the cell culture system.

As 3D cell culture systems make it more challenging to perform high quality imaging due to the inherent scattering and loss of intensity with increasing optical penetration, a post imaging processing tool set was evaluated and benchmarked in order to counteract these image corrupting effects and improve the image quality. This in turn also improves the compatibility of cellulose sheets with the commonly used tool set in life sciences: fluorescence microscopy. Special emphasis was put on the identification of a serviceable and performance-linked deconvolution setup. A GPU based CUDA Deconvolution plugin showed the best time performance but ultimately failed to produce the same quality level of image restoration as the three tested CPU based deconvolution applications. Among these three, the commercial HuygensPro software showed the best results in terms of increasing the contrast. The Iterative Deconvolution 3D plugin comes close to producing comparable results to the HuygensPro software, however, the time consumption for this application is up to 10 times larger. Finally, the plugin Deconvolution Lab showed reasonably satisfying results in terms of image restoration quality, while performing deconvolution slightly faster than HuygensPro.

Finally, cellulose sheets are used for the cultivation of cells in 3D as an example of for paper as a versatile platform for the development of functional devices. Therefore a method is required that delivers spatially resolved, quantitative, sensitive, and, most importantly, also dynamic measurements. Optical microscopy has long been recognized as a method to characterize the heterogeneous and complex structure of paper. With fluorescence detection, the functionality has even been extended to provide chemical selectivity, e.g. to determine the distribution of secondary modifications like coatings and fillers throughout a sheet of paper. Here it is shown that quantitative widefield and confocal fluorescence microscopy are versatile methods to meet this set of demands. Confocal microscopy was used to achieve a detailed view of the

interface between a hydrophobic and rhodamine labeled polymer and a FITC labeled dextran solution. Furthermore, confocal microscopy revealed that the spatial propagation of the FITC labeled dextran solution occurs along the surface of the cellulose fibers, instead of the inter-fibers space. Widefield fluorescent microscopy was subsequently used for dynamic investigations of this spatial propagation.

Zusammenfassung

Für ein besseres Verständnis der, im Vergleich zur zwei dimensional Zellkultur, komplexeren drei dimensional Zellkultursysteme können eine Reihe von bereits etablierten Parametern herangezogen werden. Parameter wie Steifigkeit, Porosität, Vernetzungsgrad und andere beschreiben die physicochemischen Eigenschaften eines 3D Systems. In dieser Arbeit werden als Alternative die zellulären Eigenschaften *Membrandynamik*, *Morphologie der Aktinfasern* und die *Migration* zur Charakterisierung eines Kollagen basierten drei dimensional Zellkultursystems herangezogen und Unterschiede zu klassischen, planaren Zellkultur aufgezeigt.

Sowohl die Membrandynamik – untersucht mittels FRAP Messungen von CAAX-mCherry – als auch die Morphologie der Aktinfasern – beobachtet durch in vitro Anfärbung mit LifeAct-tagRFP – zeigten klar erkennbare Unterschiede in Abhängigkeit des Kultivierungssystems. FRAP Messungen mit CAAX-mCherry zeigten, dass die Mobilität der Membran in drei dimensional Kultursystemen größer ist, als in zwei dimensional, planaren Systemen. Ein Blick auf das Aktin Zytoskelett bestätigt den bereit etablierten Unterschied: Stressfasern und kortikales Aktin treten im Wesentlichen nur in Zellen auf, welche in planaren Zellkultursystemen wachsen. Allerdings: ursprünglich in einem Kollagen Hydrogel ausgesäte Zellen, die in Richtung Glassoberfläche gewandert sind, zeigten Zytoskelett Eigenschaften, die in beiden Kulturbedingungen auftreten: sowohl Aktin Stressfasern als auch kortikales Aktin sind sichtbar in Zellbereichen mit direktem Kontakt zur Glassoberfläche.

Die Wanderung von Zellen innerhalb von drei dimensional Systemen in Richtung Glassoberfläche, ist eine Antwort auf ein mechanisches Signal und wird als Durotaxis bezeichnet. Zur Untersuchung dieser Migration wurden Zellen in Kollagen Hydrogelen oder in Kollagen Hydrogelen gestützt durch Papier kultiviert. Mikroskopisch Untersuchung der Zellverteilung im Laufe der Zeit zeigte eine Anhäufung der Zellen in Bereichen des Kollagen Hydrogels, welche in räumlicher Nähe zur Glassoberfläche sind. Durch die Einführung des Papiers schwimmen die Kollagen Hydrogele im Medium, wodurch kein Kontakt

mehr zur Glassoberfläche vorhanden ist. In solchen Systemen zeigte sich eine gleichmäßigere Verteilung der Zellen über das gesamte Zellkultursystem.

Dreidimensionale Zellkultursysteme stellen auf Grund ihrer hohen Lichtstreuung und des Intensitätsverlust bei steigender optischer Eindringtiefe, eine erhöhte Herausforderung für die Durchführung von hochqualitativer Mikroskopie dar. Um diesem Problem entgegenzuwirken, wurde die Anwendbarkeit einer Dekonvolutionssoftware getestet. Dabei wurde neben der eigentlichen Anwendbarkeit auch besonders auf die Performance geachtet. Das GPU basierte CUDA Deconvolution Plugin war zwar am schnellsten, aber zeigte letztendlich die geringste Verbesserung der Bildqualität im Vergleich zu den drei ebenfalls getesteten CPU basierten Dekonvolutions-Anwendungen. Unter diesen drei Anwendungen, zeigte die kommerziell erhältliche HyugensPro Software die besten Ergebnisse. Das frei erhältliche Plugin Iterative Deconvolution 3D zeigte zwar Verbesserungen auf einem Niveau, welches vergleichbar mit HuygensPro ist, allerdings prozessierte dieses Plugin die Bilder bis zu zehnmal länger. Das Plugin Deconvolution Lab liegt zwar etwas unterhalb der Verbesserungsqualität von HyugensPro und Iterative Deconvolution 3D, ist dafür aber schneller als die beiden genannten Systeme.

Die Einführung von Papier in dreidimensionale Zellkultursysteme ist ein weiteres Beispiel dafür, dass das Potential von Papier für die Entwicklung von funktionalen Geräten erkannt wurde. Methoden, die in der Lage sind quantitative Messungen mit höher Sensitivität und sowohl räumlicher als auch – und vor allem – zeitlicher Auflösung zu liefern sind daher nötig. Optische Mikroskopie wird bereits länger dazu eingesetzt, die Heterogenität und Komplexität von Papier zu untersuchen. Fluoreszenz Mikroskopie erweitert die Funktionalität der Mikroskopie und ermöglicht chemische Selektivität, die dabei hilfreich ist beispielsweise die Verteilung von sekundären Modifikationen wie Beschichtungen und Füllstoffen zu untersuchen. Quantitative Weitfeld-Mikroskopie und Konfokale Fluoreszenz Mikroskopie sind vielseitig anwendbare Methoden und werden hier genutzt um ein Papiersystem zu untersuchen, welches mittels eines Rhodamin markierten hydrophoben Polymers modifiziert wurde. Darüberhinaus wurde die Ausbreitung einer mit FITC markierten Dextran-Lösung untersucht. Es zeigte

sich, dass die Verbreitung dieser Flüssigkeit entlang der Oberfläche der Fasern stattfindet. Das Flussverhalten wurde anschließend mittels Weitfeld-Mikroskopie quantifiziert.

Contents

Microscopic characterization of functionalized paper as a platform for 3D cell cultures	
Ehrenwörtliche Erklärung	I
Statement of own work	II
Summary	III
Zusammenfassung	VI
Contents	IX
Figures	XI
Tables	XII
Abbreviations	XIII
1. Introduction	- 1 -
1.1. 3D cell culture	- 1 -
1.2. Durotaxis – mechanotaxis in response to stiffness	- 3 -
1.3. Actin cytoskeleton	- 5 -
1.4. Fluorescence recovery after photobleaching (FRAP)	- 5 -
1.5. Understanding the basic principle of Deconvolution – Outline of image formation	- 7 -
1.5.1. Point Spread Function and the effect on image formation in light microscopy	- 7 -
1.5.2. Principle of deconvolution	- 10 -
1.6. Paper as a platform for functional devices	- 11 -
1.6.1. Further development of functional paper	- 12 -
1.6.2. Structural analysis of paper	- 12 -
1.6.3. Requirement for compositional and dynamic analyses of paper	- 14 -
1.6.4. Living cells and tissue: A specimen with similar demanding analytical requirements	- 16 -
1.6.5. Quantitative fluorescence microscopy for multi-parameter analysis of paper	- 17 -
2. Materials and Methods	- 18 -
2.1. Cell culture preparation	- 18 -
2.1.1. Cell culture	- 18 -
2.1.2. (3-Aminopropyl)trimethoxysilane (APTMS) surface modification of coverslips	- 18 -
2.1.3. Collagen hydrogel preparation	- 19 -
2.1.4. Plasmid isolation	- 20 -
2.1.5. Actin cytoskeleton labeling with LifeAct-RFP	- 20 -
2.1.6. Plasma membrane labeling with CAAX-mCherry	- 21 -
2.1.7. Plasma membrane staining with Vybrant® Multicolor Cell-Labeling Kit	- 21 -
2.2. Imaging setup and image analysis	- 22 -
2.2.1. Imaging of actin cytoskeleton and cell distribution	- 22 -
2.2.2. FRAP experiments parameters	- 22 -
2.2.3. Image segmentation for investigation of cell distribution	- 22 -

2.2.4. Widefield epifluorescence microscopy and image analysis of paper samples	- 25 -
2.2.5. Confocal Imaging of triple stained paper	- 28 -
2.3. Image post processing via deconvolution	- 29 -
2.3.1. Deconvolution Applications	- 29 -
2.3.2. Test Images	- 30 -
2.3.3. Generation of point spread functions (PSF)	- 31 -
2.4. Paper modification	- 32 -
2.4.1. Monomer and polymer synthesis	- 32 -
2.4.2. Preparation of lab-engineered and polymer-modified paper	- 32 -
2.5. Flow experiments in paper	- 35 -
2.5.1. Widefield epifluorescence microscopy and analysis of flow experiments using FITC-Dextran and ethylene glycol tetraacetic acid (EGTA) ...	- 35 -
2.5.2. Widefield epifluorescence microscopy and analysis of flow experiments using FITC-Isomer I	- 35 -
3. Results and Discussion	- 36 -
3.1. Comparison of deconvolution packages	- 36 -
3.1.1. Intensity profiles as benchmark for image restoration quality	- 37 -
3.1.2. Comparison of temporal performance	- 41 -
3.1.3. More detailed view at the GPU based CUDA deconvolution factory ..	- 42 -
3.1.4. Isosurface rendering to show and compare the beneficial effect of deconvolution	- 44 -
3.2. Difference between 2D and 3D cell culture: Using cellular distribution, actin morphology and membrane dynamics as read-out parameters	- 47 -
3.2.1. Durotaxis – Migration towards the glass surface	- 48 -
3.2.2. A view at the actin cytoskeleton	- 55 -
3.2.3. Fluorescence Recovery after Photobleaching	- 58 -
3.3. Microscopic analysis of modified paper	- 59 -
3.3.1. Cellulose staining with Calcofluor White	- 60 -
3.3.1. Polymer concentration and brightness are correlated	- 61 -
3.3.2. Analysis of spot border sharpness versus polymer concentration yields valuable information on polymer distribution	- 63 -
3.3.3. Spatial relation of the three component system: paper – polymer - fluid .-	65 -
3.3.4. Initial fluid transport takes place at the fiber surface only	- 71 -
3.3.5. Fluid transport in paper	- 74 -
4. Conclusions	- 78 -
4.1. Comparison of deconvolution packages	- 78 -
4.2. Difference between 2D and 3D cell culture: Using cellular distribution, actin morphology and membrane dynamics as read-out parameters	- 79 -
4.3. Microscopic analysis of modified paper	- 81 -
5. References	- 83 -
6. Danksagung	- 92 -
7. Curriculum Vitae	- 94 -

Figures

Figure 1: Effect of the PSF on the image formation during light microscopy	- 9 -
Figure 2: Optimal, theoretical vs empirical PSF	- 10 -
Figure 3: Workflow for the analyses of cell distribution inside a collagen hydrogel	- 24 -
Figure 4: Radiometric and spatial quantification of polymer spot border roughness and intensity	- 27 -
Figure 5: Photolithographic generation of hydrophobic, fluorescent micro patterns on paper	- 34 -
Figure 6: Single Slice images of a P(MMA-co-MABP-co-RhBMA) coated paper	- 39 -
Figure 7: Maximal intensity Z-projection images of P(MMA-co-MABP-co-RhBMA) coated paper	- 41 -
Figure 8: Restored images with CUDA Deconvolution Factory running for 2500 iterations or an application determined number of iterations	- 46 -
Figure 9: Isosurface Render Images generated with the same intensity threshold value	- 47 -
Figure 10: Distribution of OVMZ-6 cells inside a collagen hydrogel on a glass surface	- 49 -
Figure 11: Distribution of OVMZ-6 cells measured by pixel amount distribution	- 51 -
Figure 12: Orthogonal Views of OVMZ-6 cells in collagen hydrogel after 24 h	- 52 -
Figure 13: Spheroid like structures formed in paper by HeLa cells	- 54 -
Figure 14: Comparison of the actin cytoskeleton between OVMZ-6 cells under different cell culture conditions	- 56 -
Figure 15: Comparison of the cell positioning and the effect on the actin cytoskeleton in different surroundings	- 57 -
Figure 16: FRAP curves of CAAX-mCherry	- 58 -
Figure 17: Maximal intensity Z-projection of a cellulose network stained with calcofluor white	- 61 -
Figure 18: Calculated Point Spread Function for the Nikon CFI Plan Fluor 4x objective	- 63 -
Figure 19: Spectral separation of cellulose, polymer and the fluid-phase	- 67 -
Figure 20: Exclusion of the aqueous phase from hydrophobic polymer areas as revealed by confocal microscopy	- 68 -
Figure 21: High magnification view of polymer distribution at various concentrations	- 69 -
Figure 22: 3D isosurface generation for quantitative analysis of volume and surface areas	- 70 -
Figure 23: Temporal analysis of FITC-Dextran solution transport using widefield and resonant scanning confocal microscopy	- 73 -
Figure 24: Flow behavior for the three tested fluids aqueous FITC-Dextran, aqueous FITC-Dextran with EGTA and FITC-Isomer I in acetone	- 76 -

Tables

Table 1: Summary of Fluorophores used in this study and setup of image acquisition parameters during sequential imaging.	- 29 -
Table 2: Properties of the test image stacks. All images were acquired as 16-Bit images.	- 30 -
Table 3: Time performance of CUDA Deconvolution factory	- 43 -
Table 4: Time it took the different applications to deconvolve four different test image stacks.....	- 44 -
Table 5: Inflow and outflow rate for different fluids in paper	- 75 -

Abbreviations

(3-Aminopropyl)trimethoxysilane	APTMS
4-(2-hydroxyethyl)-1-piperazineethanesulfonic acid	HEPES
Adenosine tri/diphosphate	ATP/ADP
Central processing unit	CPU
Confocal laser scanning microscopy	CLSM
Compute Unified Device Architecture	CUDA
Dulbecco's modified eagle media	DMEM
Ethylenediaminetetraacetic acid	EDTA
Fluorescein isothiocyanate	FITC
Fluorescence recovery after photobleaching	FRAP
Foetal calf serum	FCS
Green fluorescent protein	GFP
giga byte	GB
giga hertz	GHz
Graphical processing unit	GPU
Numerical aperture	NA
Penicillin/Streptomycin	pen/strep
Phosphate buffered saline	PBS
Point spread function	(PSF)
Poly ethylene glycol	PEG
Red fluorescent protein	RFP
Three dimensional	3D
Two dimensional	2D

1. Introduction

1.1. 3D cell culture

Conventional cell culture systems are based on cultivating cells in a sub confluent state on two dimensional surfaces like glass or plastics. However, this paradigm is changing, since it has been demonstrated multiple times, that cellular behavior and responses equal the native occurrence more closely when cultivated in three dimensional environments (Cukierman et al. 2002). It has been shown, that certain cell types show fundamentally different behavior when cultivated on either planar surfaces or in three dimensional systems, for example breast epithelial cells showed tumor like behavior when under two dimensional cultivation conditions, whereas growth behavior more closely resembled that of cells *in vivo* (Petersen et al. 1992). But not only cancer research profits from the introduction and development of three dimensional cell culture conditions, fundamental research also benefits from cell culture conditions that approximate the *in vivo* conditions. Embryonic stem cells are able to more efficiently differentiate if cultivated in three dimensional systems (Barcelloss-Hoff et al. 1989; Tanaka et al. 2004). Probably most important in terms of pharmaceutical and medical applications is the observation of increased chemo- and radioresistance many cells exhibit when cultivated in three dimensional systems as opposed to two dimensional systems (Eke and Cordes 2011). Last but not least, three dimensional cell culture systems have the potential of greatly reducing the amount of animal experimentation, due to the fact, that the overall control over certain aspects of the system in use are easier to understand and control than they are in animal experiments (Pampaloni and Stelzer 2010; Hutmacher 2010).

In principal two different approaches for the formation of supported three dimensional cell culture systems can be distinguished: natural components can be used (either as undefined extracts, i.e., basal membrane extract or in form of

defined single components matrices, i.e., collagen, fibronectin, and alginate) or the three dimensional system can be synthesized by artificial polymers such as, for example, poly ethylene glycol (PEG) (Weber et al. 2009). Whereas the first approach guarantees biocompatibility, the later one offers tight control over the physical and chemical properties of the polymer in use, for example by introducing matrix metalloproteinase sensitive peptide sequences into a PEG hydrogel. By doing so, the otherwise inert hydrogel is rendered enzymatically degradable (Turturro et al. 2013). The introduction of peptides into an artificial hydrogel is also an example for the combination of natural and artificial components, resulting in systems that combine the advantages of the natural and artificial components at the same time. These qualities are useful, for example, in crafting of lab-on-chip devices (Barkefors et al. 2009; Huh et al. 2011; Huh et al. 2013).

In addition to the supported three dimensional cell culture systems, multi-cellular spheroids represent another example of three dimensional cell culture system, providing cell-to-cell contacts in all spatial directions and generating oxygen and nutrient gradients. Formation of such multi-cellular spheroids is easily achieved *via* hanging drop cell culture protocols (Foty 2011) or the liquid overlay method (Material et al. 2012). In contrast to methods applying either natural or synthetic polymers as scaffolds in which cells are incorporated, these methods utilize an extra cellular matrix which is synthesized by the cells. This, however, limits the methods to cell types able to synthesize an extra cellular matrix and, more importantly, move the exact parameters – in terms of composition and modifiability - of this matrix beyond the control of the experimenter.

1.2. Durotaxis – mechanotaxis in response to stiffness

Movement and migration of cells in response to biochemical signals is a commonly known and heavily researched phenomenon. Chemotaxis plays a vital role in many biological processes, for example keratinocytes are required to migrate to a wound in order to close it (Usui et al. 2008), immune response is based on reaction cascades triggered by chemokines (Thelen 2001) and migration is tightly controlled during embryogenesis (Wood et al. 2006). However, hormone or nutrient gradients are not the only known reason for migratory cell activities. Cells are also able to sense and respond to the mechanical properties of their surroundings. The mechanical properties of the cell's vicinity directly affect the stiffness of the cytoskeleton and the formation of focal adhesions as was shown by mechanical stress experiments using magnetic beads and forces (Wang et al. 1993). Mechanical stress also influences integrin-cytoskeleton connections, namely by increasing the strength of these linkages in correlation to the magnitude of the mechanical stress (Choquet et al. 1997). More detailed insight into the underlying cause of these mechanosensitivities was gained by cultivating cells on substrates with defined stiffness gradients under constant chemical conditions (Pelham and Wang 1997), revealing that cells predominantly migrate towards regions with higher stiffness.

The preference of surroundings with high stiffness influences all cell culture systems containing materials presenting stiffness values normally not found *in vivo*. This is obvious in two dimensional cell culture systems, where cells exhibit different shape and actin stress fiber formation than in three dimensional culture systems; this is, in fact, true regardless of whether the cells are in direct contact to the the surface of the culture system - mostly comprising of plastic or glass - or seeded onto a thin layer of extra cellular matrix (Hakkinen et al. 2011). Considering, that the elastic modulus, which is a common way to measure and quantify the stiffness of materials, for glass lies within the range of gigapascal (see www.engineeringtoolbox.com) whereas the elastic modulus for a variety of different materials commonly used to generate hydrogels for three dimensional

cell culture was shown to lie within the range of kilopascal (Markert et al. 2013), this significant difference in stiffness can lead to unwanted migration. This undesirable behavior is a problem especially in long term culture experiments such as, i.e., the formation of tissues or tissue like cell agglomerations.

In three dimensional cell culture systems with stiffness gradients, migration is influenced in two ways: (i) migratory speed is increased on stiffer regions and (ii) migratory directionality towards higher stiffness is observed. As a result cells accumulate in regions with high stiffness whereas other regions are depleted of cells (Vincent et al. 2014). Even without intentionally introducing a stiffness gradient into a three dimensional cell culture system, the described preference of stiffer regions is an always existing factor, namely at the interface between the extra cellular matrix and the glass or plastic surface of the containing cell culture dish. By identifying an adhesion localized GTPase activating protein called cdGAP as regulatory key component of the mechanism involved in stiffness detection, research showed, that cells seeded into soft materials migrated towards the stiffer glass surface in vicinity of the original seeding point (Wormer et al. 2014). Therefore, every cell culture system based on attaching an extra cellular matrix substitute on a glass or plastic surface, i.e. with intrinsic stiffness gradients, needs to consider durotaxis as a phenomenon. Cell proliferation, for example, is but one aspect that is influenced by the migratory behaviour of cells, as is clearly demonstrated during the wound healing process (Zahm et al. 1997). More severely than the effect of the ongoing migration during durotaxis is the result: cells migrating towards the highly stiff glass or plastic surface end up inhabiting a microenvironment that resembles a two dimensional habitat more than a three dimensional. This can impact the results of experiments, for example in chemosensitivity assays. Chemosensitivity, as a term for the susceptibility of a cell to the action of a chemical agent, which is mostly used in describing the efficiency of a therapeutic drug, has been shown to decrease when incorporating cancer cells into an extra cellular matrix (Sethi et al. 1999).

1.3. Actin cytoskeleton

Actin plays a central part in many biological processes. As such actin is functional in, for example, cell division, cell movement, trafficking of membrane vesicles, providing internal support and sensing of environmental forces. Early on, most of the general knowledge about the mechanism and function of actin was gained by research on muscles and muscle cells (Szent-Györgyi 2004).

During cell migration, polymerization of actin is tightly regulated by many regulatory proteins. However, the basic mechanism of actin polymerization is fairly simple. ATP binding monomeric subunits of actin, called G-actin (globular) spontaneously self-assemble into polar and helical filaments of F-actin (filamentous) by binding to the so called (+)-ending of the filament. This binding step is faster than the hydrolysis and subsequent dissociation of ADP binding monomers at the (-)-end of the filament, resulting in an overall growth of the F-actin filament. Associated proteins like profilin, cofilin and the Arp2/3-complex regulate the equilibrium between F-actin formation and disassembly (Pollard and Cooper 2009).

The actin cytoskeleton shows vast differences when comparing cells grown in two dimensional and three dimensional surroundings. In fact, the archetypical actin structure, the so called stress fibers are mostly limited to cells growing and migrating on planar surfaces, whereas cells cultivated in an extracellular matrix show a distinct lag of stress fibers and instead showed a diffuse distribution of actin throughout the cell plasma with more intense immunofluorescence in filopodia and lamellipodia (Tomasek et al. 1982).

1.4. Fluorescence recovery after photobleaching (FRAP)

Cellular parameters are the most direct way to assess the effects different cell culture conditions have on the cells. Methods to measure cellular parameters *in vitro* are of microscopical nature. FRAP as a fluorescence based method readily

offers an insight into membrane dynamics and is therefore used to investigate the effect of the cell culture system on the plasma membrane.

First introduced in the 1970s (Axelrod et al. 1976), FRAP is a microscopic technique used to measure the two dimensional lateral mobility of particles. By focusing a high intensity laser beam on a small and defined region, fluorophores inside this region are irreversibly bleached, resulting in a dark spot. Due to the mobility of the surrounding specimen, recovery of the fluorescence occurs. Quantitative evaluation of this fluorescence recovery affords information about (i) the mobility of the fluorescent specimen in the given surroundings and (ii) the mobile fraction, viz. the amount of mobile molecules.

Assuming mobility is based solely on Brownian motion – thus ignoring directed transport and flow – and neglecting fluorescence recovery due to inflow of specimens from above and below the bleached area, mobility of the fluorescent specimen can be described by the following equation (1):

$$\tau_D = \frac{\omega^2 \gamma}{4D} \quad (1)$$

where τ_D is the diffusion time, D is the diffusion coefficient, ω is the radius of the bleached region and γ is a correction factor for the amount of bleaching. This formula is applicable for FRAP experiments in thin films, such as liquid layers and membranes. η

In general, diffusion is described by the Stokes-Einstein equation (2):

$$D = \frac{kT}{6\pi\eta R_h} \quad (2)$$

where k is the Boltzmann constant, T is the absolute temperature, μ is the viscosity of the solution and R_h is the hydrodynamic radius of the diffusing particle.

The introduction of GFP as tool for life cell imaging and fluorescent reporter protein increased the applicability of FRAP studies on living cells (Reits and Neefjes 2001; Niv et al. 2002; Sukhorukov et al. 2010; Luu et al. 2012).

1.5. Understanding the basic principle of Deconvolution – Outline of image formation

The optical properties of the specimens investigated throughout this work require and highly benefit from a microscopic tool set that is developed and redefined to counteract the detrimental effects in imaging caused by thick and scattering samples. Image post processing especially in fluorescence microscopy offers tools to improve image quality, resulting in better images and – more importantly – quantifiable parameters that are closer to the true facts of the matter. The most advanced tool producing the least amount of artefacts for image post processing is deconvolution.

1.5.1. Point Spread Function and the effect on image formation in light microscopy.

The Point Spread Function describes, how a point like object is recorded by a given imaging system. Due to the diffraction of light occurring during imaging, a point source of light is not recorded as a point, even when in focal plane. Instead, the commonly as airy pattern termed diffraction pattern is recorded. The shape of this Airy disk depends on the Numerical aperture of the objective and the wavelength of the light. The shape of the Airy disk is described by the point spread function (PSF), which can either be measured by using sub-resolution (and therefore point-like) objects or can be described theoretical. The PSF describes and determines the resolution of an optical system. The so called Rayleigh criterion (Rayleigh 1879; Rayleigh 1903) describes the resolution in classic fluorescence microscopy and states that two objects can only be identified as individual objects if the intensity maximum of the airy pattern of one object lies within the first intensity minimum of the airy pattern of the other object. The Rayleigh resolution can be calculated using the equation (3):

$$d = \frac{0,61 \lambda}{NA} \quad (3)$$

where NA is the numerical aperture, λ is the wavelength of the emitted light and d is the resolution distance.

Any part of an object is transformed by the PSF and together yields the final image.. This, diffraction based, blurring or convolution of the image is described in Figure 1 (obtained from Sibarita 2005). The blurring of the image by the PSF of the imaging systems leads to a broadening of the intensity profiles and to a decrease in intensity maximum. This in itself is a burden for the detection of objects. Combined with the random effect of noise, this can result in the loss of signal, especially in the case of small objects (see Figure 1F).

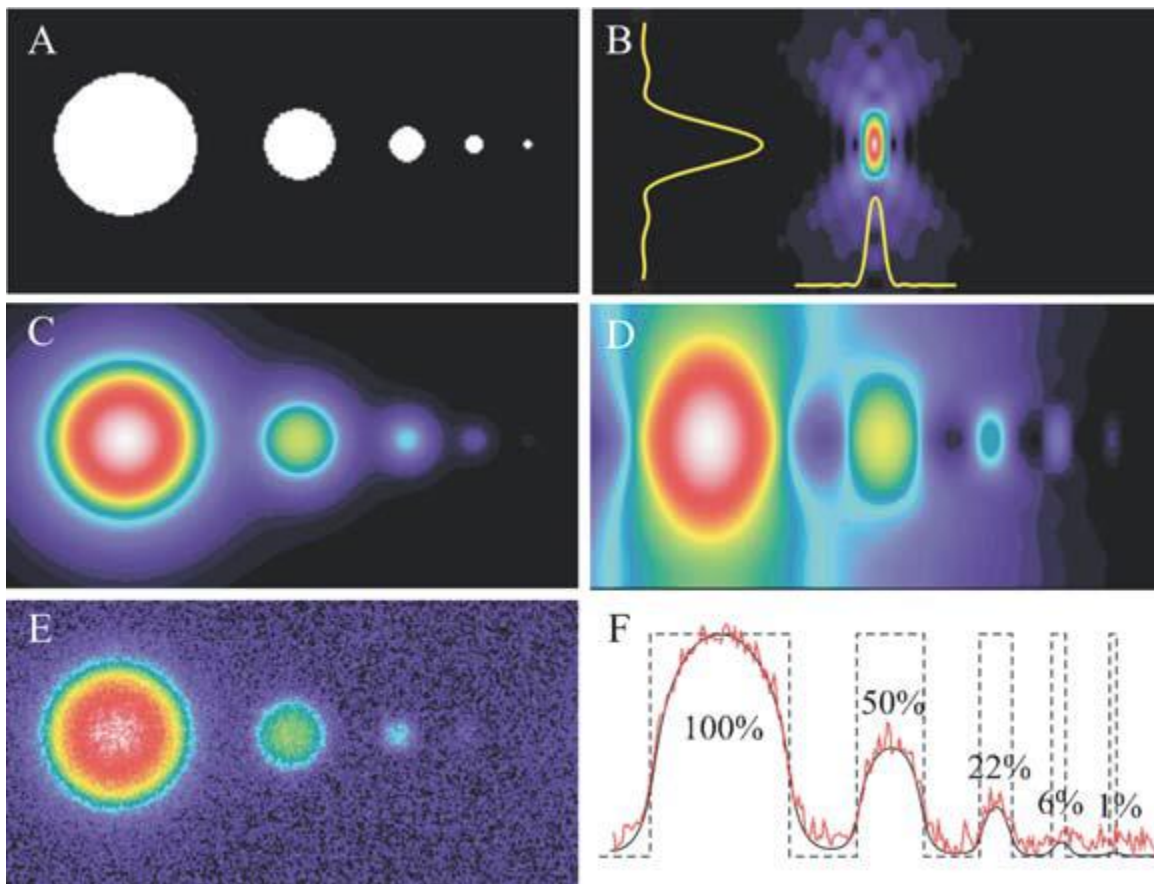


Figure 1: Effect of the PSF on the image formation during light microscopy

A) Five spherical object with the same intensity. B) PSF of the imaging system. C) Lateral and D) axial blurring of the object based on the PSF of the imaging system. E) Addition of noise and F) intensity profiles of the unaltered object (dashed black line), the convoluted image (black line) and the convoluted and noisy image (red line). After Sibarita (2005).

Image formation is further complicated by the fact, that a PSF is subjected to changes throughout a three dimensional specimen, due to spherical aberration as a result of different refractive indices. This leads to an axial asymmetry of the PSF and a decrease in its intensity (see Figure 2).

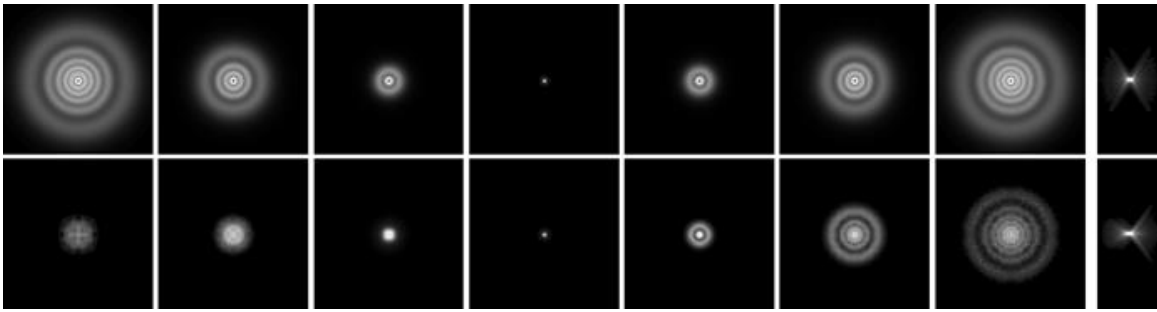


Figure 2: Optimal, theoretical vs empirical PSF

PSF of an aberration free, theoretical objective; bottom) empirical PSF of an 100X, 1.4 NA oil objective. After Sibarita (2005).

1.5.2. Principle of deconvolution

The benefit of deconvolution can immediately be understood, if one understands the principle of an imaging event. During image acquisition the image gets distorted due to inherent properties of the imaging system, based on the point spread function. This can be described with the following equation for image formation (5):

$$(5) \quad \text{Image} = \text{Object} \times \text{point spread function}$$

Simply put, deconvolution is the reversal of the image formation described in equation (5). By using the information of the PSF (which can either be calculated or measured by imaging sub resolution sized beads under identical imaging conditions as for the measurement of the actual object), deconvolution allows for the restoration of the object. By understanding the causes for image degradation and implementing reversal-steps into a computational image processing step, deconvolution basically aims to reassign blurred or out-of-focus light to its source and by doing so increases the contrast and resolution of any given image. As such, deconvolution is greatly beneficial in widefield fluorescence microscopy but can also improve the already contrast enhancing capabilities of a confocal fluorescence microscope.

1.6. Paper as a platform for functional devices

Paper is an integral part of everyday life and is used globally for several centuries. Despite being around for such a long time, the man-made material is almost exclusively used as an information storage and distribution device. However, the structural and mechanical properties of the cellulose polymer, the most abundant biological compound on earth (Klemm et al. 2005), make paper a versatile material for other applications as well. In these, paper is used as a platform which is augmented by additional functional properties, often introduced by printing processes or via chemical modifications performed ahead or after the paper production process. Such modifications have successfully been applied to transform paper into electronic and sensoric devices (Tobjörk and Österbacka 2011; Zheng et al. 2013) or even a fully functional microscope (Cybulski et al. 2014). Mechanical strength can be altered by additives (Lindström et al. 2005), whereas wettability and the capability to swell may be modified by waxes or hydrophobic polymers (Carlmark and Malmström 2003).

Among the diverse set of functionalities, the development of paper-based microfluidics has seen particular attention (Li et al. 2012). By dividing paper into hydrophilic and hydrophobic zones, a versatile system to transport, mix and analyze fluids is achieved with relatively low effort but all the more usability for lab-on-a-chip and diagnostics applications. In particular, the low cost of the basis material makes paper-based devices particularly suited for scaled applications, such as screenings for health monitoring and diseases (Martinez et al. 2007; Martinez et al. 2010), pharmacological screenings (Derda et al. 2009; Deiss et al. 2013), or as blood sampling devices (Li et al. 2013).

Many different approaches have been used to build liquid repellent and transporting areas within the paper matrix. Blocking of pores with wax-like substances (Carrilho et al. 2009; Coltro et al. 2010) followed by local removal of the wax via plasma treatment (Li et al. 2008) or the direct modification of cellulose fibers via the photo-chemical attachment of functional polymers (Böhm

et al. 2012; Böhm et al. 2013) or plasma etching (Balu and Kim 2009; Balu et al. 2009) are all examples for post-production modifications. Alternatively, modifications may also be introduced ahead of the paper production step, as demonstrated by the use of functionalized cellulose fibers, e.g. for the generation of hydrophobic fibers (Geissler et al. 2013).

1.6.1. Further development of functional paper

In view of the unique set of properties accompanied with using paper as a platform for functional devices, further development, optimization, and application of these systems for an even broader range of uses is clearly desired. However, for the advancement of functionalized paper devices to be effective and efficient, the relations between structure and function of the material need to be known in detail. Only then is it possible to derive a rational process for the production of functional papers with predictable properties. Therefore precise and quantitative analytical tools are required, which allow to obtain information about the *structure* of paper, the *components* functionalized paper may be composed of as well as *dynamic processes*, it may host as a functional device. Preferably, it should be possible to measure all these aspects simultaneously and non-invasively. Only with such tools, the relationship between production and modification processes and their effects on the functional properties of the resulting paper sheet, can be assessed. Paper, however, is a heterogeneous and thus complex structure, which therefore poses a challenge for the methodological approach to obtain qualitative structural, compositional, and dynamic information.

1.6.2. Structural analysis of paper

Of these three qualitative aspects to describe paper (i.e. structure, components and dynamics) investigations of the structure have seen by far the most attention. To investigate the spatial structure of paper, microscopy is clearly the method of

choice and, consequently, all three major fields of microscopy, namely optical, electron and scanning probe microscopy have been applied.

Optical microscopy has a clear advantage over other techniques, as it allows for nondestructive investigations of specimens. Confocal microscopy combines this benefit with the capability to acquire optical sections by rejecting out-of-focus information from the final image. It is therefore especially suited in the analysis of specimens with a complex 3D structure. Not surprisingly, confocal laser scanning microscopy (CLSM) has often been applied for structural analyses of paper. Already two decades ago, the structure of single fibers (Jang et al. 1992) and entire paper sheets (Moss et al. 1993) were analyzed by confocal imaging. Later, more and more complex aspects of paper were addressed, e.g. the distribution and orientation of fibers (Xu et al. 1997), macropore structures (Dickson 2000), or back trap mottle of coated paper (Ozaki et al. 2006). Recently, the behavior of paper as a functional device was characterized using the popular imaging technique in a study on the transport behavior of free and agglutinated red blood cells inside a paper network (Li et al. 2013).

Especially in the context of thick and highly scattering specimens, of which paper is an excellent example, confocal microscopy faces its limitations as both lateral, but in particular axial resolution quickly degrades with imaging depth. To address this fundamental limitation, Bauer and coworkers have taken a proven approach to investigate thick specimens but combined it with a remarkable precise, versatile, and all the more successful implementation. By taking optical microscopic images of serial paper sections in a fully automated approach, not only the three-dimensional position and orientation, but also the cross-section morphology of the cellulose fibers is readily obtained with a precision, exceeding the confocal approach (Wiltsche et al. 2006; Wiltsche et al. 2011; Lorbach et al. 2012). The advantage in resolution, however, is gained by the loss for a nondestructive investigation of paper. The same holds true for electron microscopy, another method providing exceptional spatial resolution, which has mainly been used to study the surface structure of individual fibers (Svensson and

Aronsson 2003; Chinga-Carrasco et al. 2009). A combination of a nondestructive investigation method with precise 3D structural information with high resolution is so far only obtained with X-ray micro tomography (Samuelsen et al. 2001; Antoine et al. 2002; Marulier et al. 2012).

Finally, scanning probe, also known as atomic force microscopy provides a very detailed and more or less nondestructive view on the surface structure of untreated samples (Persson et al. 2013). Notably, the latter technique also allows addressing of functional questions, e.g. the mechanical investigation of fiber-fiber connections which are not accessible by any other technique. A specifically designed sample holder was used in combination with atomic force microscopy to measure the strength of fiber-fiber bonds (Schmied et al. 2012). Formerly bonded areas were also imaged using AFM and SEM (Fischer et al. 2013).

All in all, a great variety of microscopy techniques is available for the analysis of the spatial structure of paper, each of which is able to deliver a certain spatial resolution in dependence of the specimen's dimensions and the requested field of view.

1.6.3. Requirement for compositional and dynamic analyses of paper

In addition to the pure structure of the paper matrix, information about the chemical identity and quantity of functionalization, as well as the analysis of dynamic parameters, are also important aspects for the characterization of chemically modified paper. Hence, methods providing chemical specificity are required, in order to distinguish the modifications from the underlying cellulose based paper fibers and to identify their spatial relationship. Raman microscopy, is an example for an imaging method that fulfills the demand for spatial resolution, sensitivity, and chemical specificity. The method can be applied to distinguish and identify several chemical distinct compounds as they are found, e.g. in coated papers, in a nondestructive way and in absence of any additional labels (WITec 2000). It was used to study the deformation mechanisms of cellulose fibers in paper and wood (Eichhorn et al. 2001) and has proven its benefits in an analysis

of starch distribution in paper cross sections, where it achieved faster and more detailed results as the classical iodine-staining method (Pigorsch et al. 2013).

In principle, Raman microscopy also provides the temporal resolution required to investigate these examples. In particular coherent Raman imaging approaches, like stimulated Raman scattering (SRS) and coherent anti-Stokes Raman scattering (CARS), significantly increase weak spontaneous Raman scattering. Thereby, the virtues of Raman imaging, providing optical sectioning capability and imaging contrast in absence of extrinsic labels, become available for video-rate imaging (Ozaki et al. 2012; Ideguchi et al. 2013; Freudiger et al. 2014) and have been applied in microscopic analyses of structured carbohydrates (Slepkov et al. 2010).

Still, processes with an even higher demand for temporal resolution exist. An even better characterization of paper coatings, for example, could be achieved by a spatiotemporal analysis of the penetration process of starch and latex into the cellulose matrix paper (Ozaki et al. 2006), or the process of ink infiltration into paper fibers (Enomae et al. 2011). Another example is found in paper-based microfluidic applications, which recently came into focus. While fluid transport in paper microfluidic systems have been investigated by imaging approaches (Böhm et al. 2012, Lutz et al. 2013), analyses at high spatial and temporal resolution are missing.

1.6.4. Living cells and tissue: A specimen with similar demanding analytical requirements

The same exacting set of demands for high spatial resolution and molecular selectivity with the simultaneous ability to follow dynamic processes in a nondestructive way is also found for investigations on live cells (Swedlow 2012; Renz 2013). Especially in view of the recent developments to overcome the diffraction limit of optical resolution (Sahl and Moerner 2013; Han et al. 2013) and the integration of fluorescence microscopy in the context of high throughput screening approaches (Conrad et al. 2011; Singh et al. 2014; Haggarty and Perlis 2014), it becomes clear that the virtues of the technique for the investigation of paper will bring tangible benefits.

Notably, paper exhibits similar optical properties if compared to biological tissue or 3D cell cultures, respectively. Tissue, as well as paper samples, deteriorates the image quality due to a significant scattering of light, compromising both excitation profiles and detection efficiency. Moreover, the heterogeneous distribution of refractive indices poses challenges to imaging based approaches. Therefore, a set of approaches to counteract these discriminatory effects are in development. The progress that has been achieved to obtain high quality images for tissue and 3D cell cultures is directly applicable for the investigation of paper substrates. The most important methods to achieve high quality images of demanding specimens are deconvolution (McNally et al. 1999), selective illumination and detection (Verveer et al. 2007) and the use of adaptive optics (Jorand et al. 2012). All these techniques can readily be applied to improve imaging of paper by means of fluorescence microscopy.

1.6.5. Quantitative fluorescence microscopy for multi-parameter analysis of paper

Widefield and confocal fluorescence microscopy in providing a tool for the analysis of chemically modified paper sheets offer capabilities to simultaneously provide high spatial and temporal resolution, while maintaining exceptional sensitivity, i.e. radiometric resolution. Through extrinsic labeling, also chemical specificity is achieved, which allows to distinguish individual components in a modified paper sheet with high contrast in all spatial dimensions. To further demonstrate that all above mentioned benefits are also available *in-situ*, as the nondestructive analysis of the method allows for characterization of dynamic processes in solvated systems, the methodical framework is applied to the analysis of an exemplary paper-based model system.

To this end lab-engineered paper substrates were analyzed, which are modified by spatially controlled chemical adsorption of a hydrophobic polymer to the cellulose fibers (Böhm et al. 2014), as the characterization of such a microfluidic system draws on all qualities of the method. Specifically, the distribution of the rhodamine labeled polymer in relation to calcofluor white labeled cellulose sheets was determined with high selectivity and spatial resolution. Likewise the static and dynamic distribution of a FITC labeled dextran solution inside the polymer coated fiber network was monitored.

Examples are provided, which exploit all four types of resolution provided by fluorescence microscopy, namely radiometric (amount of polymer), spatial (distribution of polymer), spectral (separation of cellulose, polymer and fluid), and temporal resolution (fluid propagation in paper) and thereby present a proof of concept to demonstrate how the capabilities of fluorescent microscopy help in the analysis of polymer-modified paper.

2. Materials and Methods

2.1. Cell culture preparation

2.1.1. Cell culture

OV-MZ-6 cells were cultured in Dulbecco's modified eagle media (DMEM high glucose, GlutaMAX containing, 4,500 mg/mL glucose and pyridoxine, without sodium pyruvate (Invitrogen). Media was supplemented with 10 mM 4-(2-hydroxyethyl)-1-piperazineethanesulfonic acid (HEPES) buffer (Invitrogen), 0.55 mM L-arginine (Sigma Aldrich), 0.272 mM L-asparagine (Sigma Aldrich, Australia), 20 µg/mL Gentamycin (Invitrogen), 1% penicillin/streptomycin (pen/strep) (Gibco, Australia) and 10% foetal calf serum (FCS)(Gibco, Invitrogen). Cells were cultured for 3 to 4 days at 37 °C/ 5% CO₂ till reaching 60-80% confluence. Cells were detached using 0.2 g/L Ethylenediaminetetraacetic tetrasodium (EDTA(Na₄)/PBS (Versene, Invitrogen), washed with PBS and centrifuged for 5 min at 1200 rpm. Cell pellet was carefully resuspended in fresh media and required amount of cell suspension was transferred into a new cell culture flask.

2.1.2. (3-Aminopropyl)trimethoxysilane (APTMS) surface modification of coverslips

The modification of glass or other silica surfaces with functionalized silane is a commonly used method which has for example been used to perform atomic force microscopy studies on DNA (Hu et al. 1996), to immobilize enzymes in a microchannel (Miyazaki et al. 2003) and to functionalize otherwise inert carbon nanotubes with an adsorbent property (Yu et al. 2007). The benefit of silanization

of a silica surface is found in the bifunctionality of the used silane compound. The widely used (3-Aminopropyl)-triethoxysilane and (3-Aminopropyl)-trimethoxysilane offer two distinct reaction sides. Firstly, the alkoxy groups are capable of covalently binding to an inorganic surface, such as glass. Secondly, the bifunctional amine can directly interact with an organic substrate and form covalent bonds. Additionally the amine can be further modified, for example by treatment with succinic acid anhydride to yield reactive carboxyl groups. Other bifunctional group in use include but are not limited to thiols and epoxids.

Silanization requires the hydrolysis of the alkoxy groups, thus forming hydroxyl groups which can either form covalent bonds amongst each other or with hydroxyl groups present on the surface. Silanization can be done in a variety of ways: (i) Deposition from an aqueous/organic solvent, (ii) water soluble silanes can be deposited onto a surface from an acidified aqueous solution, (iii) highly reactive silanes can be deposited to a surface from organic solvents and (iv) vapor deposition is also possible (Hermanson 2008).

(3-Aminopropyl)trimethoxysilane (Sigma-Aldrich, Munich, Germany) was freshly prepared as a 2% (v/v) solution in acetone. 40 μ L of this solution was placed in the center of a glass coverslip. Previously in acetone cleaned coverslips were then placed on a SPIN150 spin coater (S.P.S. Vertriebs GmbH, Ingolstadt, Germany). A two-step spin coating protocol was applied: in the first step a slow rotation speed of 500 rpm was used for 30 s, followed by a second step with 3000 rpm for 30 s. Acceleration was set to 500 rpm/s. After spin coating of the APTMS, coverslips were vertically placed in a Teflon rack and washed two times in distilled water for 5 min followed by a drying step over night.

2.1.3. Collagen hydrogel preparation

Collagen, Type I solution from rat tail (Sigma-Aldrich, Munich, Germany) was used as a chilled solution. Collagen hydrogel preparation was conducted on ice in order to prevent premature polymerization. Collagen stock solution with a

concentration of 3 mg/mL was diluted with 10xPBS and cell suspension to achieve hydrogels with a final collagen concentration of 2 mg/mL. Beforehand, cell suspension was diluted to achieve a suspension which allowed for a desired cell number in the final collagen gel. Finally, 7.5 % NaHCO₃ was used to adjust the acidic collagen solution to a pH value of 7.4. 20 µL of the final collagen gel solution was then centrally placed on the APTMS coated coverslips (see 2.2.1.). Polymerization of the collagen network took place for 30 min at 37 °C. After polymerization collagen hydrogels containing cells were submerged in cell culture medium containing serum.

2.1.4. Plasmid isolation

LifeAct-tagRFP (ibidi, Martinsried, Germany)) and CAAX-mCherry (pCDNA3.2) plasmids were amplified in *E.coli* DH5α strain and isolated using the GenElute™ HP Plasmid Midiprep Kit (Sigma-Aldrich, Munich, Germany).

2.1.5. Actin cytoskeleton labeling with LifeAct-RFP

LifeAct-tagRFP plasmids were used to visualize the actin cytoskeleton of cells. Cells were transfected using Genejuice® (EMD Chemicals Novagen, Darmstadt, Germany). Cells were seeded either on glass surfaces or in collagen hydrogels (see 2.2.2.) the day before transfection. For each transfection 100 µL serum-free culture medium was placed in a 1.5 mL tube. 3 µL of Genjuice were added to the medium. After 5-10 min of incubation 1 µg of the LifeAct-tagRFP plasmid was added. The solution was then gently mixed by pipetting and incubated for another 15 to 20 min. Finally, the transfection solution was dropwise pipetted to the cells. Transfection results were imaged 24 h after the transfection took place.

2.1.6. Plasma membrane labeling with CAAX-mCherry

CAAX-mCherry (pCDNA3.2) plasmids were used to visualize the plasma membrane of OVMZ-6 cells. Cells were transfected using Genejuice® (EMD Chemicals Novagen, Darmstadt, Germany). Cells were seeded either on glass surfaces or in collagen hydrogels (see 2.2.2.) the day before transfection. For each transfection 100 µL serum-free culture medium was placed in a 1.5 mL tube. 3 µL of Genejuice® were added to the medium. After 5-10 min of incubation 1 µg of the CAAX-mCherry plasmid was added. The solution was then gently mixed by pipetting and incubated for another 15 to 20 min. Finally, the transfection solution was dropwise pipetted to the cells. Transfection results were imaged 24 h after the transfection took place.

2.1.7. Plasma membrane staining with Vybrant® Multicolor Cell-Labeling Kit

The Vybrant® Multicolor Cell-Labeling Kit (Life Technologies GmbH, Darmstadt, Germany) contains three different carbocyanine dyes: DiO, DiI and DiD with respective emission maxima at 501, 565 and 665 nm. For plasma membrane staining, cells were temporarily suspended in 1 mL serum-free culture medium. 5 µL of the dye DiO was added, followed by gentle mixing with the pipette. After 15 min of incubation, the best staining result was achieved and the cells were centrifuged for 5 min at 2000 rpm, followed by two washing steps with prewarmed culture medium. Finally, cells were either seeded on glass coverslips or used for collagen preparation (see 2.2.2.).

2.2. Imaging setup and image analysis

2.2.1. Imaging of actin cytoskeleton and cell distribution

Imaging of the actin cytoskeleton and the migration behavior of cells cultivated in collagen was performed by using a Leica SP5II confocal laser scanning microscope (Leica Microsystems GmbH, Mannheim, Germany). Laser line wavelength used for the excitation of LifeAct-tagRF was 561 nm and for H2B-GFP and DiO 488 nm/561 nm. The collagen network was imaged in reflection mode using the 458 nm laser line.

2.2.2. FRAP experiments parameters

FRAP experiments of CAAX-mCherry was conducted with the LEICA SP5II by using a 561 nm laser. Five pre-bleach images were recorded with a frame interval of 38 ms, followed by bleaching with a zoomed in region of interest (ROI) for 10 frames with an interval of 38 ms. 60 Post-bleach images were acquired with a time resolution of 38 ms, followed by 30 post-bleach images recorded with a time resolution of 2 s and finally 15 post-bleach images with a frame interval of 5 s were recorded, resulting in 105 post-bleach images for 137.28 s after bleaching.

2.2.3. Image segmentation for investigation of cell distribution

After optical sectioning of collagen hydrogels containing cells by confocal laser scanning microscopy, image stacks were divided into 30 μm sub-stacks. Each image slice of these stacks was thresholded and converted into a binary image, with signal pixels set to a value of 1 and background pixels set to a value of 0 (See Figure 3 for a summary of the analysis work flow). A sum slice projection was performed using ImageJ (Image > Stacks > Z Project). This resulted in a

projection image in which the intensity of all pixels at the same position in any given slice of the stack are summed up. Automatic counting of the signal pixels is then used to quantify the cell distribution. This approach counteracts the intensity loss in deeper regions of a three dimensional specimen. Relative pixel distribution was calculated by dividing the pixel count of any given sub-stack with the combined amount of pixels counted in all sub-stacks. Image stacks were recorded over a total depth of 210 μm , thus, each image stack was divided in 7 sub-stacks.

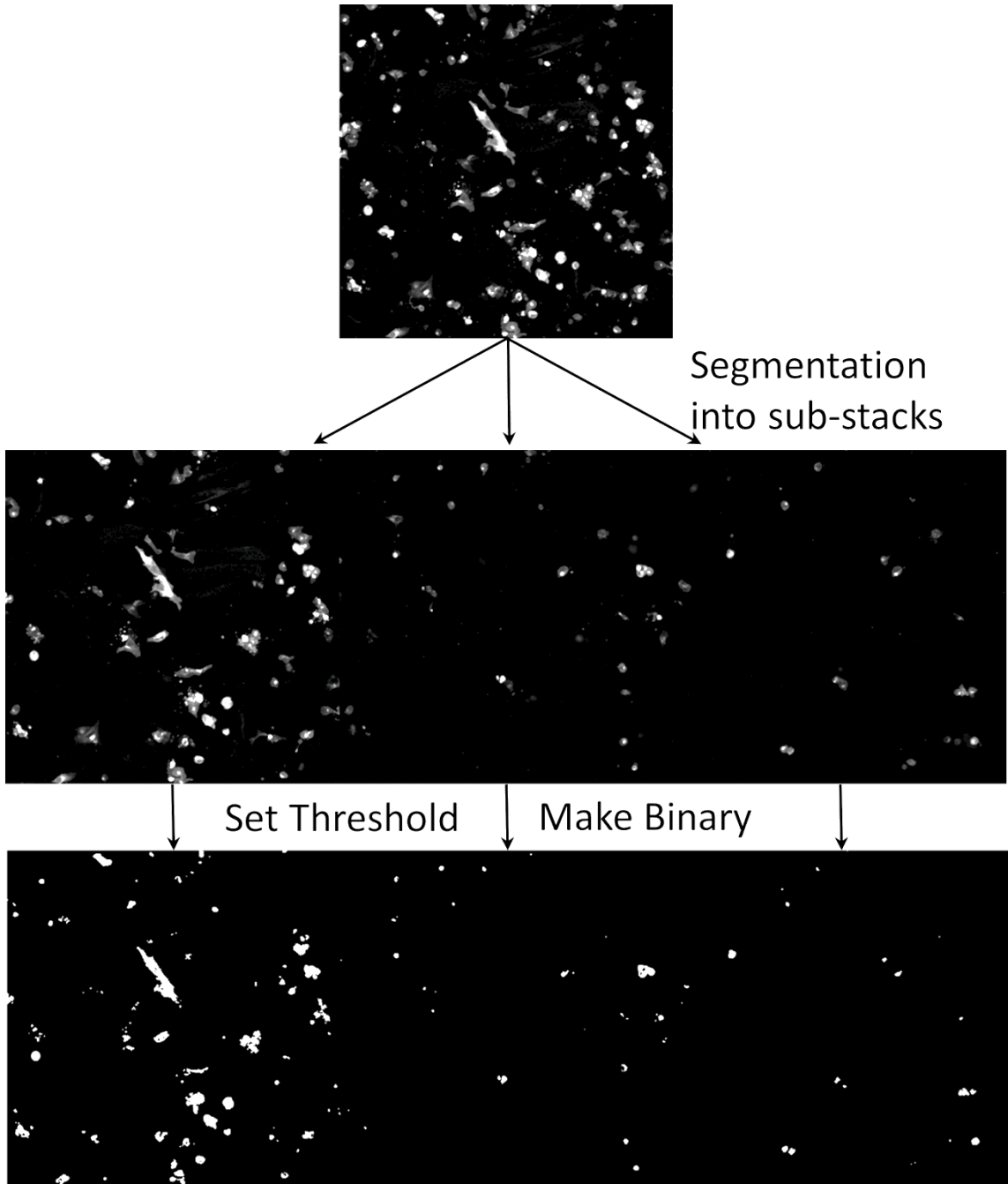


Figure 3: Workflow for the analyses of cell distribution inside a collagen hydrogel
Images were recorded with a HCX PL APO 20x/0.7 objective.

2.2.4. Widefield epifluorescence microscopy and image analysis of paper samples

Brightness and edge sharpness of the P(MMA-co-MABP-co-RhBMA) polymer spots were measured with conventional widefield epifluorescence microscopy. Samples were excited with a metal halide lamp (Prior Lumen 200 Pro, Prior Scientific, Jena, Germany) through an excitation filter (BrighLine® HC 563/9, Semrock, Rochester, NY, USA) with an illumination power of 1.5 mW and an exposure time of 50 ms. Images were acquired with a Nikon CFI Plan Fluor 4x, N.A. 0.13 objective, filtered by an BrightLine HC 612/69 filter (Semrock, Rochester, NY, USA) and detected with a back illuminated Andor iXon^{EM+} DU-897 EMCCD camera (Andor, Belfast, Ireland). Microscope hardware and image acquisition were controlled using Micromanager (Edelstein et al. 2010).

Integrated fluorescence intensities of the spots were quantified using Fiji (Schindelin et al. 2012), a distribution of ImageJ. The region of interest (ROI) for the quantification was selected on unprocessed images using the default auto-threshold method of ImageJ, which is based on the isodata algorithm (Ridler and Calvard 1978). The unprocessed image (Fig. 4a) was then divided by the binary image (Fig. 4b), thereby leaving the threshold area in the unprocessed image unchanged, while setting all remaining areas to zero (Fig. 4c). To assure that this operation works properly, the “Divide by zero value” has to be set to zero in the Fiji options (Edit > Option > Misc) and a 32-bit output has to be selected when dividing images with the „Image Calculator” (Process > Image Calculator). In these images (Fig. 4c), the fluorescent intensity of a spot is obtained from the sum of all pixels.

To quantify the border roughness of a spot, radial sums were obtained with the ImageJ plugin “Oval Profile Plot” (Author Bill O’Connell), which sums intensity values along several radii of a circular selection. By using a binary image for this operation, the summed intensity values equal to the distance from the center to the border. First, holes in the binary image (Fig. 4b) were filled (Process > Binary > Fill Holes). The now closed area of a spot (Fig 4d) was selected, fitted to a

circle to obtain its center (Edit > Selection > Fit Circle), and enlarged, until the whole spot is enclosed (Edit > Selection > Enlarge). Radial sums were obtained in 1° increments. Finally, the border roughness of a spot was quantified by calculating the standard deviation for all 360 center-to-border-distances.

For video recordings on the widefield epifluorescence setup, an aqueous FITC-Dextran solution (c=0.1 mg/mL) was applied at one end of a 2 mm x 40 mm paper stripe, which was sandwiched between a microscope slide and a coverslip. Images were recorded at a frame rate of 30 Hz. For the quantification **via** ImageJ a 50 x 512 pixel sized region of interest was placed on the side of the image where the fluid entered the field of view. Intensity in this region of interest was measured for all slices of the image stack (Image > Stacks > Plot-Z-axis Profile). Normalized intensity was then plotted against the time.

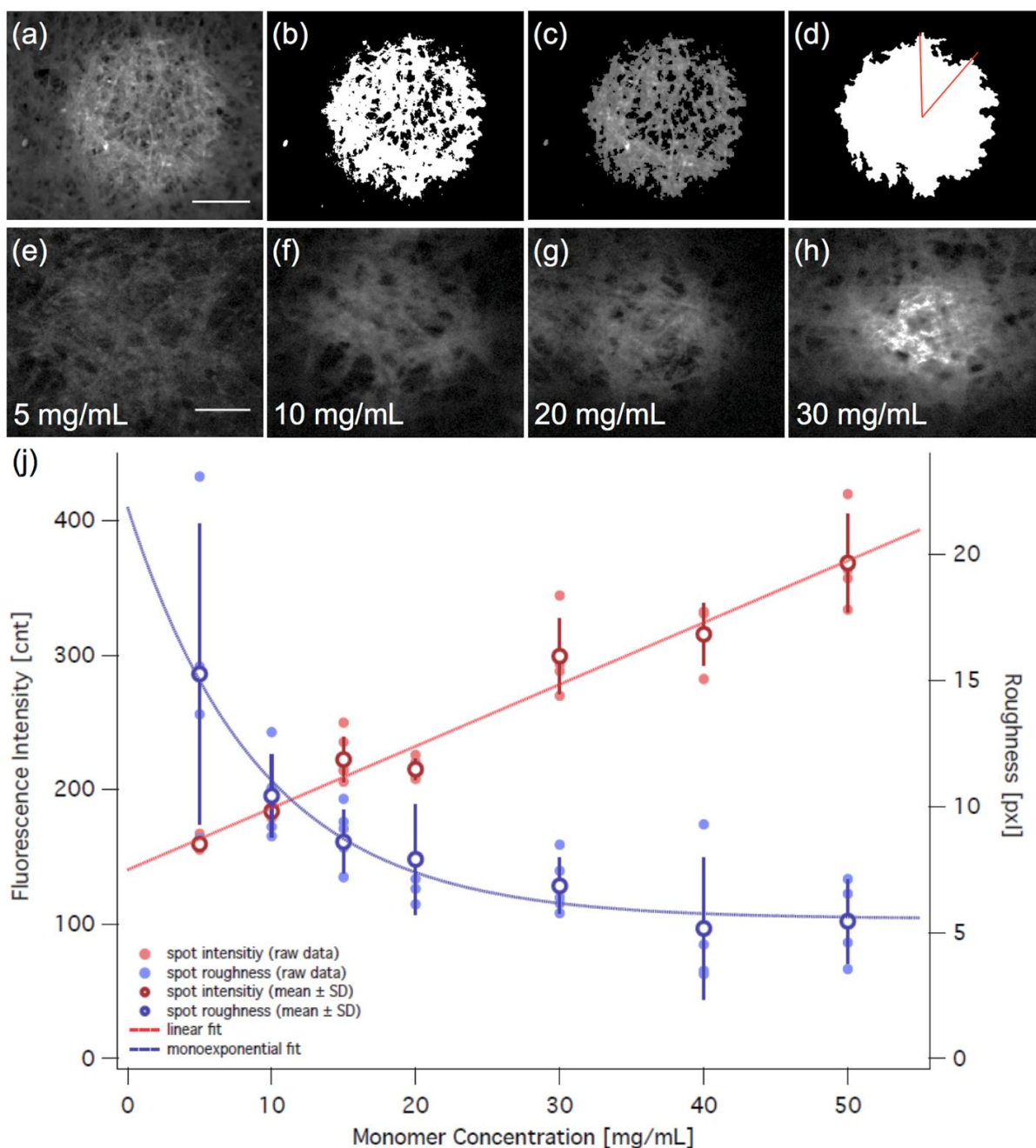


Figure 4: Radiometric and spatial quantification of polymer spot border roughness and intensity

Image processing steps performed before quantifying intensity values and spot border roughness. (a) Raw image data; (b) Thresholded image; (c) Noise and Background reduced image achieved *via* division of the raw image data with the thresholded image, which is used for intensity measurements; (d) Binarized image with all holes filled, which is used to quantify the spot border roughness. (e-h) Raw image data of fluorescent spots, produced with polymer solutions having different concentrations (5, 10, 20, and 30 mg/mL, respectively), were quantified using the image analysis procedure described in (a-d). While the total spot intensity shows a positive linear dependence on the polymer concentration (j, red symbols and line), the

border roughness decreases exponentially with the polymer concentration (j, blue symbols and line). Scale bars = 100 μm

2.2.5. Confocal Imaging of triple stained paper

Untreated paper was submerged into an aqueous solution of calcofluor white ($c = 0.02 \text{ mg/mL}$) and allowed to dry before it was modified with the PMMA-based fluorescent polymer, as described above. In a final step, the paper was brought into contact with an aqueous solution of FITC-Dextran ($c = 0.1 \text{ mg/mL}$) just before imaging was performed. Thereby, the solution was distributed inside the paper substrate due to capillary forces. A coverslip was placed on top of the samples in order to prevent desiccation during imaging. Confocal microscopic analysis was performed using a Leica SP5II confocal microscope (Leica Microsystems GmbH, Mannheim, Germany) equipped with a HCX PL APO 20x/0.7 objective. Samples were imaged by sequentially exciting each pixel line of the confocal scan with a 405, 488, and finally a 561 nm laser, corresponding to the excitation wavelengths of calcofluor white, FITC and Rhodamine B, respectively. Emission was sequentially detected between 420 and 470 nm (calcofluor white), between 500 and 550 nm (FITC-Dextran) and between 575 and 630 nm (Rhodamine-labeled PMMA). See table 2 for an overview of the fluorophores used in this study.

For confocal time-lapse sequences, an aqueous FITC-Dextran solution ($c = 0.1 \text{ mg mL}^{-1}$) was supplied at one end of a 2 mm x 40 mm paper stripe, which was pre-stained with calcofluor white ($c = 0.02 \text{ mg mL}^{-1}$) and sandwiched between two coverslips. Images were recorded with the resonant scanner. Again, sequential excitation was used as described above, but this time, only the 405 and 488 nm laser lines were used. Every line was averaged eight times, thereby sacrificing recording speed for achieving a significantly higher signal to noise ratio. Due to the fast scanning and switching of excitation wavelengths between scanned lines rather than frames, the time difference between the detection channels is negligible, if compared to the time scale for the movement of the fluid. In total, a frame rate of 1 Hz was achieved.

Table 1: Summary of Fluorophores used in this study and setup of image acquisition parameters during sequential imaging.

Fluorophores	Labeled Structure	□ _{Ex} [nm]	□ _{Ex} [nm]	Active laserline during image acquisition [nm]			Detection window during image acquisition [nm]	HyD Detector sensitivity setting [%]
				405	488	561		
Calcofluor White	Cellulose	405	452	✓	×	×	420 – 470	5 / 500
FITC	Fluid	495	518	×	✓	×	500 – 550	12 / 500
Rhodamine B derivative	Polymer	555	585	×	×	✓	575 - 630	20 / 500

2.3. Image post processing *via* deconvolution

2.3.1. Deconvolution Applications

The performance of several deconvolution applications was tested on different image stacks and the results were compared in regard to intensity profiles and subsequent isosurface render image generation. The following deconvolution applications were tested: (i) Iterative Deconvolution 3D (Dougherty 2005) and (ii) Deconvolution Lab, both of which are central processing unit (CPU) based deconvolution plugins for ImageJ; (iii) the graphical processing unit (GPU) based deconvolution plugin for ImageJ called CUDA (Compute Unified Device Architecture) Deconvolution Factory (Bruce and Butte 2013), and (iv) Huygens Professional (Scientific Volume Imaging, Hilversum, Netherlands).

Deconvolution was performed on a system with the following specifications: Windows 7 Professional 64-bit running on an 8-core 2.67 GHz Intel Core i7-920 processor with 24 GB RAM. The CUDA-Deconvolution plugin made use of a NVIDIA GeForce GT 610 graphics card (driver version 331.82 64-bit) or a NVIDIA GeForce GTX580 graphics card (driver version 331.82 64-bit).

2.3.2. Test Images

Deconvolution applications were tested on four different image stacks acquired with a confocal laser scanning microscope: (i) a high magnification image stack of a U2OS cell growing on a planar surface and transfected with the actin cytoskeleton marker LifeAct-RFP; (ii) a high magnification image stack of a U2OS cell growing in a collagen matrix for three weeks and transfected with the actin cytoskeleton marker LifeAct-RFP; (iii) P(MMA-co-MABP-co-RhBMA) coated paper and (iv) a collagen matrix labeled with E133 (see Table 1 for image properties). All four test image stacks were deconvolved using the deconvolution applications cited above (see 2.1.1.). Processing time was recorded and effectiveness of deconvolution was assessed *via* intensity plotting and evaluation of subsequent isosurface render images of the deconvolved image stacks.

Table 2: Properties of the test image stacks. All images were acquired as 16-Bit images.

Object	Name of objective; magnification; Numerical Aperture; immersion medium	Excitation Maximum [nm]	Emission Maximum [nm]	Image properties [$\mu\text{m} \times \mu\text{m} \times \mu\text{m}$]	Pixel size; lateral Resolution [pixel μm^{-1}]; No. of slices
U2OS cells expressing LifeAct-RFP on planar surface	HCX PL APO CS; 63x; 1.2; water	555	584	0.25 x 0.25 x 0.17	512 x 512; 3.93; 50
U2OS cells expressing LifeAct-RFP in collagen hydrogel	HCX PL APO CS; 63x; 1.2; water	555	584	0.4 x 0.4 x 0.29	512 x 512; 2.48; 105
P(MMA-co- MABP-co- RhBMA) coated paper	HCX PL APO lambda blue; 63x; 1.4; oil	555	585	0.25 x 0.25 x 0.25	512 x 512; 4.05; 91
Collagen matrix (2 mg mL ⁻¹)	HCX PL APO CS; 63x; 1.2; water	633	650	0.19 x 0.19 x 0.59	512 x 512; 5.324; 100

2.3.3. Generation of point spread functions (PSF)

Deconvolution requires a point spread function in order to restore an image. A PSF can either be measured by imaging microspheres under identical optical conditions as the actual specimen or it can be extracted from the image itself (blind deconvolution). Additionally, PSFs can be generated *in silico*. In this work the PSF Generator ImageJ plugin developed by the Biomedical Imaging Group at the EPFL was used (Kirshner et al. 2012) For a successful generation of a PSF with this software, knowledge over the numerical aperture of the objective, the refractive index of the immersion medium and the wavelength of the emission maximum is needed. For subsequent uses of the calculated PSFs it is necessary to generate them with the same image properties as the images that are to be deconvolved. Therefore, image sizes in pixels, stack depths as well as lateral and axial resolutions were specified, according to the properties of the respective images.

2.4. Paper modification

2.4.1. Monomer and polymer synthesis

The synthesis of the photoreactive monomer 4-methacryloyloxybenzophenone (MABP) was carried-out as previously described (Böhm et al. 2012). The fluorescent monomer rhodamine B methacrylamide (RhBMA) was synthesized in two steps from rhodamine B base (Shiraishi et al. 2007; Schäfer et al. 2013). All polymers described below were prepared by statistical free radical copolymerization and characterized with respect to molar mass and composition by size exclusion chromatography (SEC, PSS SDV linear M was used as column, THF as eluent and the system was calibrated using narrow dispersed polystyrene standards) and $^1\text{H-NMR}$ spectroscopy, respectively.

For the synthesis of P(MMA-co-MABP-co-RhBMA), methyl methacrylate (4.1 mL, 38.92 mmol) was added to 4-methacryloyloxybenzophenone (266.0 mg, 1.0 mmol) and rhodamine B methacrylamide (44.2 mg, 0.08 mmol) in 1,4-Dioxane (14 mL) in an Schlenk flask under nitrogen atmosphere. The initiator AIBN (19.2 mg, 0.12 mmol) was added and the solution was degassed by three freeze-pump-thaw cycles. The flask was placed in a thermostated bath at 60°C for 16 h for polymerization. After this time the polymer was precipitated in 500 mL methanol and dried in vacuum. The polymer was purified by reprecipitation with THF (25 mL) and methanol (300 mL). The polymer was obtained as a slightly pink solid (1.96 g, 47%), $M_n = 83.000$ g/mol. $^1\text{H-NMR}$ analysis yielded a molar composition of about 3.0 % mol of the photoreactive benzophenone group in the copolymer.

2.4.2. Preparation of lab-engineered and polymer-modified paper

For the preparation of lab-engineered paper substrates bleached, dry cotton linters was used. The pulp was refined in a Voith LR 40 lab refiner. After the refining, the cotton linters pulp had a SR (Schopper-Riegler Freeness) of 37. Refining was performed with an effective specific energy of 200 kWh/t. A series of paper sheets with grammages of 23.5 g m⁻² was made on a conventional Rapid-Koethen hand

sheet maker according to DIN 54358 and ISO 5269/2 and the prepared hand sheets did not contain any additives or fillers. The grammage, thickness (60 μm) and porosity (0.74; average pore radius: 12.8 μm) of the lab-engineered paper sheets were obtained as described in a recent publication (Böhm et al. 2014).

For the preparation of chemically modified model papers, the paper substrates were cut into pieces (2.5 x 2.5 cm). The P(MMA-co-MABP-co-RhBMA) copolymers were first dissolved in THF at a constant concentration of about 5, 10, 15, 20, 30, 40 and 50 mg/mL. The functional polymers were adsorbed to the paper by submerging the paper substrates into the polymer solution for approx. 20 sec (dip coating) followed by subsequent air-drying of the samples for approx. 30 min. After the polymers had been adsorbed onto the cellulose fibers inside the paper sheets, the samples were transferred to a Newport 1000W Oriel Flood Exposure Source ($\lambda = 365 \text{ nm}$) and illuminated with UV-light. All samples were illuminated with $E = 16 \text{ J cm}^{-2}$ at which approx. 94 % of the present benzophenone groups have reacted (Berchtold 2005). This energy dose corresponds to an illumination time of $\sim 16 \text{ min}$. In order to create surface micro patterns, appropriate metal masks were placed on top of the paper substrate during the illumination step. After the illumination, non-bound polymer was removed from shaded areas by a solvent extraction for 150 min in a Soxhlet apparatus using THF as solvent. All samples were air-dried for at least 15 h before they were further used. In a final step, samples were irradiated for approx. 20 min using an UV-Handlamp (6W) in order to convert the non-fluorescent, closed form of the RhBMA monomer into the fluorescent, open form (for details, see Schäfer et al. 2013). Figure 5 shows a schematic overview of the preparation process of the polymer-modified paper.

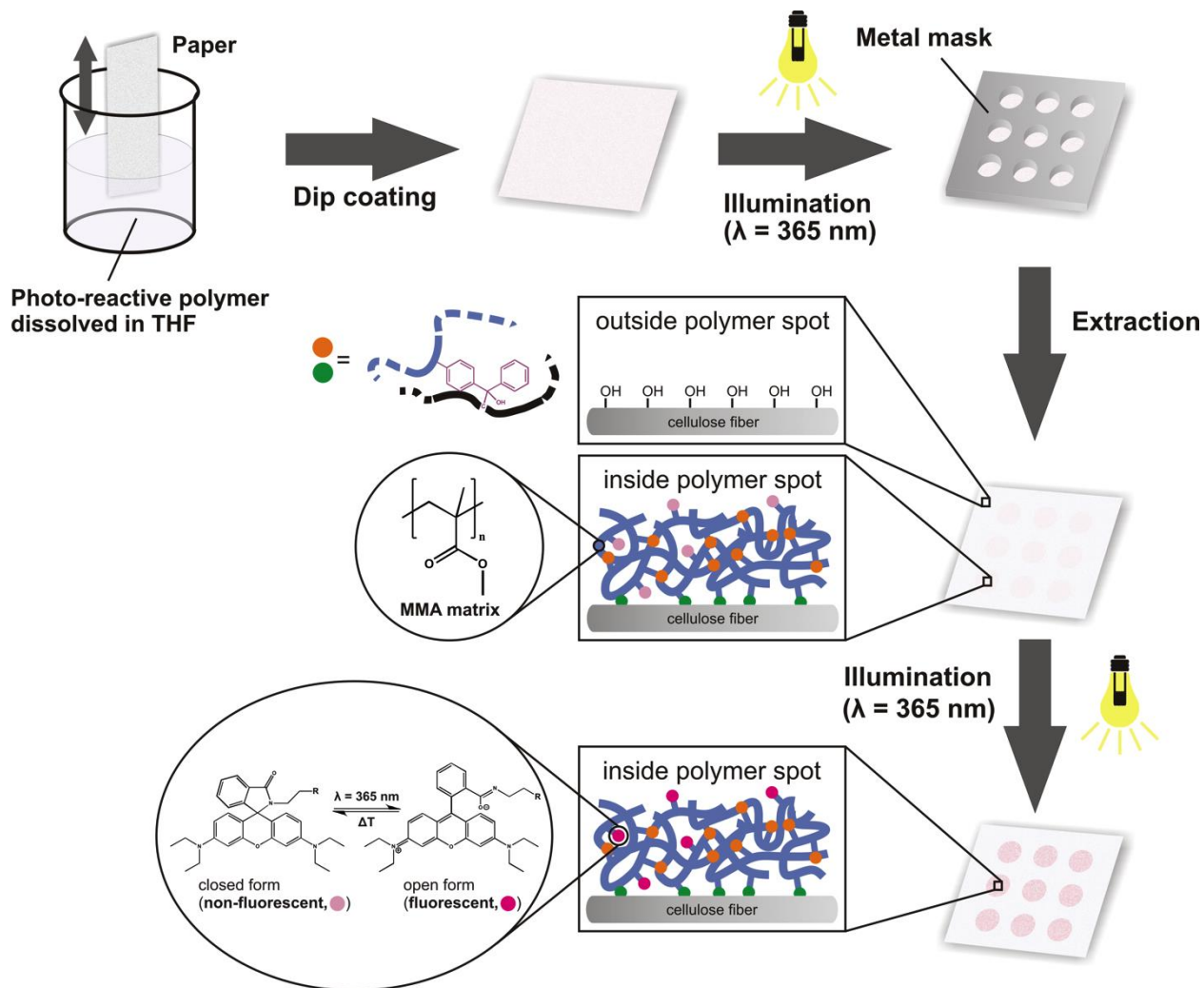


Figure 5: Photolithographic generation of hydrophobic, fluorescent micro patterns on paper

Schematic illustration of the process employed to create the polymer-defined spots inside paper substrates. Photoreactive polymers are first adsorbed onto the cellulose fibers using the dip-coating method. During illumination with UV light, a spot defining metal mask is brought into contact with the paper substrate; a surface-attached polymer network is formed in the non-shaded area through a photochemical reaction between the benzophenone group and the aliphatic C–H groups of the cellulose fibers (green dots) and other polymer segments in close proximity (orange dots) (for details of the photochemical reaction, see Böhm et al. 2012, Böhm et al. 2013). Development of the chemical micro-pattern is achieved by subsequent removal of non-bound macromolecules in shaded areas via solvent extraction. Finally, the Rhodamine B derivative incorporated in the PMMA-polymer is converted to its fluorescent state via irradiation with UV-light ($\lambda = 365 \text{ nm}$)

2.5. Flow experiments in paper

2.5.1. Widefield epifluorescence microscopy and analysis of flow experiments using FITC-Dextran and ethylene glycol tetraacetic acid (EGTA)

FITC-Dextran was diluted in an EGTA solution ($c = 0.5 \text{ mol/L}$) to achieve a final concentration of 0.1 mg/mL . $2 \text{ mm} \times 40 \text{ mm}$ paper stripes were washed with the same EGTA solution and subsequently thoroughly dried. The aqueous FITC-Dextran/EGTA solution was applied at one end of the paper stripe, which was sandwiched between a microscope slide and a coverslip. Images were recorded at a frame rate of 30 Hz .

2.5.2. Widefield epifluorescence microscopy and analysis of flow experiments using FITC-Isomer I

FITC Isomer I was diluted in acetone to achieve a final concentration of 0.1 mg/mL and was applied at one end of a $2 \text{ mm} \times 40 \text{ mm}$ paper stripe, which was sandwiched between a microscope slide and a coverslip. Images were

3. Results and Discussion

3.1. Comparison of deconvolution packages

During image acquisition information gets inevitably lost, due to the properties of the imaging system. Additionally out-of-focus signal contributes to the background of any given image, making it blurry and in consequence harder to discriminate individual features of the image. Beside and in addition to the use of sophisticated imaging methods such as confocal microscopy, deconvolution as a computational method can be applied to reduce this detrimental effects in order to restore and improve image quality. As an image gets recorded, convolution takes place as a consequence of the optical properties of the imaging system and the specimen. However, this in turn means, that with knowledge over these properties it is possible to invert the convolution. This mathematical operation is called deconvolution and can be of great aid in image restoration and in consequence in image analysis. A plethora of different software approaches for deconvolution are available as commercially distributed software or as freely distributed plugins for ImageJ. Four of these deconvolution approaches were compared: the commercially distributed (i) HuygensPro software and three Image J Plugins (ii) Deconvolution Lab, (iii) Iterative Deconvolution 3D plugin and (iv) CUDA Deconvolution Factory. This comparison aimed towards identifying the optimal trade-off in terms of deconvolution quality and processing time. Ultimately an imaging setup is desired, which is able to acquire images and perform image preprocessing steps necessary for subsequent image analysis, in a reasonable amount of time.

Deconvolution efficiency was evaluated visually by comparing the restored images of the four deconvolution applications and also by comparison of intensity profiles along a line placed at the exact same position in the original, unprocessed image and the restored images. Visual and intensity profile evaluation was done

for single slice images, resulting from the optical sectioning capabilities of the confocal laser scanning microscope and for maximal intensity Z-projections.

Finally, performance of the deconvolution software was estimated by recording the time needed for processing the images. For this, all image restoration was performed with 10 iterations, even though in some cases, better restoration results could have been achieved, if deconvolution was allowed to run for more iterations.

3.1.1. Intensity profiles as benchmark for image restoration quality

A visual comparison of the single slice images of the four test objects is shown in Figure 6. Starting with the GPU driven CUDA deconvolution, which performed the image restoration in a range from 0.7 s for the restoration of the U2OS cell cultivated on a planar surface image stack to 1.7 s for the restoration of the collagen hydrogel image stack, the restored images don't show a lot of quality improvement in terms of contrast and signal to noise ratio, which is especially pronounced in the collagen hydrogel images. This becomes even more obvious when looking at the intensity profiles shown in Figure 6 and Figure 7. In all four test objects the intensity profiles from the CUDA deconvolution show a big similarity with the intensity profiles of the unprocessed images. While this shows that very little artifacts are introduced during image restoration it has no beneficial impact on down-stream image processing steps which are based on setting intensity thresholds like, e.g., surface rendering.

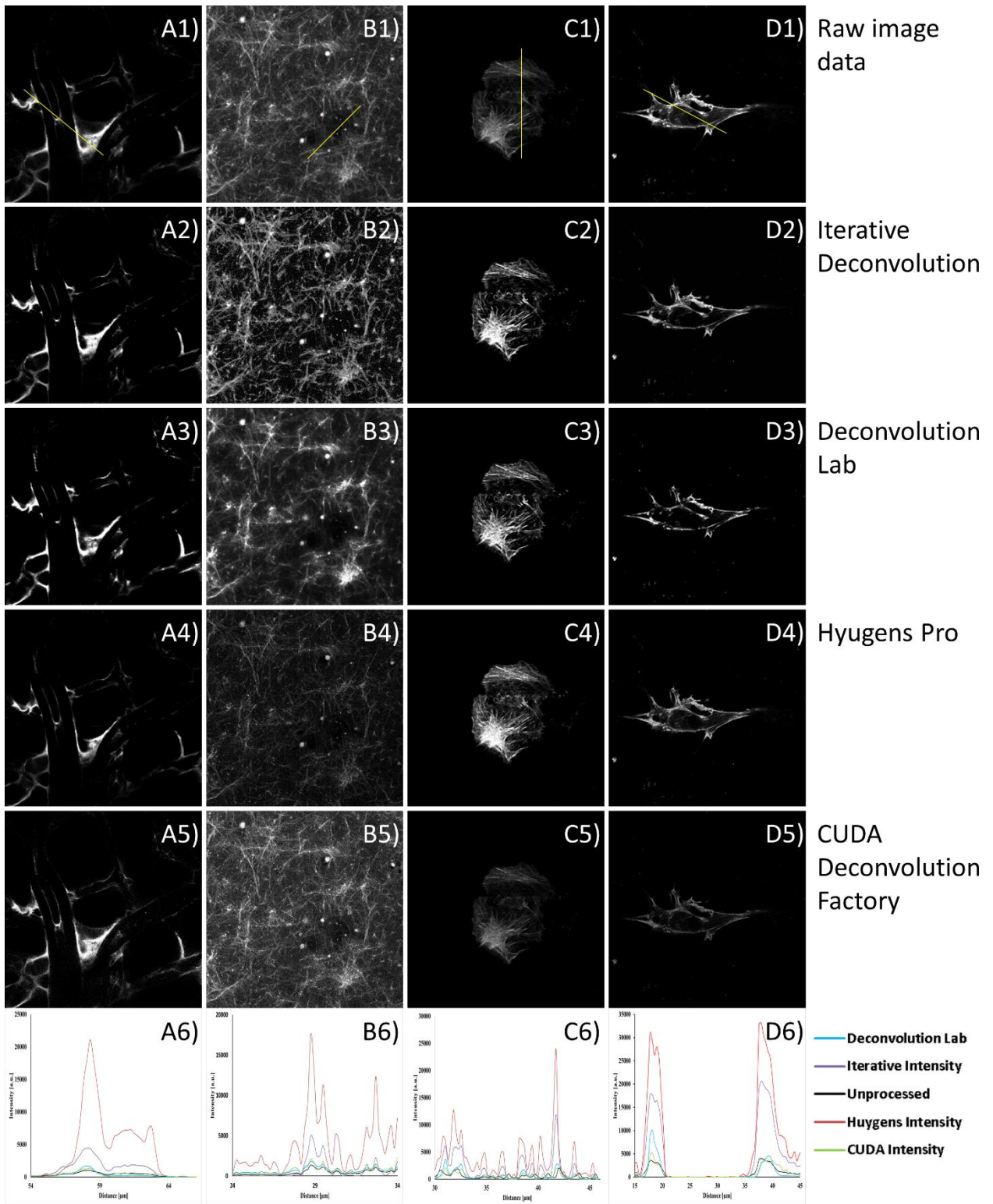


Figure 6: Single Slice images of a P(MMA-co-MABP-co-RhBMA) coated paper

(A1) Raw image; (B1) Raw image of a collagen hydrogel with a concentration of 2 mg ml⁻¹; (C1) Raw image of a U2OS cell transfected with LifeAct-RFP cultivated on a planar surface; (D1) Raw image of a U2OS cell transfected with LifeAct-RFP cultivated in a collagen hydrogel; (A2, B2, C2, D2) results of image restoration using the Iterative Deconvolution 3D plugin for ImageJ; (A3, B3, C3, D3) results of image restoration using the Deconvolution Lab plugin for ImageJ; (A4, B4, C4, D4) results of image restoration using the HuygensPro software; (A5, B5, C5, D5) results of image restoration using the CUDA Deconvolution plugin for ImageJ. Yellow line marks the region of interest for the intensity profile measurement. (A6, B6, C6, D6) Intensity profiles along a line placed at the same position in all single slice images (see yellow lines in A1-D1). (A6) P(MMA-co-MABP-co-RhBMA) coated paper; (B6) Collagen hydrogel; (C6) U2OS cell on planar surface and (D6) U2OS cell in collagen hydrogel.

At a first glance, visual inspection of the results produced by the Deconvolution Lab plugin show similar findings like the inspection of the images deconvolved with CUDA. The intensity profiles show that the local intensity maxima are of the same magnitude as in the unprocessed images. However, images restored with Deconvolution Lab show a very good improvement of contrast which is particularly noticeable in the maximal intensity Z-projections of the U2OS cells cultivated in a Hydrogel (Figure 7 D3).

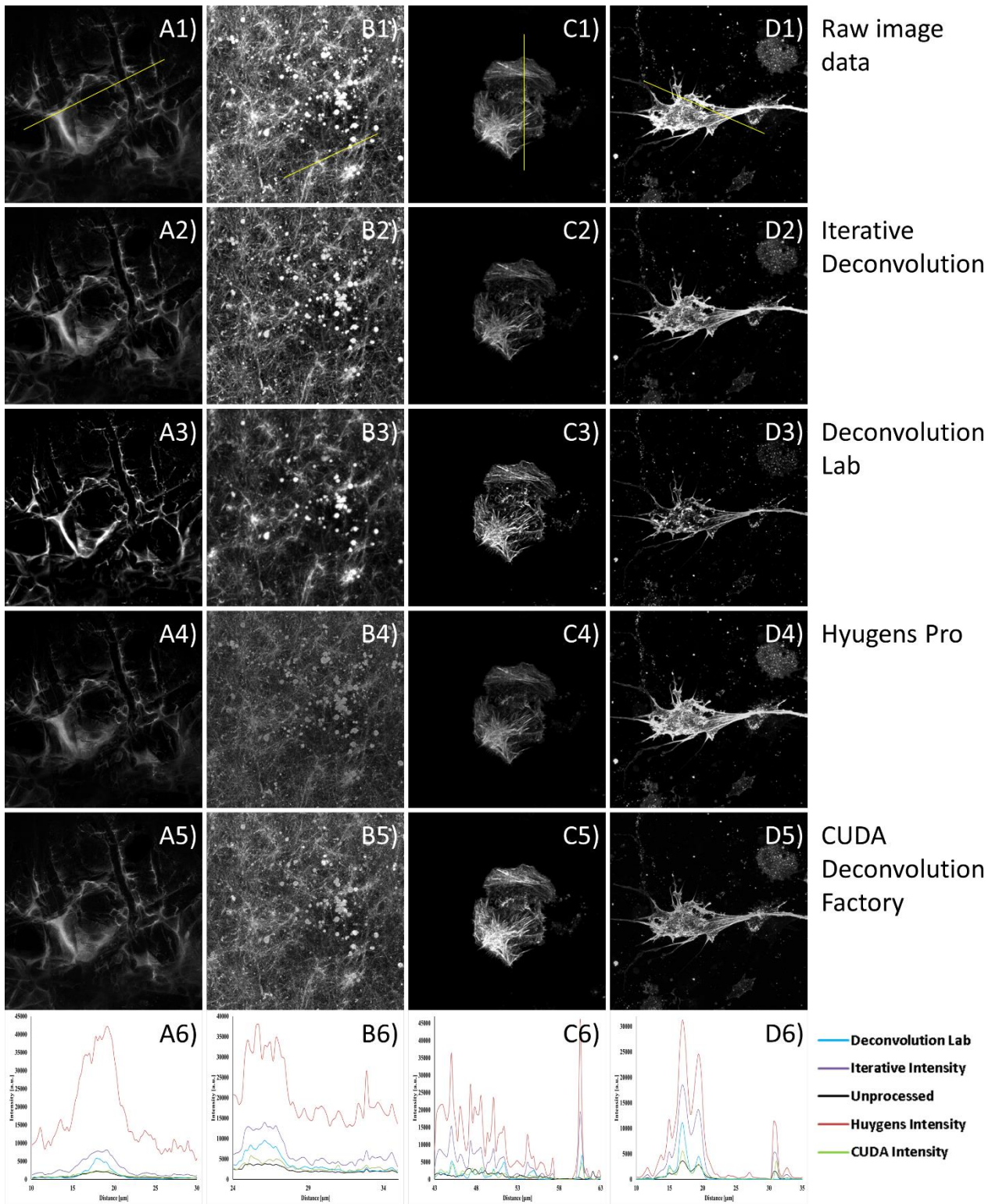


Figure 7: Maximal intensity Z-projection images of P(MMA-co-MABP-co-RhBMA) coated paper

(A) Raw image; (B) Raw image of a collagen hydrogel with a concentration of 2 mg ml⁻¹; (C) Raw image of a U2OS cell transfected with LifeAct-RFP cultivated on a planar surface; (D) Raw image of a U2OS cell transfected with LifeAct-RFP cultivated in a collagen hydrogel; (A2, B2, C2, D2) results of image restoration using the Iterative Deconvolution 3D plugin for ImageJ; (A3, B3, C3, D3) results of image restoration using the Deconvolution Lab plugin for ImageJ; (A4, B4, C4, D4) results of image restoration using the HuygensPro software; (A5, B5, C5, D5) results of image restoration using the CUDA Deconvolution plugin for ImageJ. Yellow line marks the region of interest for the intensity profile measurement. (A6, B6, C6, D6) Intensity profiles along a line placed at the same position in all maximal intensity Z-projection images (see yellow lines in A1-D1). (A6) P(MMA-co-MABP-co-RhBMA) coated paper; (B6) Collagen hydrogel; (C6) U2OS cell on planar surface and (D6) U2OS cell in collagen hydrogel.

Both the Iterative Deconvolution 3D plugin for ImageJ and the HuygensPro software increase the value of intensity maxima greatly while at the same time suppressing the background noise level or at least keeping it at the same level of the unprocessed images. This greatly improves the Signal to Noise ratio and thus increases overall image quality. This is true in all cases and is most obvious in case of the P(MMA-co-MABP-co-RhBMA) coated paper and the U2OS cell cultivated in a collagen hydrogel. Intensity profiles for the single slice image (Figure 6 A6 and D6) and the maximal intensity Z-projection (Figure 7 A6 and D6) of both objects show how the intensity spikes of the respective object is considerably increased whereas the noise level almost remains unchanged compared to the unprocessed images. The HuygensPro software increases the intensity values slightly more than the Iterative Deconvolution 3D ImageJ plugin.

3.1.2. Comparison of temporal performance

In terms of image restoration HuygensPro and the Iterative Deconvolution 3D plugin achieve a comparable quality, however, HuygensPro is considerably faster than the Iterative Deconvolution plugin. Whereas the Iterative Deconvolution plugin deconvolved the image stacks in 20 min (U2OS cell cultivated on a planar surface) to 30 min (collagen hydrogel), HuygensPro only took 135 s (U2OS cell cultivated on planar surface) to 221 s (U2OS cell cultivated in a collagen hydrogel). Table 4 summarizes the time it took for all four deconvolution

applications to restore all four test image stacks over 10 iterations. The GPU driven CUDA deconvolution plugin is considerably faster than all other deconvolution applications as long as the memory of the graphics card is sufficient. Using the NVIDIA GeForce GT610 for deconvolution resulted in the memory of the CPU auxiliary supporting the GPU and thus becoming the time limiting factor in the restoration process. Therefore, all images shown are restored using the NVIDIA GeForce GTX580 graphics card. Like previously stated the Iterative Deconvolution 3D plugin achieved results comparable with the results of the commercially distributed HuygensPro software. Taking into account that the Iterative Deconvolution 3D plugin is a freely accessible plugin for ImageJ which (at least for the four objects tested) restores images with comparable results to a professional deconvolution software, the by far slowest performance can be accepted and tolerated, as long as this deconvolution application is not part of an image acquisition and processing system in which it would act as an extremely speed limiting factor.

3.1.3. More detailed view at the GPU based CUDA deconvolution factory

It needs to be said, that all deconvolution processes were manually stopped after 10 Iterations. It is possible, that more iterative steps might have an impact on the findings presented. In order to access this question CUDA deconvolution factory was allowed to perform deconvolution for roughly the same lapse of time as Deconvolution Lab, resulting in 2500 rounds of iterations for all for image stacks, using the NVIDIA GeForce GTX580 graphics card. Additionally the CUDA Deconvolution factory plugin offers the possibility to automatically stop deconvolution when an optimal deconvolution result is achieved. The inherent stop criterion for this is based on a standard Richardson-Lucy maximum likelihood algorithm (Richardson 1972; Bruce and Butte 2013). Table 3 summarizes the time

it took for the 2500 rounds of iterations as well as the optimal numbers of iterations and the respective time.

Table 3: Time performance of CUDA Deconvolution factory

Object	Time for 2500 rounds of iteration	Rounds of iterations before automatic termination	Lapsed time before automatic termination
U2OS 2D	52 s	24	1.2 s
U2OS 3D	118 s	18	2.4 s
Collagen	103 s	34	2.7
PMMA Paper	108 s	34	2.1

Figure 8 shows the achieved results in form of single slice images and the maximal intensity Z-projections. If the CUDA Deconvolution Factory application is allowed to process the images until the inherent criterion for termination is reached, image restoration is indeed improved (Figure 8 E1-E4 and F1-F4) compared to the results achieved with 10 iterations (Figure 8. C1-C4 and D1-D4). However, the overall quality is still inferior compared to the restoration achieved with HuygensPro, Deconvolution Lab and Iterative Deconvolution Lab 3D. CUDA Deconvolution Factory fails to remove background noise pixels, which are readily removed by the other mentioned applications. This is especially apparent for the collagen hydrogel image stack, but is also observable for the P(MMA-co-MABP-co-RhBMA) coated paper and the U2OS cultivated in collagen image stacks.

Forcing the CUDA Deconvolution Factory application to perform 2500 iteration introduces artifacts to the images such as high frequency noise (Figure 8 A2), a fragmentation of features (Figure 8 A3) and a flickering in intensity values from one slide to the next (Figure 8 G1-G4). Hence, it is clearly advisable to not overdo the amount of iterations performed on any given image stack.

Without access to the commercially available HuygensPro software, the decision between the other three freely distributed ImageJ Plugins depends on a few aspects that need to be weight against each other. Considering, that the Deconvolution Lab plugin is distinctly faster than Iterative Deconvolution 3D plugin, but without delivering the same improvements to the overall image quality, it is a from case

to case decision if one prefers a fast deconvolution with slightly worse results or if the time investment is worth the improved image restoration. CUDA Deconvolution Factory at the time being is restricted to systems equipped with a NVIDIA graphics card and can be a good substitution for CPU based deconvolution software providing that the memory of the GPU is large enough to process the image data without auxiliary accessing the CPU. The two graphic cards available for this test study had either 1 GB of DDR3 memory (NVIDIA GeForce GT 610) or 1.5 GB GDDR5 memory (NVIDIA GeForce GTX580) available. The superior memory in terms of quantity and quality of the GTX580 graphics card coupled with the larger number of CUDA cores (512 cores for the GTX580 vs 48 cores for the GT610), results in the much faster deconvolution, being at least 100 times faster than Deconvolution Lab and even 1000 times faster than the Iterative Deconvolution 3D plugin (see Table 4).

Table 4: Time it took the different applications to deconvolve four different test image stacks

Object	Iterative Deconvolution 3D	Deconvolution Lab	HuygensPro	CUDA (GTX580)	CUDA (GT610)
U2OS 2D	1200 s	59 s	135 s	0.7 s	7 s
U2OS 3D	1500 s	149 s	221 s	1.5 s	135 s
Collagen	1800 s	124 s	187 s	1.7 s	69 s
PMMA Paper	1500 s	121 s	114 s	1.37 s	39 s

3.1.4. Isosurface rendering to show and compare the beneficial effect of deconvolution

Image restoration using deconvolution has more purpose than just improving image quality. By improving the signal to noise ratio *via* reduction of background noise and enhancement of intensity maxima subsequent image processing and analysis steps deliver better results. For example, colocalization studies can profit from deconvolution as shown by Landmann (Landmann 2002).

In the comparison presented here, isosurface rendering of the image stacks to achieve three dimensional representations of the objects was applied to compare

the deconvolved stacks among themselves and with the unprocessed, raw image stack. Since isosurface render images are generated based on an intensity threshold it is advisable to compare image stacks with similar intensity values. Therefore, the unprocessed image stack is compared with the restored image stacks achieved with the Deconvolution Lab and CUDA Deconvolution factory plugin, both after 10 iterations (Figure 9). Comparisons are shown for the U2OS cell grown on a planar surface and the P(MMA-co-MABP-co-RhBMA) coated paper. As already stated above, the CUDA Deconvolution Factory plugin does not improve the signal to noise ratio significantly which shows in the nearly identical surface render images (compare Figure 9 A) to B) and D) to E)) whereas the surface render images based on the image stacks achieved with the Deconvolution Lab plugin show vast improvements (Figure 9 C) and F)).

The results of this study are comparable to a similar evaluation of deconvolution applications published in 2010 (Griffa et al. 2010), which also assessed HuygensPro, Deconvolution Lab and Iterative Deconvolution 3D. However, the mentioned study did not include the CUDA Deconvolution Factory and furthermore failed to deconvolve actual, recorded image data with the Iterative Deconvolution 3D plugin due to memory restrictions. Apart from this discrepancy, the results are in good agreement with the results of the evaluation presented here.

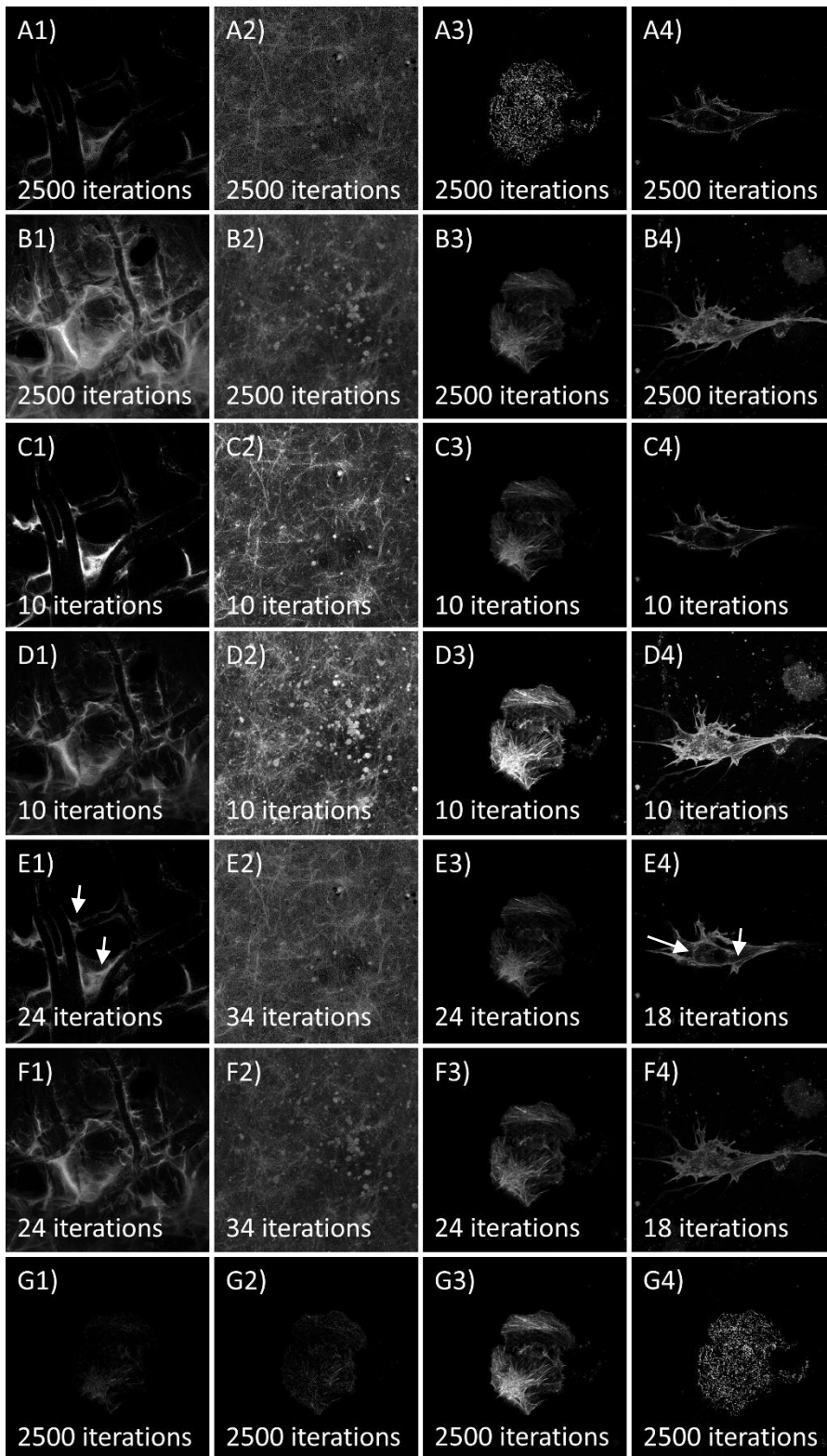


Figure 8: Restored images with CUDA Deconvolution Factory running for 2500 iterations or an application determined number of iterations

(A1-A4) Single slice images after 2500 iterations; (B1-B4) Maximal intensity Z-projection images after 2500 iterations; (C1-C4) Single Slice images after 10 iterations. (D1-D4) Maximal intensity Z-projection images after 10 iterations. (E1-E4) Single Slice images after automatic termination of the deconvolution process. (F1-F4) Maximal intensity Z-projection images after automatic termination of the deconvolution process (G1-G4) Sequence of four single slice images (after 2500 iterations) of the U2OS cell cultivated on a planar surface.

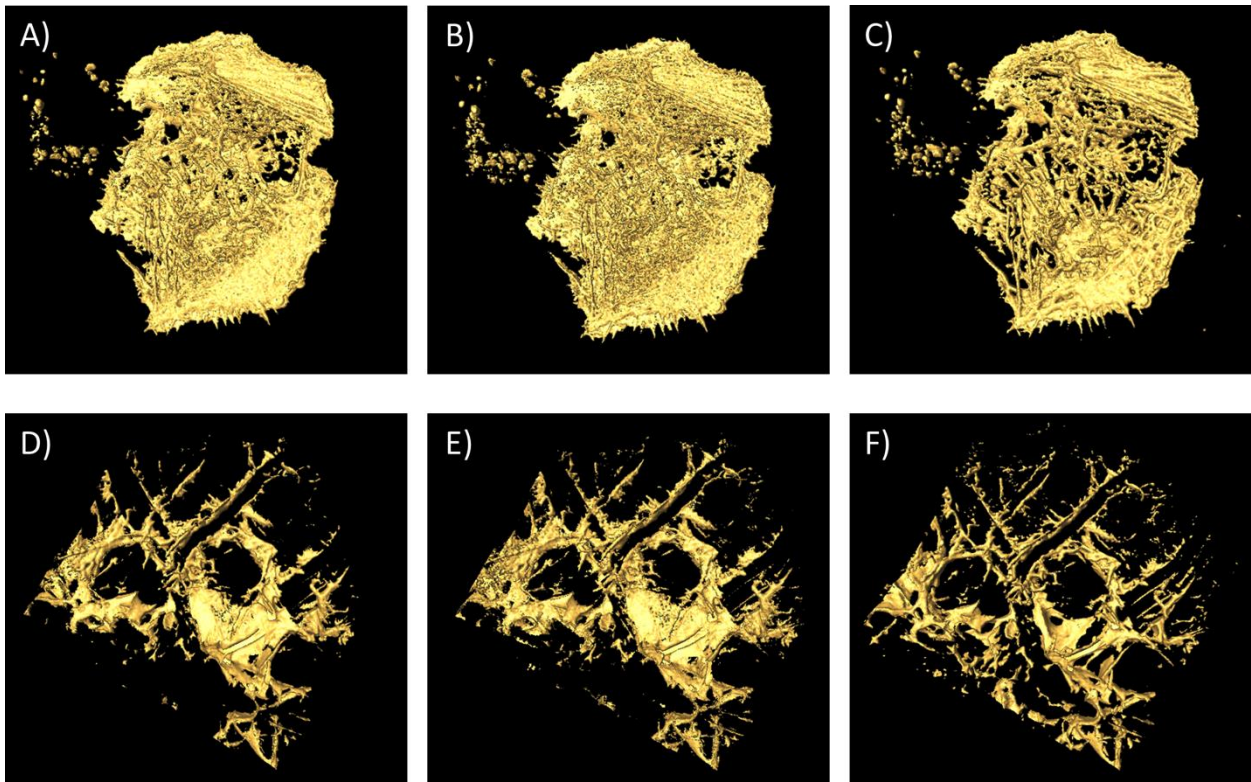


Figure 9: Isosurface Render Images generated with the same intensity threshold value (A-C) U2OS cell cultivated on a planar surface: (A) unprocessed image stack; (B) CUDA Deconvolution Factory and (C) Deconvolution Lab. (D-F) P(MMA-co-MABP-co-RhBMA) coated paper: (A) unprocessed image stack; (B) CUDA Deconvolution Factory and (C) Deconvolution Lab.

3.2. Difference between 2D and 3D cell culture: Using cellular distribution, actin morphology and membrane dynamics as read-out parameters

Cell culture is conventionally done in a two dimensional fashion. However, this means that results and insights gained by experiments and studies on such an artificial system are not representative of *in vivo* conditions found inside an organism or a tissue. Therefore, the development of three dimensional culture systems which are more closely related to the *in vivo* conditions is of great importance. Three dimensional systems however pose a completely new challenge, since they need to be evaluated and characterized in order to assess their usefulness for three dimensional cell culture systems. Hence, it is advisable to use

systems that are simplistic and easily adjustable. Here, a composite system based on paper and collagen hydrogel is used to prevent durotaxis, a common phenomenon in three dimensional cell culture. The term durotaxis is used to describe cellular migration as response to stiffness. This migration can be of biological relevance or completely unwanted. Therefore, systems where a three dimensional cell culture systems is in close proximity to a surface with a high stiffness (i.e. collagen hydrogel directly applied to a glass coverslip) exert a signal on the cells which is, in most cases, not requested. By using paper filled with collagen, the close proximity to glass is circumvented, since the composite material is floating in medium, thus guaranteeing isotropic stiffness conditions. Additionally, the formation of the actin cytoskeleton and the membrane mobility were examined in more detail as exemplary parameters to determine how a two dimensional cell culture system differs from a three dimensional system

3.2.1. Durotaxis – Migration towards the glass surface

For a detailed investigation of the migration behavior the optical sectioning capability of a confocal laser scanning microscope was applied. OVMZ-6 cells stained with the plasma membrane label DiO (see chapter 3.3.6.) were cultivated in surface attached collagen hydrogels (2 mg mL^{-1}) (see chapter 3.3.2 for detailed information on collagen hydrogel preparation). Distribution of cells inside a collagen hydrogel was observed over a period of 8 d *via* confocal laser scanning microscopy, followed by analysis as described in chapter 3.3.9. Fluorescence signals are emitted by the cells, thus, the information about the total number of signal pixels is in correlation to the total amount of cells.

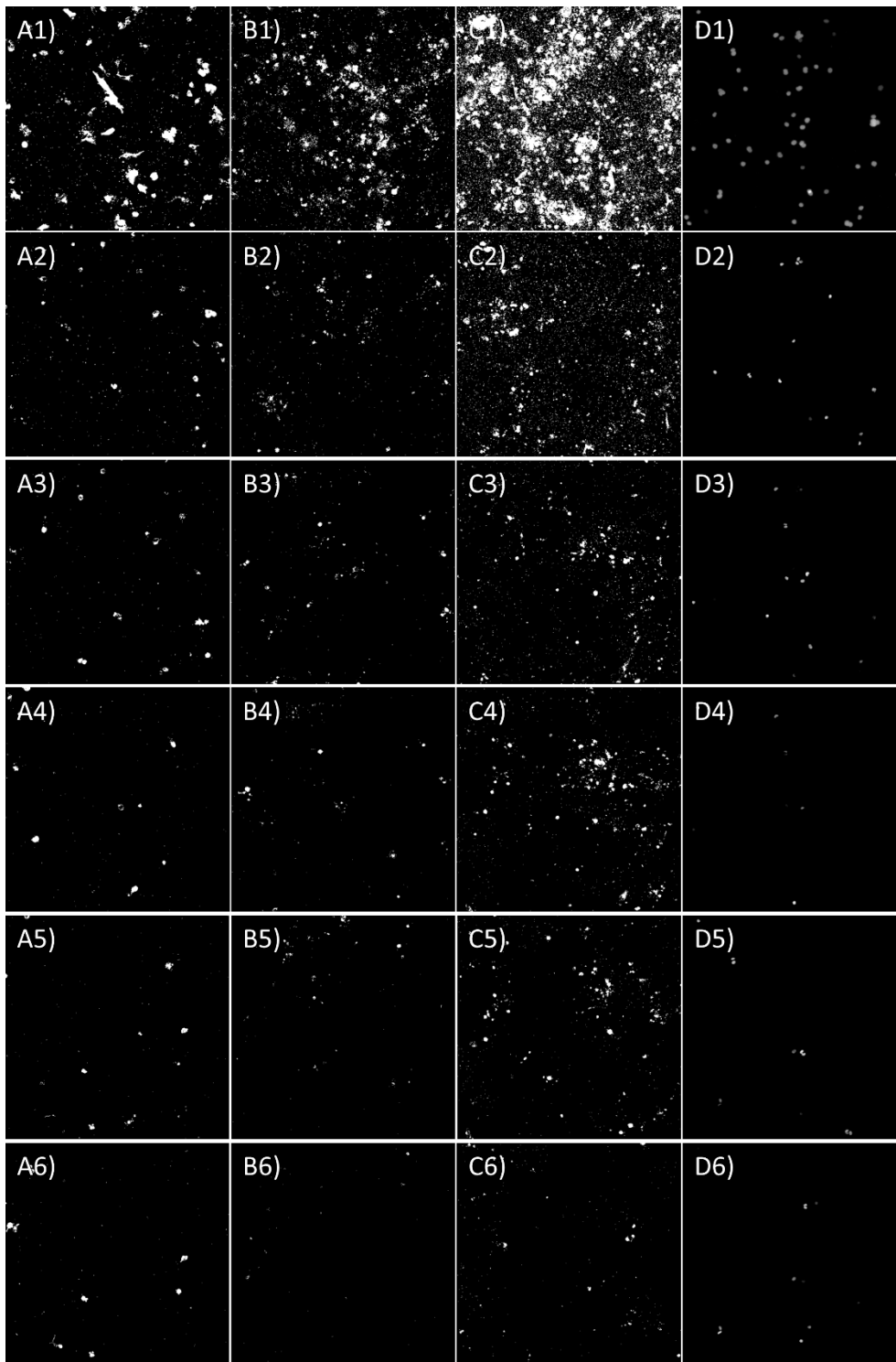


Figure 10: Distribution of OVMZ-6 cells inside a collagen hydrogel on a glass surface

A1-A6) Sum slice Z-projections of OVMZ-6 cell distribution in a collagen hydrogel after 24 h; B1-B6) after 120 h; C1-C6) after 192 h and D1-D6) after 4 h. A1-D1) Sum slice Z-projection of a complete 210 μm thick image stack; A2-D2) Sum slice Z-projection of the first 30 μm close to the glass coverslip surface; A3-C3; A4-C4; A5-C5 and A6-C6) Sum slice Z-projections of the respectively following 30 μm thick sub-stack. Scale bar is 100 μm.

Results as depicted in Figure 10 and Figure 11 show the shifting distribution of OVMZ-6 cells over the course of 192 h. Four hours after collagen culture preparation cells were evenly distributed over the entire 210 μm thickness of the collagen gel, containing 26 % of the cells in the first 30 μm sub-stack and 18 % of the cells in the 180 – 120 sub-stack. This distribution was already greatly altered after 24 h of cultivating OVMZ-6 cells in a collagen hydrogel, when most of the cells are found within the first 30 μm sub-stack, with 70 % of the cells present in this sub-stack. The remaining 30 % of the cells are evenly distributed over the next 180 μm , with 3 to 7 % per 30 μm thick sub-stack. After five days of cultivation, the relative distributions changes only slightly, with an increase to nearly 80 % of cells found within the first 30 μm . Consequently, the relative amount of cells found in the sub-stacks from deeper inside the collagen hydrogel decreases even more in stacks past a depth of 90 μm in relation to the distribution observed after 24 h. However, at a depth of 30 to 60 μm , a slight increase of relative amount of cells is observed, showing 9 % of cells after 120 h in this depth compared to 7 % at 24 h. After eight days of cultivation the 1 - 30 μm sub-stack still contained 80 % of the cells detected in the image stack. 9 % of the remaining cells are found within the 30 – 60 μm sub-stack, resulting in 10 % of cells evenly distributed over the remaining 150 μm , with 3 – 4 % of pixels per 30 μm sub-stack. Interestingly, the last two sub-stacks (from 150 to 180 μm and from 180 to 210 μm) contain nearly no pixels at all, indicating an abandonment of these parts of the collagen hydrogel which are most distanced from the glass coverslip. Since optical penetration depth is not a problem for this type of specimen as is clearly demonstrated by the fact, that cells are easily detectable in the upper regions of the collagen gels 4 h after preparation, the distinct lack of cells in these regions after 24 h are a clear sign of abandonment due to migration, most likely as response to the difference in stiffness between glass surface and collagen hydrogel.

Orthogonal views as shown in Figure 12 of the image stack recorded after 24 h confirms the accumulation of OVMZ-6 cells near to the glass coverslip surface as

shown by the close proximity of the fluorescence signal from the DiO to the reflected light signal from the glass coverslip.

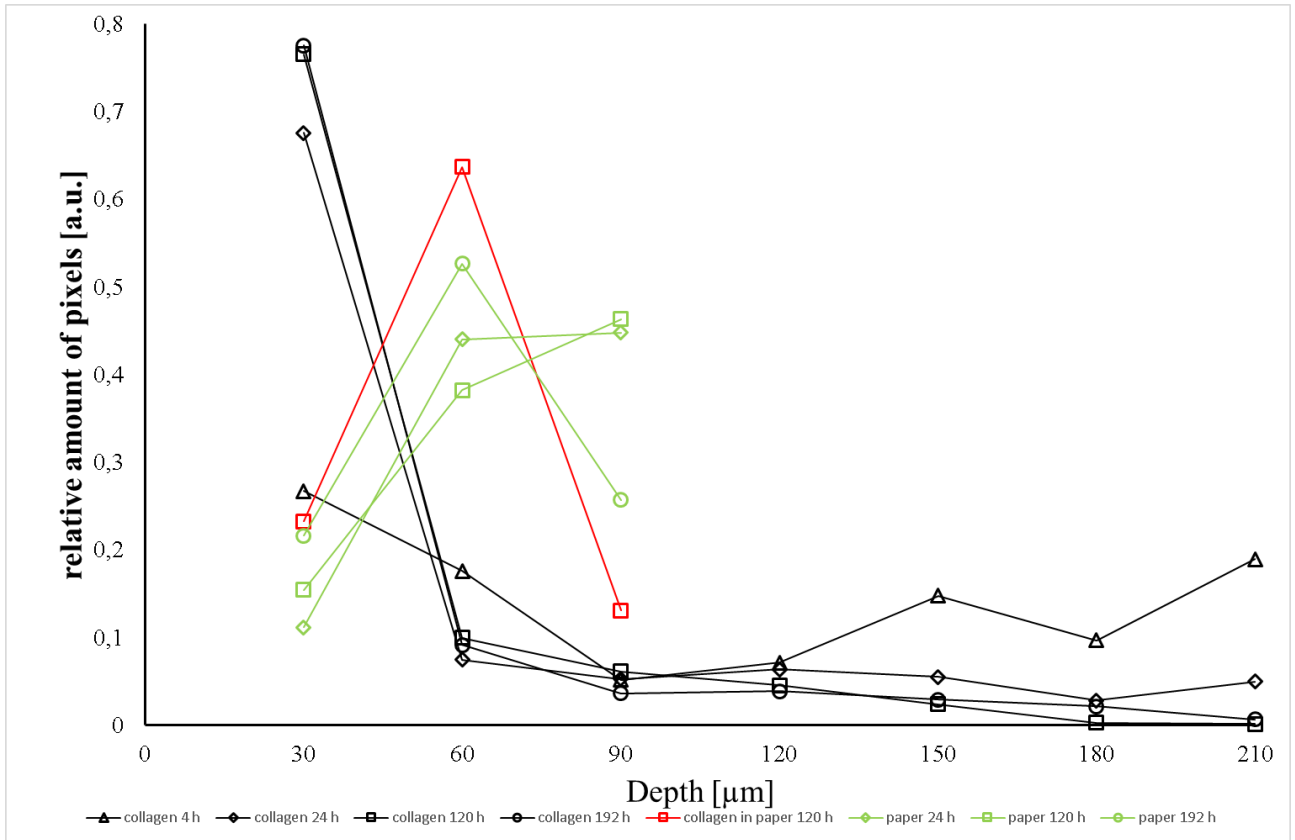


Figure 11: Distribution of OVMZ-6 cells measured by pixel amount distribution

Allocation of cell distribution in 30 μm thick sub-stacks of an image stack with a total thickness of 210 μm for unsupported collagen hydrogels and 100 μm for supported collagen hydrogels in paper. Black symbols show the distribution of cells inside unsupported collagen hydrogels. Red symbols show the distribution of cells inside collagen hydrogels in paper. Green symbols show the distribution of cells inside paper.

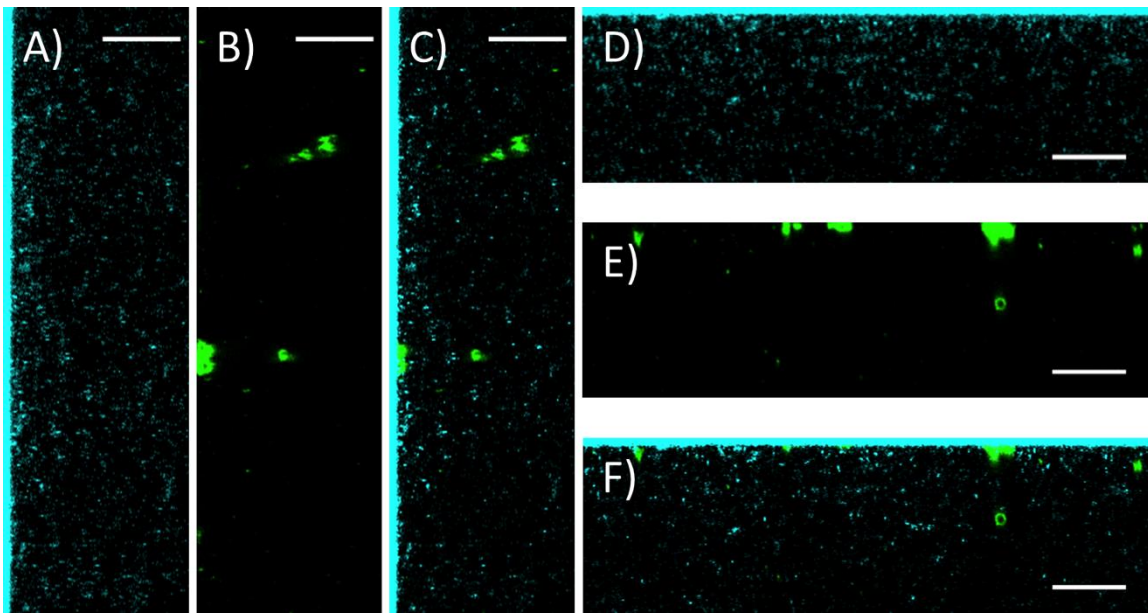


Figure 12: Orthogonal Views of OVMZ-6 cells in collagen hydrogel after 24 h
 (A) Reflection image of the collagen hydrogel in YZ direction and (D) reflection image of the collagen hydrogel in XZ Direction. The thick blue part of the images is the reflection of the underlying glass coverslip. (B) and (E) show the position of cells in the collagen hydrogel. (C) and (F) show the overlay of (A) and (B), respectively (D) and (E). Scale bar is 100 μm .

Results and observations so far show, that the close proximity to the glass coverslip surface influence the distribution of cells inside a collagen hydrogel by positioning the majority of the cells near the surface. Therefore, a need for a culture system that circumvents the contact between collagen network and glass coverslip surface is necessary. However, microscopic probing of such a system still needs to be feasible, which in consequence means, the collagen hydrogel – at least temporarily - needs to be placed on a glass coverslip.

Lab-produced paper offers the possibility to contain collagen hydrogel within a well-defined system, which is (i) easily manipulable, (ii) can be relocated and (iii) offers reasonable optical properties within the geometric sizes used. Therefore collagen hydrogels containing cells were cultivated inside lab-produced paper sheets, circumventing the need of fixating the collagen hydrogels on top of a glass surface and instead keeping the cell culture free floating in the culture medium, resulting in isotropic stiffness conditions where the collagen hydrogel and in turn the cells are exposed to the same stiffness from all directions. Figure 11 reveals

that incorporation of the cell containing collagen hydrogel into paper indeed has an effect on the distribution of the OVMZ-6 cells. Distribution of cells is clearly shifted towards the central part of the collagen hydrogel in paper system, containing 65 % of the pixels detected in a depth of 30 to 60 μm , 22 % in a depth of 0 to 30 μm and 13 % in a depth of 60 to 90 μm after 5 days of cultivation.

In a next step cells were also cultivated in lab-produced paper without collagen hydrogel to investigate the effects this material has on the cells. HeLa cells stably expressing GFP in the nucleus were cultivated for 10 days in linters lab-produced paper. With the already established method of analysis, distribution of cells within the paper was investigated. Cultivating cells inside paper without the addition of collagen, results in a comparable distribution of cells as in the case of incorporating a collagen hydrogel into paper. Cell distribution is distinctly shifted towards the central region of the paper, containing 44 % of the cells after 24 h and 52 % of cells after 192 h. As shown in Figure 13, HeLa cells when cultivated in paper form spheroid like structures that span over the entire thickness of the paper (100 μm).

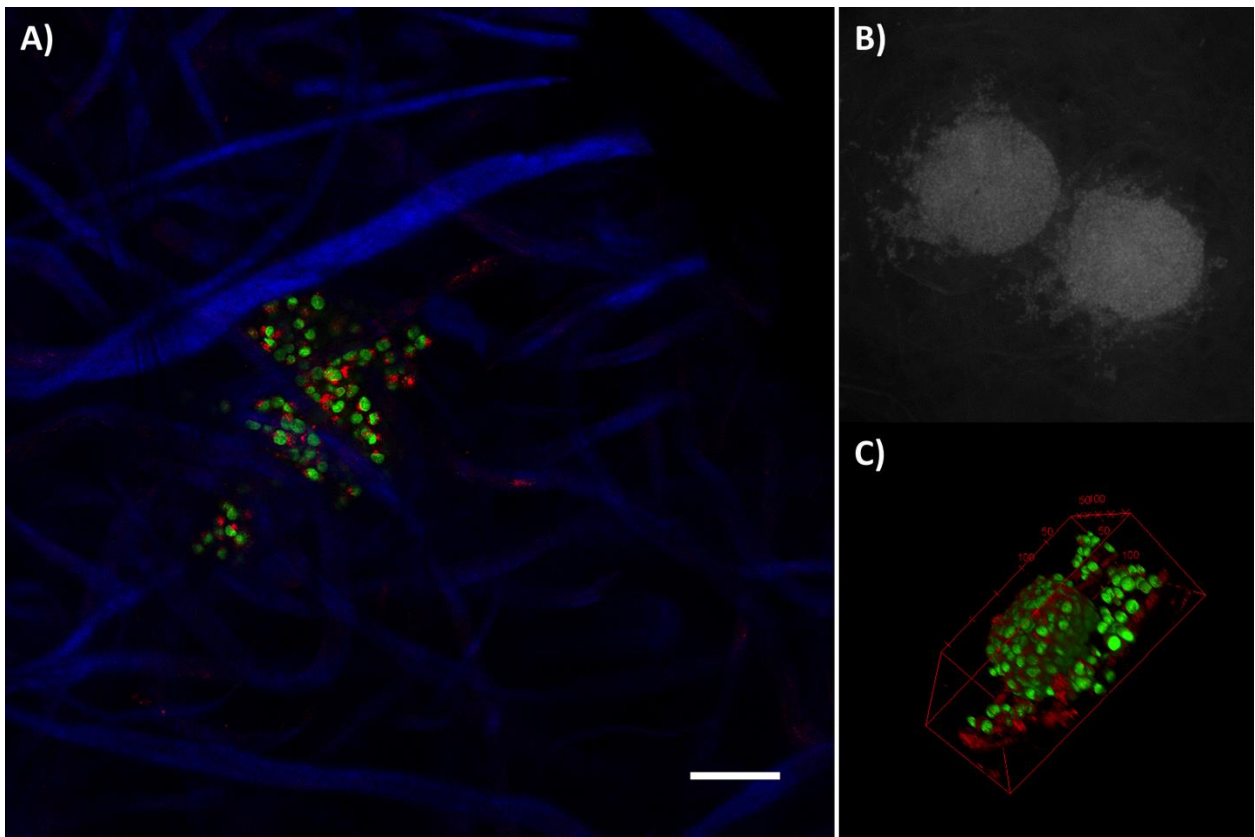


Figure 13: Spheroid like structures formed in paper by HeLa cells

(A) Maximal intensity Z-projection of a confocal image stack, showing the cellulose fibers stained with calcofluor white (blue), cell nuclei labeled with GFP (green) and a plasma membrane staining with DiD (red). (B) Widefield fluorescence image of two spheroid like structures in close proximity inside paper. (C) 3D representations of a spheroid like structure spanning the complete depth of the paper (100 μm). Scale bar is 100 μm .

The image processing steps chosen in the analysis method presented in this chapter is beneficial in approaching the depth dependent intensity loss observed with image acquisition using confocal laser scanning microscopy. With increasing scan depth, laser excitation intensity and in turn emission intensity deteriorate. Any subsequent image processing needs to adopt to this and either implement an intensity compensation step post imaging or a smart adjustment of detector sensitivity during imaging. However, the approach used in this chapter circumvents this problem by setting the intensity of all pixels to either a value of 1 (signal pixel) or 0 (background pixel). By dividing the acquired image stacks into sub-stacks with individual threshold setting and finally generation of sum slice Z-projection images with signal and background pixels, counting of signal

pixels is an appropriate measurement for the distribution of cells. Since every pixel in each slice is set to have a value of 1, summing up all pixels gives information about the total number of signal pixels in a stack. This approach is a simple, quick, and robust alternative to more elaborate image segmentation approaches for counting cells. As the fidelity of segmenting approaches clearly decreases with lower signal to noise ratio, cells imaged deep inside the gel would increasingly fail to be detected reliably. The binary method, in turn, is virtually free from this effect, as it concentrates on presence, rather than quality of signal. Fluorescence signals are emitted by the cells, thus, the information about the total number of signal pixels is in correlation to the total amount of cells. The approach chosen in this chapter ignores variation in cell size and fluorescence intensity.

3.2.2. A view at the actin cytoskeleton

To further characterize the effect of the culture condition stiffness, the actin cytoskeleton was investigated and compared between (i) cells cultivated directly on top of a glass coverslip without the presence of collagen, (ii) cells cultivated in a collagen hydrogel which have migrated towards the top of a glass coverslip and (iii) cells cultivated in a collagen hydrogel and still surrounded by a collagen hydrogel. Figure 14 shows, that the organization of the actin cytoskeleton shows a high degree of similarity when comparing cells cultivated under conventional two dimensional conditions and cells which have migrated towards the glass coverslip surface despite being cultivated in a collagen hydrogel.

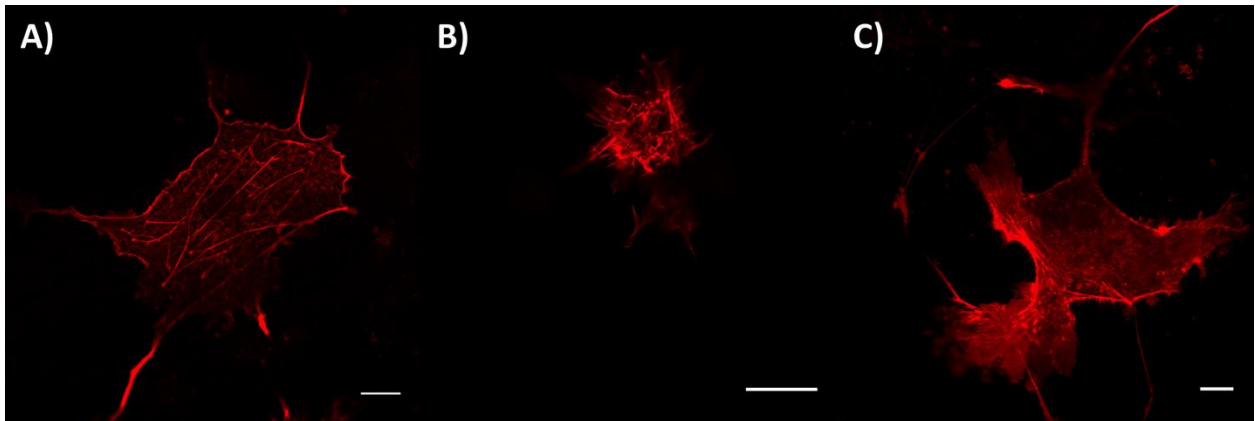


Figure 14: Comparison of the actin cytoskeleton between OVMZ-6 cells under different cell culture conditions

(A) Conventional two dimensional cell culture on top of a glass coverslip; (B) Cultivated in a collagen hydrogel and still completely embedded in collagen; (C) Cultivated in a collagen hydrogel but migrated towards the glass coverslip surface. Labeling of actin was performed by transiently expressing the fusion protein LifeAct-RFP. Scale bar in every image is 20 μm .

In both cases, prominent actin stress fibers are visible, especially alongside the outer borders of the cell body (compare Figure 14 A) and C)). However, stress fibers are not so distinct in cells still completely surrounded by collagen hydrogel. Furthermore, a continuous stretch of cortical actin is not visible and therefore does not seem to be required support the cell body under these conditions. Instead, actin is labeled rather diffusely and unordered. It is however noteworthy, that even though cells cultivated directly on glass coverslips and cells which have migrated towards the surface show a high degree of similarity regarding the organization of the actin cytoskeleton, cells which have migrated also show some features in terms of overall shape, that are related to cells which are completely embedded in collagen. Namely the withdrawal from a completely flattened cell body and loss of actin stress fibers in some regions of the cell body, establish a comparability between cells which have migrated through a collagen hydrogel towards the glass surface and cells completely embedded in collagen (compare Figure 14 B) and C)). Figure 15 shows the same cells as in Figure 14 (Figure 15 A-F) corresponds to Figure 14 B) and Figure 15 G-M) corresponds to Figure 14 C)) in orthogonal views to further emphasize the effect the difference in microhabitat has on the actin cytoskeleton.

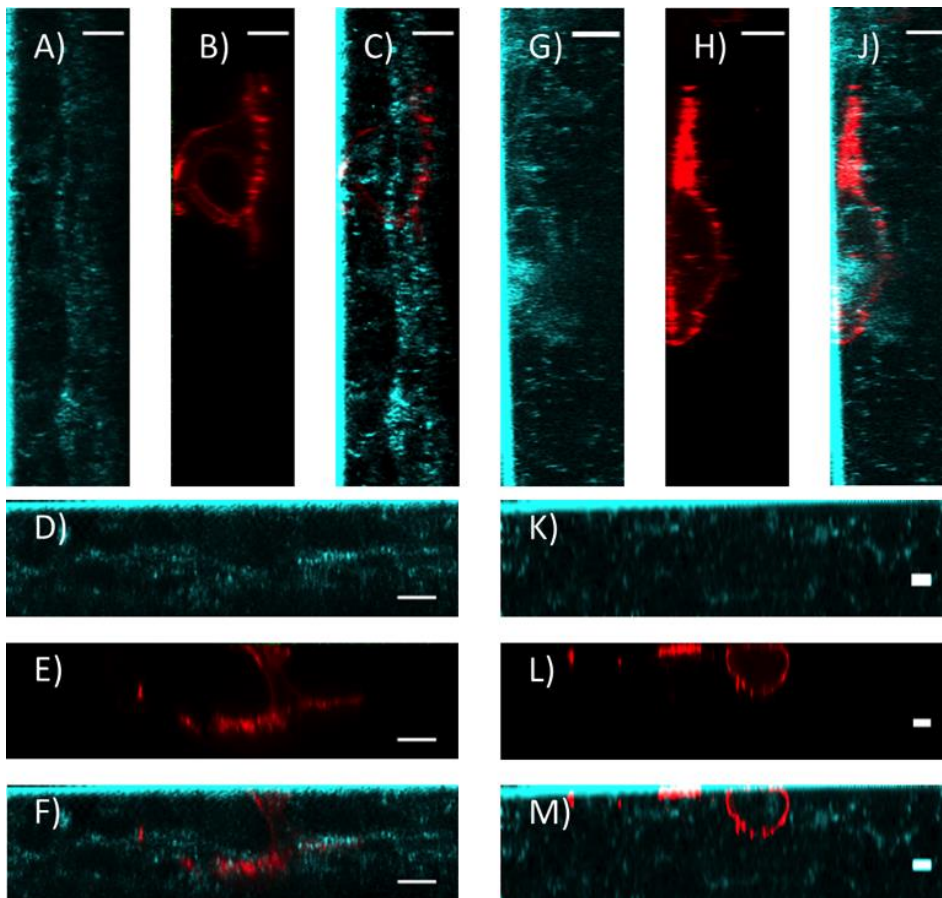


Figure 15: Comparison of the cell positioning and the effect on the actin cytoskeleton in different surroundings

(A-F) OVMZ-6 cells cultivated in a collagen hydrogel and still completely surrounded by collagen. (G-M) Cultivated in a collagen hydrogel but migrated towards the glass coverslip surface. Labeling of actin was performed by transiently expressing the fusion protein LifeAct-RFP. Scale bar in every image is 10 μm .

Even though the main part of the cell body in Figure 15 B-C) and Figure 15 E-F) is measurably distanced from the glass coverslips surface, some contacts are already formed between the cell and the surface. In this cellular protrusions the actin cytoskeleton formation is distinctly different from the one shown in the rest of the cell body. Here, the actin cytoskeleton labeling is rather diffuse and unorganized whereas in the protrusions, the labeling shows clearly visible cortical actin localization. This is also true for the cell body in Figure 15 L-M). Here, the complete cell body is in direct contact to the surface of the class coverslip, resulting in an actin cytoskeleton formation outlining the cells shape.

3.2.3. Fluorescence Recovery after Photobleaching

Fluorescence recovery after photo bleaching was compared for two different cell culture systems – namely cultivation of OVMZ-6 cells on two dimensional glass coverslip surfaces and in three dimensional collagen hydrogels – under otherwise identical conditions in regards to FRAP setup parameters and identity of the molecule under investigation.

A qualitative comparison (as shown in Figure 16) of the two and three dimensional culture conditions reveals a significantly faster half time of recovery in the three-dimensional cell culture systems, with fluorescence intensity reaching 50 % of the pre-bleach value after 10 s, whereas the halftime recovery for the two dimensional cell culture was reached after 27 s. However, the mobile fraction is the nearly identical in both cases: 88 % of the initial, pre-bleach fluorescence intensity is recovered in the three dimensional cell culture system, compared to 83 % recovery under two dimensional cell culture conditions.

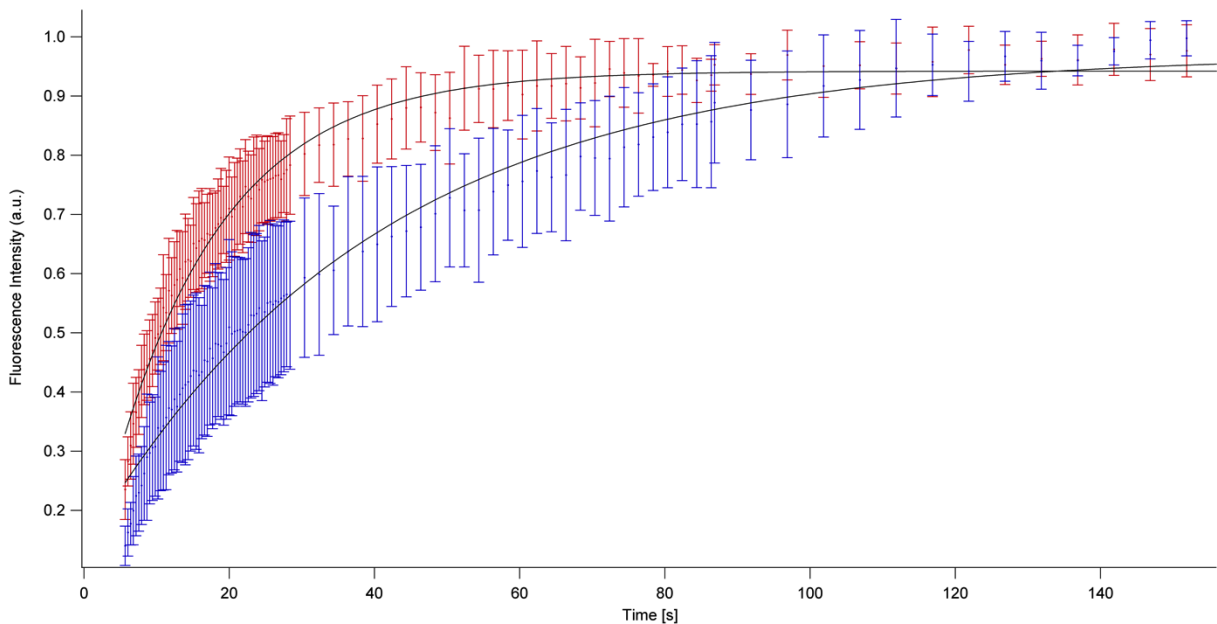


Figure 16: FRAP curves of CAAX-mCherry

Red: FRAP curve in 3D (n=9); Exponential Recovery Fit gives a halftime recovery value of 10.63 s and a mobile fraction of 0.88. Blue: FRAP curve in 2D (n=8); Exponential Recovery Fit gives a halftime recovery value of 27.41 s and a mobile fraction of 0.83.

3.3. Microscopic analysis of modified paper

Optical microscopy has long been recognized as a method to characterize the heterogeneous and complex structure of paper. With fluorescence detection, the functionality has even been extended to provide chemical selectivity, e.g. to determine the distribution of secondary modifications like coatings and fillers throughout a sheet of paper. The full spectrum of capabilities offered by fluorescence microscopy, which is able to deliver information with high spatial, spectral, radiometric, and temporal resolution simultaneously and non-destructively, however has yet to be exploited. With paper more and more coming into focus as a versatile platform for the development of functional devices, static structural and compositional information is no longer sufficient to describe the properties of these systems. Rather, a likewise versatile method is required that delivers spatially resolved, quantitative, sensitive, and, most importantly, also dynamic measurements.

Quantitative widefield and confocal fluorescence microscopy are able to meet this set of demands. In a proof of concept analysis on PMMA-modified microfluidic paper substrates, all four types of resolution provided by fluorescence microscopy are exploited, by analyzing the distribution of rhodamine labeled polymer in relation to calcofluor white labeled cellulose fibers with high selectivity and spatial resolution and by imaging the static and dynamic distribution of a FITC labeled dextran solution inside the polymer coated fiber network. The advantages of fluorescent microscopy and differences between widefield epifluorescence and confocal laser scanning microscopy are demonstrated on polymer-modified paper. In particular, the spatial and temporal relationship of three key components, as found for a paper-based microfluidic system, are investigated: (i) the cellulose fibers, (ii) a hydrophobic polymer, which is surface-attached to the fibers in a spatially defined way to form a barrier for aqueous liquids, and (iii) the aqueous phase, i.e. the fluid itself.

3.3.1. Cellulose staining with Calcofluor White

Calcofluor white is known for its ability to stain cellulose and chitin fibers (Herth and Schnepf 1980; Haigler et al. 1980). Here, this property is exploited to counterbalance the detrimental imaging effect of the highly scattering nature of paper samples. Enhancing the fluorescence intensity of the cellulose fibers in the same wavelength range as the autofluorescence of cellulose is beneficial for imaging and results in high quality image of the cellulose network as shown in Figure 17.



Figure 17: Maximal intensity Z-projection of a cellulose network stained with calcofluor white

The Z-projection is based on an image stack with a voxel size of 0.76 x 0.76 x 0.5 μm . Image size is 1024 x 1024 pixels. Blind deconvolution using the CUDA deconvolution plugin was applied for 27 iterations.

Staining with calcofluor white greatly improves the visibility of the thick cellulose fibers. Smaller, finer cellulose branches are also visible. Most impressive however is the fact that a calcofluor white stained image stack conveys the three-dimensionality of the cellulose network in this rather thin paper sample which is otherwise hard to capture *via* microscopic analysis.

3.3.1. Polymer concentration and brightness are correlated

In a next step the correlation of the fluorescence signal of the polymer with the polymer concentration in the dip coating solution, i.e. the amount of fiber-attached polymer, was investigated. This correlation is important in measurements of the spatial distribution of the polymer, as local changes of the fluorescence intensity can then be correlated to local concentrations of the surface-attached polymer. While the exact amount of fluorescent monomer RhBMA inside the copolymers cannot be determined via $^1\text{H-NMR}$ spectroscopy, as it falls below the detection limit of NMR, one can still assume with sufficient certainty that a constant amount of the fluorescent label is covalently built into the statistic copolymer. The fluorescence intensity of the fiber-attached polymer will then scale with its amount.

In order to investigate this, lab-engineered paper was subjected to a chemical modification using PMMA-based, photo-reactive polymers and photolithography in order to generate small, sub-millimeter circular polymer spots inside the paper substrates, as described earlier (Böhm et al. 2012) and schematically depicted in Figure 5. Illumination was performed through a lithographical mask that compromises spots ranging from 200 μm up to 1000 μm . Widefield epifluorescence microscopy was used to achieve a reliable radiometric quantification of the fluorescence intensity of the polymer spots. This technique allows illuminating

the sample with a light intensity profile that is constant over the field of view and along the axial path. Thus, fiber-attached polymer across the entire thickness of the paper can contribute to the total fluorescence intensity.

In order to capture and record the fluorescence signal over the entire depth of the paper with a thickness of 60 μm an objective with a low numerical aperture (NA) is required. A good estimate for the detection range is found in the Rayleigh criterion for resolution (Equation 3, see chapter 1.5.1).

With a minimum emission wavelength of 575 nm, as given by the emission filter, a refractive index of $n = 1$ for air as the immersion medium and a numerical aperture of $\text{NA} = 0.13$ for the Nikon CFI 4x Plan Fluor objective, the calculated axial resolution is 68 μm . A visualization of the objective point spread function (Kirshner et al. 2011), based on the Gibson and Lanni model (Gibson and Lanni 1992), confirms the validity of this calculation (see Figure 17).

For the quantification of spot brightness as a function of polymer concentration in the dip coating solution, images of polymer spots ($n = 4-6$) were recorded for each concentration investigated and all images (Fig. 4, e-h) were processed and quantified as described in the materials section. As can be inferred from Figure 4 the fluorescence intensity of the spots increases linearly with an increasing polymer concentration (Fig. 4j, red symbols) and can thus be used as a direct readout of the local polymer concentration, i.e. the amount of fiber-attached polymer.

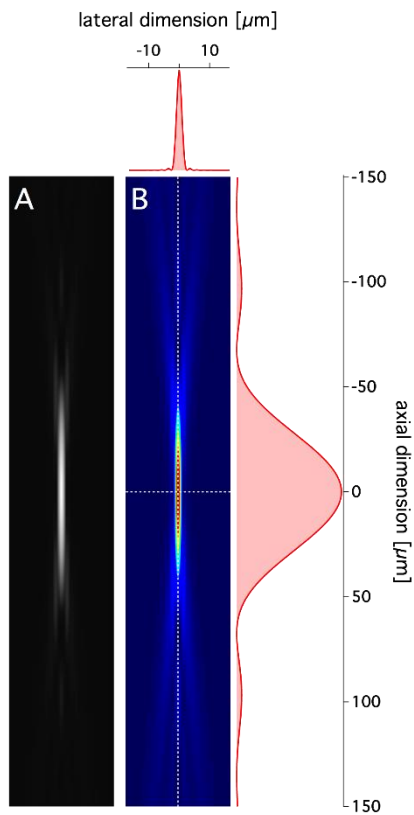


Figure 18: Calculated Point Spread Function for the Nikon CFI Plan Fluor 4x objective

The point spread function for the Nikon CFI 4x Plan Fluor objective was calculated using the Gibson and Lanni model (Gibson and Lanni 1992), based on the following parameters: Detection wavelength $\lambda = 575$ nm, refractive index of the immersion medium $n = 1$, and numerical aperture $NA = 0.13$. Shown is the axial extension of the calculated point spread function with a grayscale (a) or colored (b) intensity. In addition, horizontal and vertical intensity profiles of the lateral and axial centers (white dashed lines) are plotted (red curves)

3.3.2. Analysis of spot border sharpness versus polymer concentration yields valuable information on polymer distribution

The same images were also used to quantify the roughness of the borders of the polymer spots, to determine the spatial precision of the polymer spots created via photolithography as a function of the amount of polymer, that has been attached to the cellulose fibers, i.e. the used polymer concentration in the dip coating

solution during the fabrication of the polymer-modified paper. As a quantitative indicator for the spot roughness, variations in the spot radius, as obtained from numerous measurements, have been analyzed. For this, several image processing steps were required, as described in detail in the materials section (Fig. 4, a-d), whereas a rough border yields a high standard deviation. As shown in Figure 4, the border roughness decreases with an increasing amount of fiber-attached polymer.

The decrease can be described by an exponential decay, which starts to saturate at a polymer concentration of around 30 mg/mL (Fig. 4j, blue symbols). Hence, an increase in the polymer concentration from 5 mg/mL up to 30 mg/mL leads to a more precise chemical micro pattern within the paper sheet, with a sharper, more accurate border, whereas a further increase of the polymer concentration shows no impact on this accuracy. Since the camera used for the detection has an exceptional sensitivity and is capable to detect the fluorescence of single fluorophores, it is unlikely that this saturation in spot sharpness is reached because of a detection threshold for low amounts of polymer. More likely, the obtained minimum in border sharpness is directly linked to the characteristics of the fibrous structure of the paper. However, as the intensity and thus the amount of fiber-attached polymer within the spots further increases beyond a polymer concentration of 30 mg/mL in the used coating solution (Fig. 4j, red symbols), and the paper is dried after it is dip coated inside the polymer solution, additional polymer can only be deposited on already polymer coated cellulose fibers or starts to fill small gaps in between the fibers since it does not contribute to the sharpness of the circular polymer spots. Thus, the analysis of the border sharpness as a function of the polymer concentration is able to identify this important concentration range.

Eventually the interest lies in the preparation of hydrophobic barriers for the production of microfluidic channels. Whether a hydrophobic barrier can be achieved by only coating the fibers with low polymer concentrations while leaving the pores open, is thus of central importance for the design approach. Therefore,

all remaining experiments use paper patterned by polymer based on a solution with a monomer concentration of 30 mg/mL.

3.3.3. Spatial relation of the three component system: paper – polymer - fluid

To investigate the distribution of the polymer inside the paper matrix as well as the interaction of the hydrophobic polymer with aqueous solutions in more detail, confocal laser scanning microscopy (CLSM) was applied. In contrast to widefield microscopy, the detection of fluorescence is limited to the focal plane, leading to a dramatic increase in the imaging contrast, especially for extended 3D specimens such as paper. Furthermore, the capability to perform optical sectioning of the paper cross section allows for the acquisition and reconstruction of the three dimensional structure of the paper.

In a first step, a careful selection of fluorescent dyes and an appropriate imaging protocol to achieve a clean spectral separation of labeled cellulose fibers, polymer, and the aqueous fluid phase was performed. First experiments with unmodified paper substrates revealed a significant autofluorescence of the cellulose fibers in the 450- 500 nm range, although the prepared lab-engineered cellulose sheets have a lignin content well below 1% (Fig. 18, dashed blue line). However, the obtained fluorescence level was not sufficient to achieve high contrast images of the cellulose fibers. Therefore, the decision to enhance the autofluorescence of the cellulose fibers by using the fluorescence brightener Calcofluor White was made. As can be inferred from the emission spectrum (Fig. 18a, solid blue line), a fourfold increase in the emission intensity was achieved, which permitted to image cellulose fibers with high contrast and without occupying an additional spectral detection range (Fig. 18b). As calcofluor white is applied as an aqueous solution which cannot penetrate into the hydrophobic polymer spots, the paper needs to be incubated with the Calcofluor White solution prior to the chemical modification with the photo-reactive, hydrophobic P(MMA-

co-MABP-co-RhBMA) copolymer, in order to achieve an homogeneous labeling of all cellulose fibers present in the cellulose sheet. The distribution of the aqueous solution inside the paper sheet was made visible by using an aqueous FITC-Dextran solution (Fig. 19a and c, green spectrum and image). Finally, Rhodamine B was used as the fluorescent label for the PMMA-based copolymers (Fig. 19a and d, red spectrum and image). Sequential, rather than simultaneous excitation of the three dyes in combination with carefully selected detection windows and sensitivity settings for the detectors (Tab. 2) allowed for distinct spectral separation of all three dyes avoiding cross talk between the detection channels. Besides the ability to relate the spatial positions of the cellulose fibers, the polymer and the fluid phase to each other with high accuracy, this approach makes subsequent image processing steps such as deconvolution and 3D visualizations easier accessible.

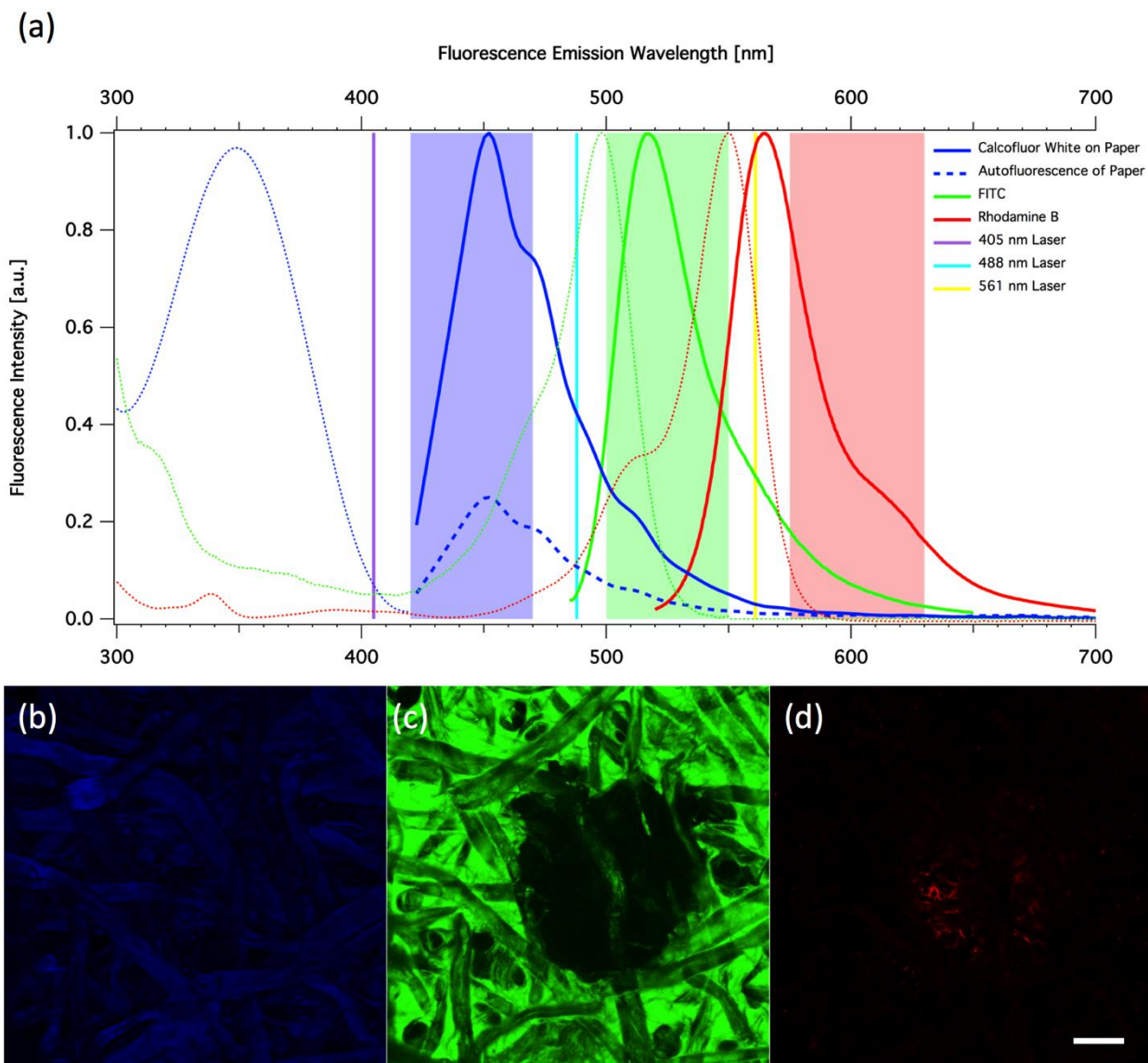


Figure 19: Spectral separation of cellulose, polymer and the fluid-phase

Spectral separation of cellulose, pre-incubated in Calcofluor White (blue), untreated cellulose (blue, dashed), the aqueous phase (labeled with FITC-Dextran, green) and the Rhodamine-labeled polymer P(MMA-co-MABP-co-RhBMA, red) was achieved by sequentially exciting the triple stained samples with a 405 nm (violet), 488 nm (cyan) and 561 nm (yellow) laser, respectively. A comparison of the emission spectra of untreated paper (blue spectrum, dashed line) and paper incubated in calcofluor white (blue spectrum, solid line) reveal a 4-fold increase in fluorescence intensity. Wavelengths of the lasers used for excitations are shown as dashed vertical lines at 405 nm (purple), 488 nm (cyan), and 561 nm (yellow). Dotted lines in the in the respective colour show the excitation spectra of the fluorophores. Boxes mark the detection bandwidth used for each sequential scan. (a) Calcofluor white stained cellulose fibers; (b) FITC-Dextran; (d) Rhodamin labeled polymer P(MMA-co-MABP-co-RhBMA). Scale bar = 100 μm .

Confocal analysis of this preparation reveals, that the aqueous fluid phase (Fig. 19b and f) is successfully excluded from the hydrophobic areas created by P(MMA-co-MABP-co-RhBMA) (Fig. 19c and g), even if the hydrophobic polymer is only attached to the fibers while leaving the pores open. At higher magnification, the polymer distribution can be clearly visualized (Figure 20). Furthermore, the presence of voids within the bulk fluid phase can be observed, especially in the maximum intensity projections of the recorded 3D image stack (Fig. 19f and h). Interestingly, only a few to none of those voids could be observed at the interface of the aqueous phase and the polymer-defined, hydrophobic barrier.

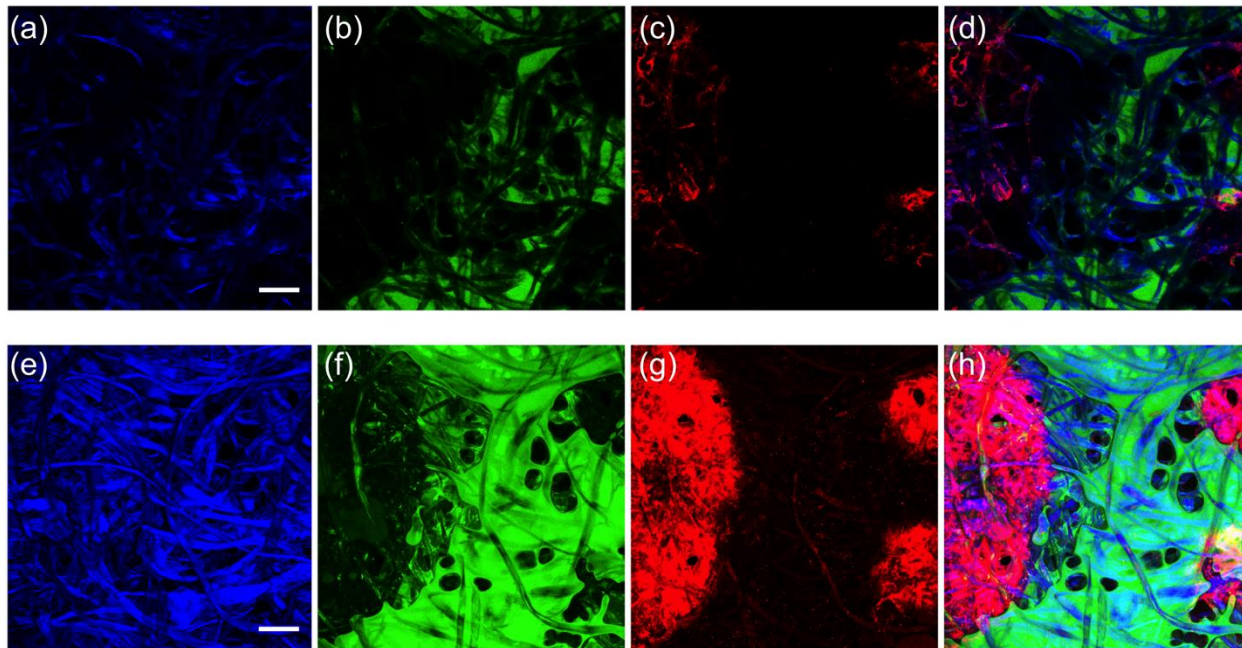


Figure 20: Exclusion of the aqueous phase from hydrophobic polymer areas as revealed by confocal microscopy

Confocal images of a paper pre-incubated in Calcofluor White (blue), before P(MMA-co-MABP-co-RhBMA) spots were generated via photo-lithographically (red) and a FITC-Dextran solution was soaked into the paper matrix (green). The top row shows single confocal planes: (a) Calcofluor White on cellulose fibers; (b) FITC-Dextran solution between the cellulose fibers; (c) hydrophobic polymer spots labeled with Rhodamine B; (d) Overlay of (a-c). The bottom row shows maximum intensity projections of all 100 planes, recorded over a total axial depth of 70 μm : (e) Calcofluor White labeled cellulose fibers; (f) FITC-Dextran solution is excluded from the hydrophobic spots; (g) Rhodamine B labeled polymer spots; (h) Overlay of e-g. White Arrows point towards air voids trapped inside the fluid. The aqueous phase labeled with FITC-Dextran is clearly excluded from all hydrophobic P(MMA-co-MABP-co-RhBMA) spots, i.e. from the larger spot at the left (radius = 500 μm) as well as from the two smaller spots at the right (radius = 125 μm). Scale bar = 100 μm .

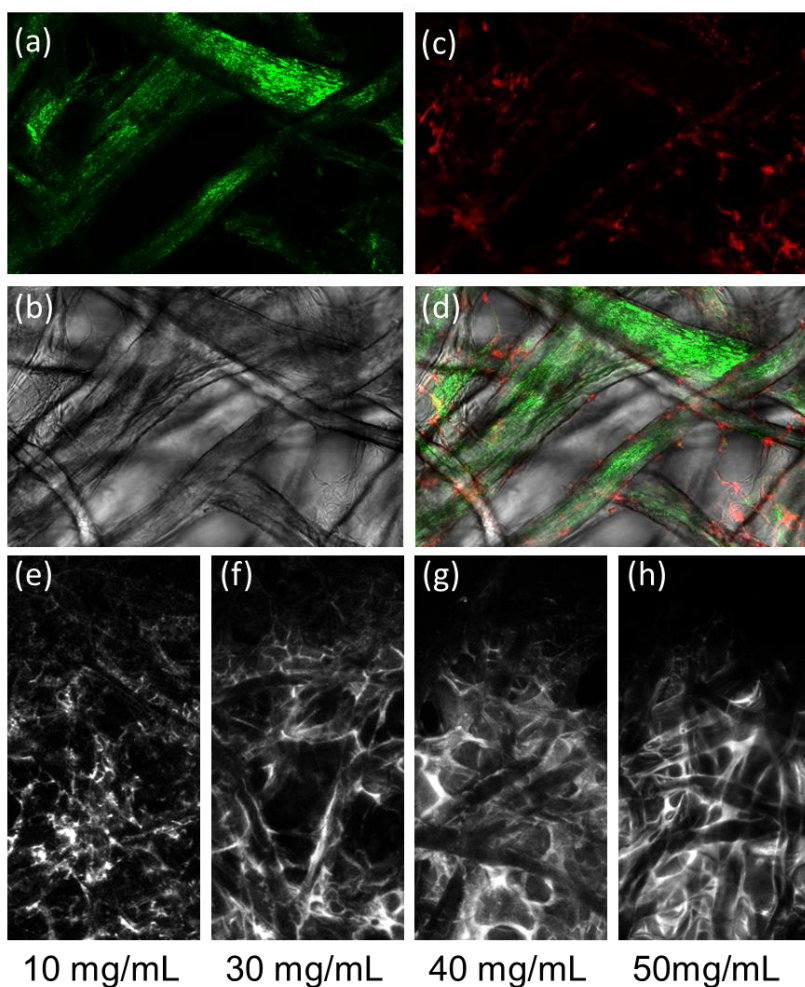


Figure 21: High magnification view of polymer distribution at various concentrations
 More detailed view of the cellulose network marked with calcofluor white (green) and in transmitted light image is given in A and B. C and D show that P(MMA-co-MABP-co-RhBMA) adsorbs and attaches mainly on the surface of cellulose fibers. E-H) Magnified images of P(MMA-co-MABP-co-RhBMA) spots with different concentrations. Images were recorded with a confocal laser scanning microscope using a 20x objective (NA 0.75)

This finding can be explained by the fact that the polymer-modified area remains permeable for gas and thus allows voids to escape, when they get in contact with the liquid/gas interface, i.e. the hydrophobic barrier. Hence, in contrast to approaches, where the pores of the paper are filled with a hydrophobic material to create barriers in paper-based microfluidic systems (Martinez et al. 2007, Carrilho et al. 2009; Derda et al. 2011), the system can potentially prevent a well-known problem of microfluidic systems - the potential blocking of fluid flow by trapped voids. A better view, especially on the liquid/gas interface, is provided by rendering the iso-surfaces of the three components and projecting the view from within the hydrophobic area onto the interface (Figure 21). In relation to the rather scattered distribution of the hydrophobic polymer which is of course a direct result of the underlying paper structure, a relatively smooth liquid/air interface forms thanks to the surface tension of the water.

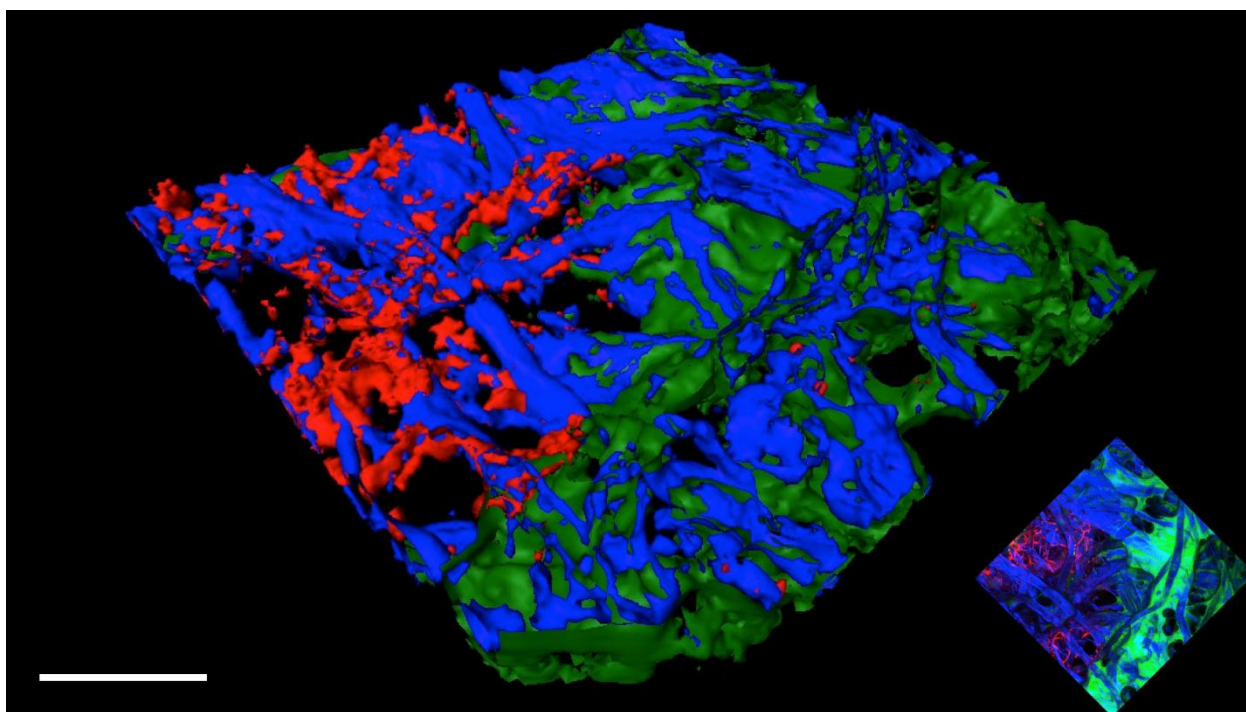


Figure 22: 3D isosurface generation for quantitative analysis of volume and surface areas
3D surface Rendering of a P(MMA-co-MABP-co-RhBMA) spot in paper imposing a barrier for the FITC-Dextran labeled fluid phase. Inset shows the maximum intensity projection of the same planes over a depth of 62 μm . Scale bar = 100 μm .

3.3.4. Initial fluid transport takes place at the fiber surface only

In addition to static images, fluorescence microscopy also allows for the observation of dynamic processes. Therefore, both widefield and confocal microscopy to investigate the fluid inside paper were applied. Especially in the context of paper based microfluidic devices a microscopic view on the dynamic transport of fluid is of great interest to gain an understanding of its relation to the microscopic morphology of the micro-channel, as it is depicted by the cellulose fibers inside the paper matrix.

The capillary driven transport of FITC-Dextran labeled water into the paper matrix was recorded at a frame rate of 30 Hz using the widefield setup described above. Close scrutiny of the obtained data reveals two findings. First, fluid transport only progresses on the surface of the fibers while leaving out the pores in between them. This observation is best seen at the leading edge, where individual fibers are rapidly labeled ahead of the bulk (Fig. 22b box, Fig. 22e-j arrow).

Second, the leading edge is brighter than the bulk zone behind it, which can be quantified by plotting the mean intensity of a subregion of interest (Fig. 22a, box) over the time course of the fluid transport (Fig. 22d). Hence, more liquid is present in this zone. As most fibers in this zone can still be distinguished from one another, the additional amount of liquid is most likely realized as a thicker fluid layer around the fibers. This finding suggests a disequilibrium of the transport rates for the fluid transport towards and from this zone. Confocal analysis of the same process confirms the finding that the fluid transport occurs along the fibers (Fig. 22k-n). In addition, it reveals that the distribution of the liquid film is highly heterogeneous. The pattern resembles that found for polymer depositions recorded at high resolution (Fig. 20) and thereby explains, why an even polymer distribution on the fiber is not achieved.

In a final attempt to demonstrate the capabilities of fluorescence microscopy in investigations on paper based devices, a micro-channel in unlabeled paper by using the hydrophobic polymer P(MMA-co-MABP-co-RhBMA) as the barrier of

the channel was prepared. A 30 Hz recording with the aforementioned widefield setup of the capillary driven transport of an aqueous FITC-Dextran solution in context with the Rhodamine B labeled polymer (Fig. 22-u) shows, that the P(MMA-co-MABP-co-RhBMA) modification confines the moving fluid within a narrower channel than apparently defined by polymer distribution inside the paper matrix. As the size of a microfluidic channel determines capillary flow (Washburn 1921), the resulting, rather than intended dimensions of a channel need to be determined accurately. The example demonstrates, how precise microscopic measurements will be able to further the understanding, optimization, and modeling of paper-based microfluidics. In addition the recording confirms that the leading front of fluid transport inside the channel is restricted to the fibers. Only at later stages the fluid enters zones between the fibers, which becomes apparent when bright and flat areas of FITC-Dextran that form between the paper and the glass coverslip (Fig. 22r-u). Clearly more work is required to fully understand the contributions of both variants of fluid transport and their impact on the properties of a paper based microfluidic system. Fluorescence microscopy with its capability for multi-parameter recordings – especially in dynamic systems – is likely to deliver some valuable input.

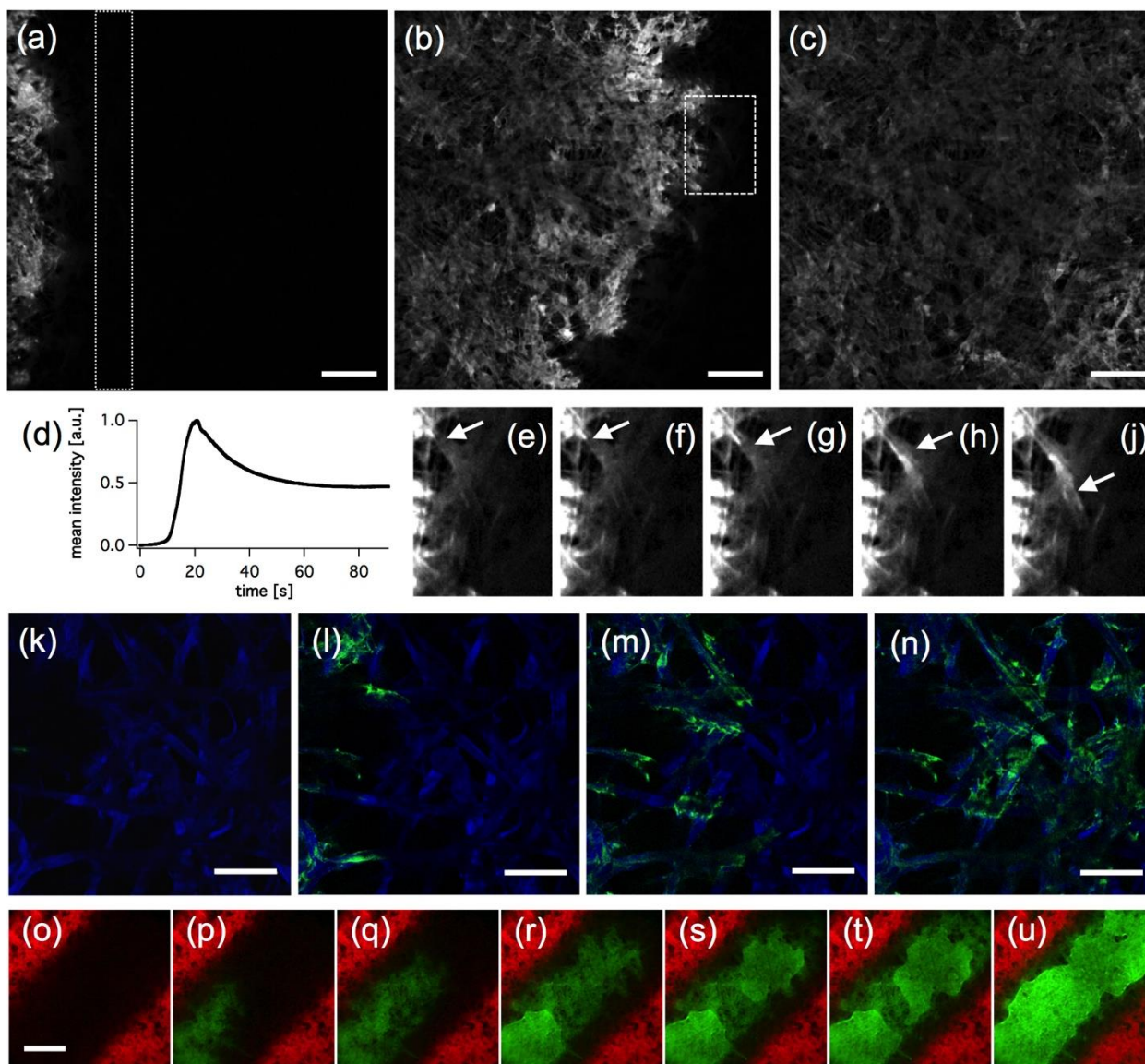


Figure 23: Temporal analysis of FITC-Dextran solution transport using widefield and resonant scanning confocal microscopy

(a-c) Selected frames of an image sequence (a = 5 s; b = 45 s; c = 90 s) recorded at a speed of 30 Hz show the progression of FITC-Dextran in paper. Image acquisition speed was 30 Hz. Scale bar = 200 μ m. Mean fluorescence intensity was quantified in the boxed region (a) throughout the sequence and plotted against time (d). The inset in (b) contains two fibers which get labeled ahead of the leading front (marked with an arrowhead in the magnified views in e-j). (c) At the end of the sequence the entire field of view is evenly field with the fluorescent tracer. (k-n) The same process was recorded by confocal laser scanning microscopy with an acquisition rate of 1 Hz (k = 0 s; l = 20 s; m = 75 s; n = 110 s). FITC-Dextran solution (green) progresses along the cellulose fibers (blue) which were stained with calcofluor white. (o-v) Recording of FITC-Dextran solution (green) progressing along the cellulose fibers inside a P(MMA-co-MABP-co-RhBMA) modified channel (red) inside a piece of paper (time points in subimages o-u = 0, 3, 6, 9, 12, 18, 30 s). Image acquisition speed was 30 Hz. Scale bar = 100 μ m and 500 μ m for images o-u.

3.3.5. Fluid transport in paper

To further investigate the fluid flow in paper, three test fluids were applied in the same manner as described previously (see chapter 3.3.4 and 2.3.4.). One hypothesis to explain the observation of FITC-dextran accumulation on the surface of the cellulose fibers is based on an assumed ionic interaction between FITC-dextran, calcium (or equivalent ions) and cellulose (Paul et al. 2012). Therefore, EGTA was used as chelating agent to examine the possible effect of such an ionic interaction. Findings show that FITC-dextran/EGTA flows with higher velocity through the paper stripe (see table 5 and figure 24). By keeping all other parameters identical – concentration of FITC-dextran, amount of fluid placed on the paper stripe, size of the paper stripe, size of field of view, size of boxed region of interest during image analysis – this effect has to be attributed to the absence of divalent ions. EGTA lowers the availability of divalent ions for the proposed interaction between FITC-dextran, calcium and cellulose.

The observation of faster FITC-dextran/EGTA flow than FITC-dextran flow is confirmed when looking at the outflow rate. Here, the apparent difference in flow velocity is slightly less notable: outflow rate for FITC-dextran is 2 times slower than the outflow rate for FITC-dextran/EGTA.

Finally, FITC isomer I shows an even slower inflow rate. By using acetone instead of water as solvent for FITC Isomer I another ionic interaction is no longer possible: acetone molecules show less polarity than water molecules, therefore acetone has lower affinity towards the surface of the cellulose. Furthermore, acetone offers no possibilities for hydrogen bridge linkage compared to water. By denying the ionic interaction completely due to a lack of dextran, FITC isomer I is even less compelled to stick to the surface of the cellulose fibers. This is also represented by the apparent stagnation, showing a very slow outflow rate.

Table 5: Inflow and outflow rate for different fluids in paper

Fluid	Inflow rate [mean intensity/s]	Outflow rate [mean intensity/s]
FITC-Dextran (aqueous)	0.11	-0.02
FITC-Dextran/EGTA (aqueous)	0.4	-0.04
FITC-Isomer I (acetone)	0.01	-0.001

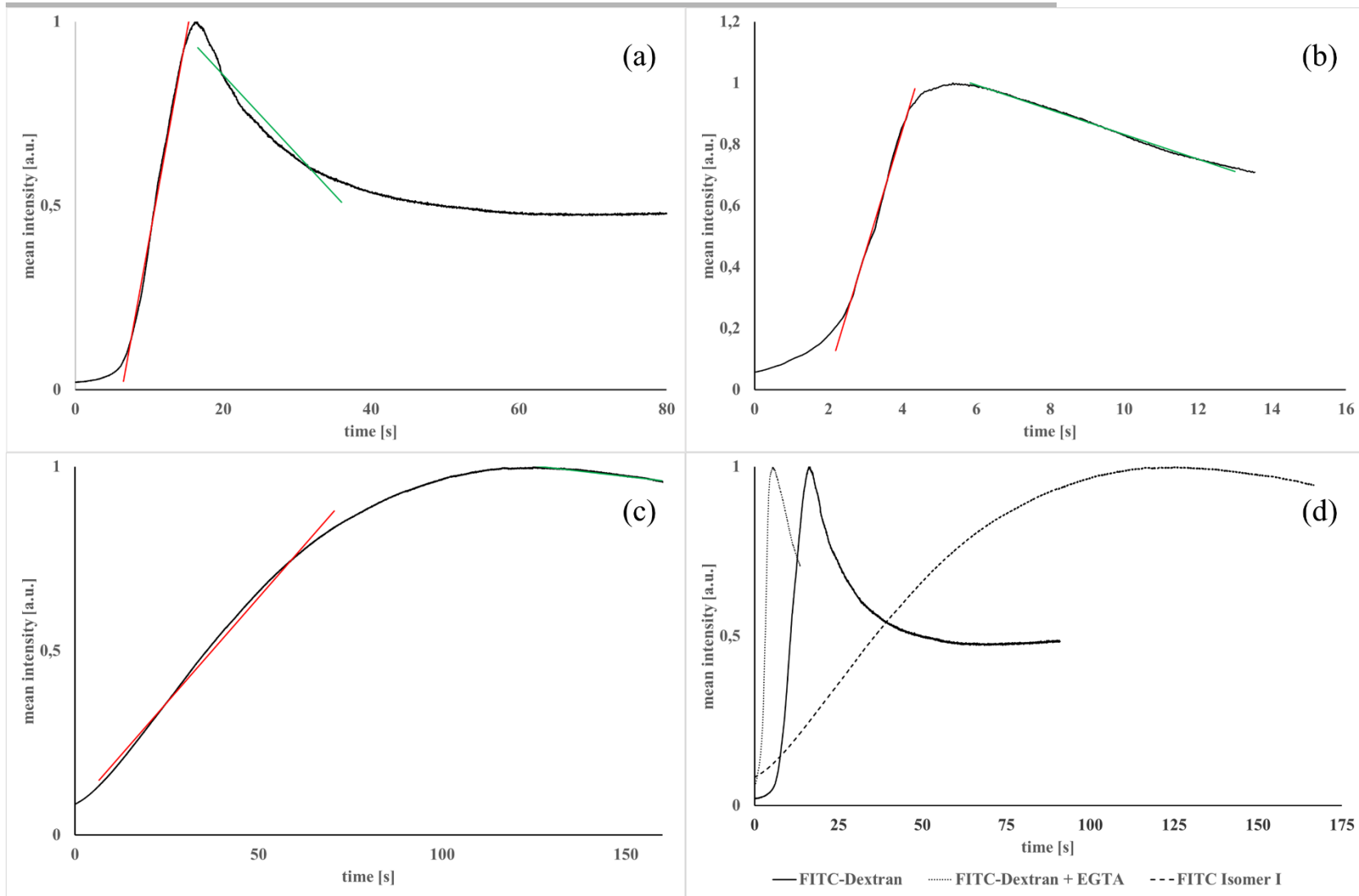


Figure 24: Flow behavior for the three tested fluids aqueous FITC-Dextran, aqueous FITC-Dextran with EGTA and FITC-Isomer I in acetone (a)

Flow behavior of aqueous FITC-Dextran; (b) Flow behavior of aqueous FITC-Dextran with 0.5 mol/L EGTA; (c) flow behavior of aqueous FITC-Dextran with 0.5 mol/L EGTA and (d) combined flow behavior of all three fluid systems. Inflow is marked in red, Outflow is marked in green.

Further experiments with increased EGTA concentrations are needed, to even further lower the availability of ions. However, this might prove difficult, as a concentration of more than 0.5 mol/L EGTA in water is hard to achieve.

Furthermore, the effect of changing the solvent from water to acetone needs to be investigated. Acetone was used to allow for a better solubility of FITC isomer I, since the solubility of FITC isomer I in water is rather poor.

4. Conclusions

4.1. Comparison of deconvolution packages

Four different deconvolution plugins were tested on four different image stacks in order to compare their effects on image quality improvement and to assess the performance in terms of time consumption. Three CPU based deconvolution applications, including the commercially distributed HuygensPro software and one GPU based deconvolution plugin were compared. Even though the GPU based method showed vastly superior performance regarding the reduction of time it comes with two drawbacks: firstly it only runs on NVIDIA graphics cards and secondly the actual output of the image restoration is not of the same quality as for the other deconvolution applications, at least for the test conditions. Among the three CPU based deconvolution applications, the results achieved with the Iterative Deconvolution 3D plugin were comparable with the results achieved with the HuygensPro software, since both enhanced local intensity maxima and by doing so increased the signal to noise ratio. However, the time consumption of the Iterative Deconvolution 3D plugin was significantly larger than with the HuygensPro software and additionally the local intensity maxima intensity enhancement was better for the HuygensPro software than for the Iterative Deconvolution 3D plugin. Deconvolution Lab plugin increased the signal to noise ratio without the significant enhancement of the local intensity maxima as shown in the surface render images (Figure 9) and the maximal intensity Z-projections (Figure 7). Furthermore, time consumption for the Deconvolution Lab plugin was the least among the CPU based deconvolution applications. Therefore, for a day-to-day basis, the Deconvolution Lab plugin seems to be the most reasonable software to apply to image deconvolution. However, the potential value of a GPU based deconvolution application such as CUDA Deconvolution Factory should not be neglected. The speed of performance of such an application lies within or even below (depending on the complexity of the acquired image or image stack) the same time domain of image acquisition with a conventional confocal scanning

microscope. This can allow for real-time deconvolution, in which a newly recorded image gets almost instantly deconvolved, allowing for a quick adaptation of imaging parameters, i.e., in terms of laser powers to reduce or even completely avoid photo bleaching. Hence, an imaging and image processing setup using both, a fast, GPU based deconvolution application which is directly linked to the imaging software and processes the acquired images on the fly and a slower, but at least at the time being better performing CPU based deconvolution application installed on an ideally just for image processing reserved computer system, can greatly enhance the quality of images, which are otherwise hard to acquire with sufficient quality, i.e., images of cells cultivated in a three dimensional system such as a collagen hydrogel or paper.

4.2. Difference between 2D and 3D cell culture: Using cellular distribution, actin morphology and membrane dynamics as read-out parameters

The aim of this chapter was to investigate and quantify a basic problem of three dimensional cell culture systems: keeping the system stable for long term studies and preventing cells from uncontrollably exiting the three dimensional environment. Basic and easy to use systems like collagen hydrogels on top of a glass coverslip surface do not prevent this behavior at all. However, the biocompatibility and easy accessibility of collagen still make it the preferred polymer for the generation of an extracellular matrix replacement. Therefore, a more sophisticated system which is still based on collagen, is desirable. In this work cellulose, another biocompatible and easily accessible polymer, is used to support collagen hydrogel and to fabricate isotropic stiffness conditions by obviating the close proximity of the collagen hydrogel to a glass coverslip surface during cultivation, while still allowing for microscopic investigations and imaging. Using a analysis method that is not based on intensity but instead on localizing and counting of pixels, it is shown, that cells in an unsupported collagen hydrogel with contact to an underlying glass coverslip clearly prefer to inhabit regions of the hydrogel directly on top of the coverslip and that by

embedding a collagen hydrogel into paper this behavior is distinctly altered. Similar to this, cultivating cells in paper without the addition of a collagen hydrogel shows a comparable alteration of distribution, shifting the main amount of cells towards the central region of the paper. Therefore, paper shows promising properties, in terms of fabricating isotropic conditions, for three dimensional cell culture systems. Furthermore, due the plethora of possibilities to modify cellulose, more sophisticated systems can be crafted, allowing for the design of multi-well cell culture platforms or microfluidic channels.

Additional insight into the effects of the culture systems stiffness was gained, by investigating the organization of the actin cytoskeleton. The actin cytoskeleton is highly affected by the surrounding of a cell, therefore the difference in actin organization between cells cultivated in two dimensional or three dimensional systems is significant. Cells cultivated originally in a three dimensional system but which have migrated towards the glass coverslips surface and thus inhabiting a microenvironment related to a two dimensional cell culture system, show similarities to the actin cytoskeleton organization found in cells cultivated in two dimensional cell culture systems, since both show prominent formation of actin stress fibers. However, similarity towards the actin cytoskeleton organization found in cells cultivated in three dimensional systems is at hand, in that cells which have migrated towards the glass coverslip surface still show an overall cell shape which is not completely flattened and show less actin stress fibers at the cells outer borders.

Finally, FRAP measurement on CAAX-mCherry revealed, that the membrane mobility under three dimensional cell culture conditions is higher than under conventional two dimensional conditions, indicated by a faster halftime recovery value of 10 s for the three dimensional cell culture versus 27 s for the two dimensional cell culture system. This can likely be attributed to a higher membrane activity caused by the close contact to the surrounding collagen. However, since the cell type is the same in both culture conditions, overall membrane composition is similar, resulting in an identical mobile fraction of the investigated CAAX-mCherry fusion protein.

4.3. Microscopic analysis of modified paper

Widefield epifluorescence microscopy was used to investigate systems which are composed of three components, namely the paper fiber, the polymer, and the fluid phase and to quickly assess the relation between polymer concentration and barrier-sharpness. Widefield epifluorescence microscopy reveals the connection between the amount of coating polymer and achieved precision of the coating.

More detail, in turn, is obtained by confocal microscopy, which allows to quantify the relation between all three components with high spatial and temporal resolution. Especially useful is the capability of confocal microscopy to investigate individual focal planes with high contrast (i.e. optical sectioning), as this provides means to explore the 3D organization of paper composites. That way, the three dimensional shape of the fluid barrier can be correlated with the local geometry of fiber thickness and orientation as well as polymer concentration and distribution. Quantitative spatial and temporal information as presented in this work will help to development rational approaches to produce microfluidic papers with predictable properties.

Finally, temporal investigations of fluid flow in paper show, that in the system at hand fluid clearly occurs at the surface of the fibers. Thus, to create hydrophobic barriers within this paper matrix, it would be sufficient to coat the surface of the fibers, where fluid transport took place. With the preparation procedure presented in this paper, such a polymer distribution was achieved at 30 mg/mL while higher concentrations only enhanced the amount at positions, where polymer had been deposited already at lower concentrations. The similarity in distribution of fluorescently labeled water with that of the final polymer distribution suggests that the initial distribution of the polymer solution has a higher impact on the final polymer distribution than its concentration. Consequently, to achieve the best starting condition for the polymer to only coat the surface of the fibers, paper should not be submerged in polymer solution. Rather, the solution should be allowed to enter the paper only by capillary forces, ensuring a correct distribution with a minimum of material used.

Apparently a coating of fibers seems to be sufficient to create an effective hydrophobic barrier. Moreover, such a polymer distribution also adds an advantageous property to the final microfluidic system, as it allows the barrier to remain permeable for gases. While small voids may occasionally be trapped within the hydrophilic channel, this property successfully prevents that a void can span the whole width of a channel which would block fluid transport. Hence the design addresses a well-known problem of microfluidic systems.

In conclusion, these initial results demonstrate the potential of fluorescence microscopy for the investigation of paper. Unlike other techniques, which may excel in one of these tasks, fluorescence microscopy is able to simultaneously deliver information with high spatial, spectral, radiometric, and temporal resolution. Thereby, valuable connections between the different aspects of the investigation can be drawn to uncover structure function relations. Moreover, this combined set of information is obtained in-situ and non-invasively, which, by obviating the need of sample preparations, guarantees undisturbed structures and provides compatibility with the investigation of non-static processes, as found e.g. in paper-based microfluidic systems.

5. References

- Antoine C, Nygård P, Gregersen ØW, et al. (2002) 3D images of paper obtained by phase-contrast X-ray microtomography: image quality and binarisation. *Nucl Instruments Methods Phys Res Sect A Accel Spectrometers, Detect Assoc Equip* 490:392–402. doi: 10.1016/S0168-9002(02)01003-3
- Axelrod D, Koppel DE, Schlessinger J, et al. (1976) Mobility measurement by analysis of fluorescence. *Biophys J* 16:1055–1069.
- Balu B, Kim J (2009) Design of superhydrophobic paper/cellulose surfaces via plasma enhanced etching and deposition. *Contact Angle Wettability* 6:4–6.
- Balu B, Kim JS, Breedveld V, Hess DW (2009) Tunability of the Adhesion of Water Drops on a Superhydrophobic Paper Surface via Selective Plasma Etching. *J Adhes Sci Technol* 23:361–380. doi: 10.1163/156856108X383547
- Barcelloss-Hoff MH, Aggeler J, Ram TG, Bissel MJ (1989) Functional differentiation and alveolar morphogenesis of primary mammary cultures on reconstituted basement membrane. *Development* 105:223–235.
- Barkefors I, Thorslund S, Nikolajeff F, Kreuger J (2009) A fluidic device to study directional angiogenesis in complex tissue and organ culture models. *Lab Chip* 9:529–35. doi: 10.1039/b814691h
- Berchtold B (2005) Oberflächengebundene Polymernetzwerke zur Re-Endothelialisierung von porcinen Herzklappenbioprothesen. Albert-Ludwigs-Universität Freiburg im Breisgau
- Böhm A, Carstens F, Trieb C, et al. (2014) Engineering microfluidic papers: effect of fiber source and paper sheet properties on capillary-driven fluid flow. *Microfluid Nanofluidics* 16:789–799. doi: 10.1007/s10404-013-1324-4
- Böhm A, Gattermayer M, Carstens F, et al. (2013) Designing microfabricated paper devices through tailored polymer attachment. *I'Anson SJ Trans. XVth Fundam. res. Symp.* pp 599–618
- Böhm A, Gattermayer M, Trieb C, et al. (2012) Photo-attaching functional polymers to cellulose fibers for the design of chemically modified paper. *Cellulose* 20:467–483. doi: 10.1007/s10570-012-9798-x
- Bruce M a, Butte MJ (2013) Real-time GPU-based 3D Deconvolution. *Opt Express* 21:4766–73.
- Carlmark A, Malmström EE (2003) ATRP grafting from cellulose fibers to create block-copolymer grafts. *Biomacromolecules* 4:1740–5. doi: 10.1021/bm030046v

-
- Carrilho E, Martinez AW, Whitesides GM (2009) Understanding wax printing: a simple micropatterning process for paper-based microfluidics. *Anal Chem* 81:7091–5. doi: 10.1021/ac901071p
- Chinga-Carrasco G, Lenés M, Johnsen PO, Hult E-L (2009) Computer-assisted scanning electron microscopy of wood pulp fibers: dimensions and spatial distributions in a polypropylene composite. *Micron* 40:761–8. doi: 10.1016/j.micron.2009.04.010
- Choquet D, Felsenfeld DP, Sheetz MP, Carolina N (1997) Extracellular Matrix Rigidity Causes Strengthening of Integrin – Cytoskeleton Linkages. *Cell* 88:39–48.
- Coltro WKT, de Jesus DP, da Silva JAF, et al. (2010) Toner and paper-based fabrication techniques for microfluidic applications. *Electrophoresis* 31:2487–98. doi: 10.1002/elps.201000063
- Conrad C, Wünsche A, Tan TH, et al. (2011) Micropilot: automation of fluorescence microscopy-based imaging for systems biology. *Nat Methods* 8:246–9. doi: 10.1038/nmeth.1558
- Cukierman E, Pankov R, Yamada KM (2002) Cell interactions with three-dimensional matrices. *Curr Opin Cell Biol* 13:633–639.
- Cybulski J, Clements J, Prakash M (2014) Foldscope: Origami-based paper microscope. *arXiv Prepr arXiv14031211* 9:1–36.
- Deiss F, Mazzeo A, Hong E, et al. (2013) Platform for high-throughput testing of the effect of soluble compounds on 3D cell cultures. *Anal Chem* 85:8085–94. doi: 10.1021/ac400161j
- Derda R, Laromaine A, Mammoto A, et al. (2009) Paper-supported 3D cell culture for tissue-based bioassays. *Proc Natl Acad Sci U S A* 106:18457–62. doi: 10.1073/pnas.0910666106
- Derda R, Tang SKY, Laromaine A, et al. (2011) Multizone Paper Platform for 3D Cell Cultures. *PLoS One* 6:e18940. doi: 10.1371/journal.pone.0018940
- Dickson A (2000) Quantitative analysis of paper cross-sections. *APPITA J* 53:292–295.
- Dougherty RP (2005) Extensions of DAMAS and Benefits and Limitations of Deconvolution in Beamforming. 11th Aeroacoustics Conference. American Institute of Aeronautics and Astronautics, pp 1–13
- Edelstein A, Amodaj N, Hoover K, et al. (2010) Computer control of microscopes using μ Manager. *Curr Protoc Mol Biol* Chapter 14:Unit14.20. doi: 10.1002/0471142727.mb1420s92
- Eichhorn SJ, Sirichaisit J, Young RJ (2001) Deformation mechanisms in cellulose fibers, paper and wood. *J Mater Sci* 6:3129–3135.
- Eke I, Cordes N (2011) Radiobiology goes 3D: How ECM and cell morphology impact on cell survival after irradiation. *Radiother Oncol* 99:271–8. doi: 10.1016/j.radonc.2011.06.007

-
- Enomae T, Isogai A, Naito M, et al. (2011) Optimum Optical Conditions for Fluorescence Imaging Using a Confocal Laser Scanning Microscope to Determine Three-Dimensional Shape of Ink Jet Dots on Paper. *J Imaging Sci Technol* 55:020201. doi: 10.2352/J.ImagingSci.Technol.2011.55.2.020201
- Fischer WJ, Zankel A, Ganser C, et al. (2013) Imaging of the formerly bonded area of individual fiber to fiber joints with SEM and AFM. *Cellulose* 21:251–260. doi: 10.1007/s10570-013-0107-0
- Foty R (2011) A simple hanging drop cell culture protocol for generation of 3D spheroids. *J Vis Exp* 20:4–7. doi: 10.3791/2720
- Freudiger CW, Yang W, Holtom GR, et al. (2014) Stimulated Raman scattering microscopy with a robust fiber laser source. *Nat Photonics* 8:153–159. doi: 10.1038/nphoton.2013.360
- Geissler A, Chen L, Zhang K, et al. (2013) Superhydrophobic surfaces fabricated from nano- and microstructured cellulose stearyl esters. *Chem Commun (Camb)* 49:4962–4. doi: 10.1039/c3cc41568f
- Gibson SF, Lanni F (1992) Experimental test of an analytical model of aberration in an oil-immersion objective lens used in three-dimensional light microscopy. *J Opt Soc Am A* 9:154–66.
- Griffa A, Garin N, Sage D (2010) Comparison of Deconvolution Software in 3D Microscopy. *GIT Imaging Microsc* 12:43–45.
- Haggarty SJ, Perlis RH (2014) Translation: Screening for Novel Therapeutics With Disease-Relevant Cell Types Derived from Human Stem Cell Models. *Biol Psychiatry* 75:952–960. doi: 10.1016/j.biopsych.2013.05.028
- Haigler CH, Brown RM, Benziman M (1980) Calcofluor white ST Alters the in vivo assembly of cellulose microfibrils. *Science* 210:903–6.
- Hakkinen KM, Harunaga JS, Doyle AD, Yamada KM (2011) Direct comparisons of the morphology, migration, cell adhesions, and actin cytoskeleton of fibroblasts in four different three-dimensional extracellular matrices. *Tissue Eng Part A* 17:713–24. doi: 10.1089/ten.TEA.2010.0273
- Han R, Li Z, Fan Y, Jiang Y (2013) Recent advances in super-resolution fluorescence imaging and its applications in biology. *J Genet Genomics* 40:583–95. doi: 10.1016/j.jgg.2013.11.003
- Hermanson GT (2008) Silane Coupling Agents. *Bioconjugate Tech.* (Second Ed. Springer US, Boston, MA, pp 562–581
- Herth W, Schnepf E (1980) The Fluorochrome, Calcofluor White, Binds Oriented to Structural Polysaccharide Fibrils. *Protoplasma* 105:129–133.

-
- Hu J, Wang M, Frantz P, et al. (1996) Imaging of Single Extended DNA Molecules on Flat (Aminopropyl) triethoxysilane - Mica by Atomic Force. *Langmuir* 12:1697–1700.
- Huh D, Hamilton G a, Ingber DE (2011) From 3D cell culture to organs-on-chips. *Trends Cell Biol* 21:745–54. doi: 10.1016/j.tcb.2011.09.005
- Huh D, Kim HJ, Fraser JP, et al. (2013) Microfabrication of human organs-on-chips. *Nat Protoc* 8:2135–57. doi: 10.1038/nprot.2013.137
- Hutmacher DW (2010) Biomaterials offer cancer research the third dimension. *Nat Mater* 9:90–3. doi: 10.1038/nmat2619
- Ideguchi T, Holzner S, Bernhardt B, et al. (2013) Coherent Raman spectro-imaging with laser frequency combs. *Nature* 502:355–8. doi: 10.1038/nature12607
- Jang H, Robertson A, Seth R (1992) Transverse dimensions of wood pulp fibers by confocal laser scanning microscopy and image analysis. *J Mater Sci* 27:6391–6400.
- Jorand R, Le Corre G, Andilla J, et al. (2012) Deep and clear optical imaging of thick inhomogeneous samples. *PLoS One* 7:e35795. doi: 10.1371/journal.pone.0035795
- Kirshner H, Aguet F, Sage D, Unser M (2012) 3-D PSF fitting for fluorescence microscopy: implementation and localization application. *J Microsc* 249:13–25.
- Kirshner H, Sage D, Unser M (2011) 3D PSF Models for Fluorescence Microscopy in ImageJ. *Proc. Twelfth Int. Conf. Methods Appl. Fluoresc. Spectrosc. Imaging Probes.* p 154
- Klemm D, Heublein B, Fink H-P, Bohn A (2005) Cellulose: fascinating biopolymer and sustainable raw material. *Angew Chem Int Ed Engl* 44:3358–93. doi: 10.1002/anie.200460587
- Landmann L (2002) Deconvolution improves colocalization analysis of multiple fluorochromes in 3D confocal data sets more than filtering techniques. *J Microsc* 208:134–47.
- Li L, Tian J, Ballerini D, et al. (2013) A study of the transport and immobilisation mechanisms of human red blood cells in a paper-based blood typing device using confocal microscopy. *Analyst* 138:4933–40. doi: 10.1039/c3an00810j
- Li X, Ballerini DR, Shen W (2012) A perspective on paper-based microfluidics: Current status and future trends. *Biomicrofluidics* 6:11301–1130113. doi: 10.1063/1.3687398
- Li X, Tian J, Nguyen T, Shen W (2008) Paper-Based Microfluidic Devices by Plasma. *Anal Chem* 80:9131–9134. doi: 10.1039/b811135a.10.1021/ac801729t
- Lindström T, Wågberg L, Larsson T (2005) On the nature of joint strength in paper A review of dry and wet strength resins used in paper manufacturing On the nature of joint strength in paper – A review of dry and wet strength resins used in paper. 13th Fundam. Res. Symp

-
- Lorbach C, Hirn U, Kritzing J, Bauer W (2012) Automated 3D measurement of fiber cross section morphology in handsheets. *Nord PULP Pap Res J* 27:264–269.
- Lutz B, Liang T, Fu E, et al. (2013) Dissolvable fluidic time delays for programming multi-step assays in instrument-free paper diagnostics. *Lab Chip* 13:2840–7. doi: 10.1039/c3lc50178g
- Luu D-T, Martinière A, Sorieul M, et al. (2012) Fluorescence recovery after photobleaching reveals high cycling dynamics of plasma membrane aquaporins in Arabidopsis roots under salt stress. *Plant J* 69:894–905. doi: 10.1111/j.1365-313X.2011.04841.x
- Markert CD, Guo X, Skardal A, et al. (2013) Characterizing the micro-scale elastic modulus of hydrogels for use in regenerative medicine. *J Mech Behav Biomed Mater* 27:115–27. doi: 10.1016/j.jmbbm.2013.07.008
- Martinez AW, Phillips ST, Butte MJ, Whitesides GM (2007) Patterned paper as a platform for inexpensive, low-volume, portable bioassays. *Angew Chem Int Ed Engl* 46:1318–20. doi: 10.1002/anie.200603817
- Martinez AW, Phillips ST, Whitesides GM, Carrilho E (2010) Diagnostics for the developing world: microfluidic paper-based analytical devices. *Anal Chem* 82:3–10. doi: 10.1021/ac9013989
- Marulier C, Dumont PJJ, Orgéas L, et al. (2012) Towards 3D analysis of pulp fiber networks at the fiber and bond levels. *Nord Pulp Pap Res J* 27:245–255.
- Material N, Penetration C, Ma H, et al. (2012) Multicellular Tumor Spheroids as an In Vivo – Like Tumor Model for Three-Dimensional Imaging of. 11:487–498. doi: 10.2310/7290.2012.00012
- McNally JG, Karpova T, Cooper J, Conchello J a (1999) Three-dimensional imaging by deconvolution microscopy. *Methods* 19:373–85. doi: 10.1006/meth.1999.0873
- Miyazaki M, Kaneno J, Uehara M, et al. (2003) Simple method for preparation of nanostructure on microchannel surface and its usage for enzyme-immobilization. *Chem Commun (Camb)* 648–9.
- Moss P, Retulainen E, Paulapuro H, Aaltonen P (1993) Taking a new look at pulp and paper - Application of confocal laser scanning microscopy (CLSM) to pulp and paper research. *Pap JA PUU-PAPER TIMBER* 75:74–79.
- Niv H, Gutman O, Kloog Y, Henis YI (2002) Activated K-Ras and H-Ras display different interactions with saturable nonraft sites at the surface of live cells. *J Cell Biol* 157:865–72. doi: 10.1083/jcb.200202009
- Ozaki Y, Bousfield DW, Shaler SM (2006) Three-dimensional observation of coated paper by confocal laser scanning microscope. *Tappi J* 5:3–8.

-
- Ozeki Y, Umemura W, Otsuka Y, et al. (2012) High-speed molecular spectral imaging of tissue with stimulated Raman scattering. *Nat Photonics* 6:845–851. doi: 10.1038/NPHOTON.2012.263
- Pampaloni F, Stelzer E (2010) Three-dimensional cell cultures in toxicology. *Biotechnol Genet Eng Rev* 26:117–38.
- Paul UC, Manian AP, Široká B, et al. (2012) Sorption of anionic polysaccharides by cellulose. *Carbohydr Polym* 87:695–700. doi: 10.1016/j.carbpol.2011.08.049
- Pelham R, Wang Y (1997) Cell locomotion and focal adhesions are regulated by substrate flexibility. *Proc Natl Acad Sci USA* 94:13661–13665.
- Persson BNJ, Ganser C, Schmied F, et al. (2013) Adhesion of cellulose fibers in paper. *J Phys Condens Matter* 25:045002. doi: 10.1088/0953-8984/25/4/045002
- Petersen OW, Rønnov-Jessen L, Howlett a R, Bissell MJ (1992) Interaction with basement membrane serves to rapidly distinguish growth and differentiation pattern of normal and malignant human breast epithelial cells. *Proc Natl Acad Sci U S A* 89:9064–8.
- Pigorsch E, Finger M, Thiele S, Al E (2013) Analysis of starch distribution in the paper cross-section by Raman microscopy. *Appl Spectrosc* 67:59–65.
- Pollard TD, Cooper J a (2009) Actin, a central player in cell shape and movement. *Science* 326:1208–12. doi: 10.1126/science.1175862
- Rayleigh, Lord (1903) On the Theory of Optical Images, with special reference to the Microscope. *Trans Soc* 17:474–482.
- Rayleigh, Lord (1879) Investigations in optics, with special reference to the spectroscope. *Philos Mag Ser 5* 8:261–274.
- Reits EAJ, Neefjes JJ (2001) From fixed to FRAP : measuring protein mobility and activity in living cells. *Nat Cell Biol* 3:145–147.
- Renz M (2013) Fluorescence microscopy-a historical and technical perspective. *Cytometry A* 83:767–79. doi: 10.1002/cyto.a.22295
- Richardson WH (1972) Bayesian-Based Iterative Method of Image Restoration. *J Opt Soc Am* 62:55. doi: 10.1364/JOSA.62.000055
- Ridler TW, Calvard S (1978) Picture thresholding using an iterative selection method. *IEEE Trans Syst Man Cybern* 630–632.
- Sahl SJ, Moerner WE (2013) Super-resolution fluorescence imaging with single molecules. *Curr Opin Struct Biol* 23:778–87. doi: 10.1016/j.sbi.2013.07.010
- Samuelsen EJ, Houen P, Gregersen ØW, Helle T (2001) Three-dimensional imaging of paper by use of synchrotron x-ray microtomography. *J PULP Pap Sci* 27:50–53.

-
- Schäfer CG, Gallei M, Zahn JT, et al. (2013) Reversible Light - , Thermo - , and Mechano-Responsive Elastomeric Polymer Opal Films. *Chem Mater* 25:2309–2318.
- Schindelin J, Arganda-Carreras I, Frise E, et al. (2012) Fiji: an open-source platform for biological-image analysis. *Nat Methods* 9:676–82. doi: 10.1038/nmeth.2019
- Schmied FJ, Teichert C, Kappel L, et al. (2012) Joint strength measurements of individual fiber-fiber bonds: an atomic force microscopy based method. *Rev Sci Instrum* 83:073902. doi: 10.1063/1.4731010
- Sethi T, Rintoul R, Moore S, et al. (1999) Extracellular matrix proteins protect small cell lung cancer cells against apoptosis : A mechanism for small cell lung cancer growth and drug resistance in vivo. *Nat Med* 5:662 – 668.
- Shiraishi Y, Miyamoto R, Zhang X, Hirai T (2007) Rhodamine-Based Fluorescent Thermometer Exhibiting Selective Emission Enhancement at a Specific Temperature Range. 3032–3033.
- Sibarita J (2005) Deconvolution Microscopy. *Adv Biochem Engin/Biotechnol* 95:201–243. doi: 10.1007/b102215
- Singh S, Carpenter AE, Genovesio A (2014) Increasing the Content of High-Content Screening: An Overview. *J Biomol Screen* 19:640–650. doi: 10.1177/1087057114528537
- Slepkov AD, Ridsdale A, Pegoraro AF, et al. (2010) Multimodal CARS microscopy of structured carbohydrate biopolymers. *Biomed Opt Express* 1:1347–1357. doi: 10.1364/BOE.1.001347
- Sukhorukov VM, Dikov D, Busch K, et al. (2010) Determination of protein mobility in mitochondrial membranes of living cells. *Biochim Biophys Acta* 1798:2022–32. doi: 10.1016/j.bbamem.2010.07.016
- Svensson S, Aronsson M (2003) Using Distance Transform Based Algorithms for Extracting Measures of the Fiber Network in Volume Images of Paper. *IEEE Trans Syst MAN Cybern PART B-CYBERNETICS* 33:562–571.
- Swedlow JR (2012) Innovation in biological microscopy: current status and future directions. *Bioessays* 34:333–40. doi: 10.1002/bies.201100168
- Szent-Györgyi AG (2004) The early history of the biochemistry of muscle contraction. *J Gen Physiol* 123:631–41. doi: 10.1085/jgp.200409091
- Tanaka H, Murphy CL, Murphy C, et al. (2004) Chondrogenic differentiation of murine embryonic stem cells: effects of culture conditions and dexamethasone. *J Cell Biochem* 93:454–62. doi: 10.1002/jcb.20171
- Thelen M (2001) Dancing to the tune of chemokines. *Nat Immunol* 2:129–134.

-
- Tobjörk D, Österbacka R (2011) Paper electronics. *Adv Mater* 23:1935–61. doi: 10.1002/adma.201004692
- Tomasek JJ, Hay ED, Fujiwara K (1982) Collagen modulates cell shape and cytoskeleton of embryonic corneal and fibroma fibroblasts: distribution of actin, alpha-actinin, and myosin. *Dev Biol* 92:107–22.
- Turturro M V, Christenson MC, Larson JC, et al. (2013) MMP-sensitive PEG diacrylate hydrogels with spatial variations in matrix properties stimulate directional vascular sprout formation. *PLoS One* 8:e58897. doi: 10.1371/journal.pone.0058897
- Usui ML, Mansbridge JN, Carter WG, et al. (2008) Keratinocyte migration, proliferation, and differentiation in chronic ulcers from patients with diabetes and normal wounds. *J Histochem Cytochem* 56:687–96. doi: 10.1369/jhc.2008.951194
- Verveer PJ, Swoger J, Pampaloni F, et al. (2007) High-resolution three-dimensional imaging of large specimens with light sheet-based microscopy. *Nat Methods* 4:311–313. doi: 10.1038/NMETH1017
- Vincent LG, Choi YS, Alonso-latorre B, et al. (2014) Mesenchymal Stem Cell Durotaxis Depends on Substrate Stiffness Gradient Strength. *J Biotechnol* 8:472–484. doi: 10.1002/biot.201200205.Mesenchymal
- Wang N, Butler JP, Ingber DE (1993) Mechanotransduction across the cell surface and through the cytoskeleton. *Science* (80-) 3:257. doi: 10.1016/0962-8924(93)90050-B
- Washburn EW (1921) The dynamics of capillary flow. *Phys Rev* 17:273–283.
- Weber LM, Lopez CG, Anseth KS (2009) Effects of PEG hydrogel crosslinking density on protein diffusion and encapsulated islet survival and function. *J Biomed Mater Res A* 90:720–9. doi: 10.1002/jbm.a.32134
- Wiltsche M, Donoser M, Bauer W (2006) A novel destructive approach for 3D paper structure analysis. *Lenzinger Berichte* 86:90–95.
- Wiltsche M, Donoser M, Kritzing J, Bauer W (2011) Automated serial sectioning applied to 3D paper structure analysis. *J Microsc* 242:197–205. doi: 10.1111/j.1365-2818.2010.03459.x
- WITec (2000) Confocal Raman & AFM Imaging of Paper. *Appl note* 49:1–9.
- Wood W, Faria C, Jacinto A (2006) Distinct mechanisms regulate hemocyte chemotaxis during development and wound healing in *Drosophila melanogaster*. *J Cell Biol* 173:405–16. doi: 10.1083/jcb.200508161
- Wormer DB, Davis K a, Henderson JH, Turner CE (2014) The focal adhesion-localized CdGAP regulates matrix rigidity sensing and durotaxis. *PLoS One* 9:e91815. doi: 10.1371/journal.pone.0091815

Xu L, Parker I, Filonenko Y (1997) Technique for determining the fiber distribution in the z-direction using confocal microscopy and image analysis. *APPITA J* 50:325–328.

Yu L, Li CM, Zhou Q, et al. (2007) Functionalized multi-walled carbon nanotubes as affinity ligands. *Nanotechnology* 18:115614. doi: 10.1088/0957-4484/18/11/115614

Zahm J, Kaplan H, Herard, A-LDoriot F, et al. (1997) Cell Migration and Proliferation During the In Vitro Wound Repair of the Respiratory Epithelium. *Cell Motil Cytoskeleton* 43:33–43.

Zheng G, Cui Y, Karabulut E, et al. (2013) Nanostructured paper for flexible energy and electronic devices. *MRS Bull* 38:320–325.

6. Danksagung

Mein aller erster Dank geht an PD Dr. Tobias Meckel. Der immer vorhandene Blick über den interdisziplinären Tellerrand hinaus war immer sehr wertvoll und hochgeschätzt. Danke für die nicht immer einfache Betreuungsarbeit.

Dank auch an Prof. Gerd Thiel und Prof. Markus Biesalski für die Möglichkeit an diesem Projekt zu arbeiten.

Besonderer Dank auch an Alexander Böhm. Die Zusammenarbeit und der vermittelte Einblick in die Papier- und Polymerchemie war sehr wertvoll

Danke auch an die Bewohner des Raumes B1|01 83: Miriam, Laura, Florian.

Danken möchte ich auch den übrigen Mitgliedern der AG Meckel, AG Thiel und AG Biesalski.

Unbedingt danken möchte ich auch Henning für unterhaltsame und aufbauende Mittagspausen. Der Doppelhut wird sich durchsetzen!

Größtmöglicher Dank für die immerwährende Unterstützung geht an meine Familie, insbesondere an meine Mutter, meinen beiden kleinen Brüdern, sowie meinen Vater.

Zu guter Letzt Danke ich vor allem Pu, die immer Geduld mit mir hatte und hoffentlich nun mit mir zusammen den Lohn aller Mühen ernten wird.



Diese Arbeit wurde ermöglicht und finanziert durch die Hessische Exzellenz Initiative LOEWE Softcontrol.

7. Curriculum Vitae

Personal Data

Name: Steven Bump
Birth: August 25th 1984 in Rüsselsheim, Germany

Education

2011-2014 PhD-student at Technische Universität Darmstadt, PD Dr. Tobias Meckel
2010 Diploma thesis: “Integrin mediated endocytic uptake of FITC labeled integrin binding peptides: towards bio-selective POSS carriers”, Graduation (“Diplom”) November, 30th (grade “sehr gut”)
2005-2010 Study of biology at Technische Universität Darmstadt. Subjects: plant physiology, biochemistry, special botany
2004-2005 civil service
2004 Abitur (grade 2,8)
1994-2004 Immanuel-Kant-Gymnasium, Rüsselsheim
1991-1994 Albrecht-Dürer-Grundschule, Rüsselsheim

Publications

2014 Bump, Steven; Böhm, Alexander; Babel, Laura; Wendenburg, Sonja; Carstens, Franz; Schabel, Samuel; Biesalski, Markus and Meckel, Tobias. (2014) „Spatial, spectral, radiometric, and temporal analysis of polymer-modified paper substrates using fluorescence microscopy” Cellulose. Volume 22, Issue 1, pp 73-88, doi: 10.1007/s10570-014-0499-5, 2014.

Conference Contributions:

2014 EMBL Conference: Microfluidics 2014; Heidelberg; Poster
2013 EMBO/EMBL Symposium: Seeing is Believing Imaging the Processes of Life 2013; Heidelberg; Poster
2012 EMBL Conference: Microfluidics 2012; Heidelberg; Poster